Democratic and Popular Republic of Algeria
Ministry of Higher Education and Scientific Research
University A.MIRA-BEJAIA

جامعة بجاية
Tasdawit n Bgayet
Université de Béjaïa

Faculty of Technology
Department of Electrical Engineering
Laboratory of Signals and Systems, University of Boumerdes

THESIS

TOWARDS OBTAINING THE DIPLOMA OF DOCTORATE

Field: Science and Technology **Sector:** Telecommunication

Specialty: Telecommunications Systems

Presented by

MERBOUTI Mohammed Abdenacer

Theme

BIOLOGICAL SIGNALS PROCESSING USING ARTIFICIAL INTELLIGENCE

Defended on: July 10th, 2025

Board of Examiners

First and last name	Rank		
Mr KASMI Reda	Professor	Univ. of Bejaia	President
Mrs CHERIFI Dalila	Professor	Univ. of Boumerdes	Rapporteur
Mr KEMIH Karim	Professor	Univ. of Jijel	Examiner
Mr BELLAHSENE Hocine	Lecturer A	Univ. of Bejaia	Examiner

Academic Year : 2024/2025

République Algérienne Démocratique et Populaire
Ministère de l'Enseignement Supérieur et de la Recherche Scientifique
Université A.MIRA-BEJAIA

جامعة بجاية
Tasdawit n Bgayet
Université de Béjaïa

Faculté de Technologie
Département Génie Électrique
Laboratoire signaux et systèmes, Université de Boumerdès

THÈSE

EN VUE DE L'OBTENTION DU DIPLÔME DE DOCTORAT

Domaine : Sciences et Technologies **Filière :** Télécommunication
Spécialité : Systèmes de télécommunications

Présentée par

MERBOUTI Mohammed Abdenacer

Thème

TRAITEMENT DE SIGNAUX BIOLOGIQUES EN UTILISANT L'INTELLIGENCE ARTIFICIELLE

Soutenue le : 10 Juillet 2025 **Devant le Jury composé de :**

Nom et Prénom	**Grade**		
Mr KASMI Reda	Professeur	Univ. de Bejaia	Président
M^me^ CHERIFI Dalila	Professeur	Univ. de Boumerdes	Rapporteur
Mr KEMIH Karim	Professeur	Univ. de Jijel	Examinateur
Mr BELLAHSENE Hocine	MCA	Univ. de Bejaia	Examinateur

Année Universitaire : 2024/2025

الجمهورية الجزائرية الديمقراطية الشعبية
وزارة التعليم العالي والبحث العلمي
جامعة عبد الرحمن ميرة بجاية

جامعة بجاية
Tasdawit n Bgayet
Université de Béjaïa

كلية التكنولوجيا
قسم الهندسة الكهربائية
مختبر الإشارات والأنظمة، جامعة بومرداس

أطروحة نحو الحصول على دبلوم دكتوراه

مجال: علوم وتكنولوجيا قطاع: اتصالات

تخصص: أنظمة الاتصالات

مقدمة من

مربوطي محمد عبد الناصر

موضوع

معالجة الإشارات البيولوجية باستخدام الذكاء الاصطناعي

نوقشت في: 10 جويلية 2025 أمام لجنة التحكيم المكونة من:

الاسم واللقب	الرتبة		
السيد قاسمي رضا	أستاذ	جامعة بجاية	رئيس
السيدة شريفي دليلة	أستاذ	جامعة بومرداس	مقرر
السيد كميح كريم	أستاذ	جامعة جيجل	ممتحن
السيد بلحسن حسين	أستاذ محاضر أ	جامعة بجاية	ممتحن

السنة الدراسية: 2025/2024

République Algérienne Démocratique et Populaire
Ministère de l'Enseignement Supérieur et de la Recherche Scientifique
Université A.MIRA-BEJAIA

جامعة بجاية
Tasdawit n Bgayet
Université de Béjaïa

Faculté de Technologie
Département Génie Electrique
Laboratoire signaux et systèmes, Université de Boumerdès

THÈSE

EN VUE DE L'OBTENTION DU DIPLOME DE DOCTORAT

Domaine : Sciences et Technologies **Filière :** Télécommunication
Spécialité : Systèmes de télécommunications

Présentée par
MERBOUTI Mohammed Abdenacer

Thème

Traitement de signaux biologiques en utilisant l'Intelligence Artificielle

Soutenue le : 10 Juillet 2025 **Devant le Jury composé de :**

Nom et Prénom	Grade		
Mr KASMI Reda	Professeur	Univ. de Bejaia	Président
M^me^ CHERIFI Dalila	Professeur	Univ. de Boumerdes	Rapporteur
Mr KEMIH Karim	Professeur	Univ. de Jijel	Examinateur
Mr BELLAHSENE Hocine	MCA	Univ. de Bejaia	Examinateur

Année Universitaire : 2024/2025

الجمهورية الجزائرية الديمقراطية الشعبية
وزارة التعليم العالي والبحث العلمي
جامعة عبد الرحمن ميرة بجاية

جامعة بجاية
Tasdawit n Bgayet
Université de Béjaïa

كلية التكنولوجيا
قسم الهندسة الكهربائية
مختبر الإشارات والأنظمة، جامعة بومرداس

أطروحة

نحو الحصول على دبلوم

دكتوراه

مجال: علوم وتكنولوجيا **قطاع:** اتصالات
تخصص: أنظمة الاتصالات

مقدمة من
مربوطي محمد عبد الناصر

موضوع

معالجة الإشارات البيولوجية باستخدام الذكاء الاصطناعي

نوقشت في: 10 جويلية 2025

أمام لجنة التحكيم المكونة من:

الاسم واللقب	الرتبة		
السيد قاسمي رضا	أستاذ	جامعة بجاية	رئيس
السيدة شريفي دليلة	أستاذ	جامعة بومرداس	مقرر
السيد كميح كريم	أستاذ	جامعة جيجل	ممتحن
السيد بلحسن حسين	أستاذ محاضر أ	جامعة بجاية	ممتحن

السنة الدراسية: 2025/2024

Dedication

To my mother and father, whose unconditional love, unwavering belief, and countless sacrifices laid the foundation for every step of this journey; thank you for teaching me resilience, curiosity, and the courage to dream.

To my family, whose encouragement and patience carried me through moments of doubt and celebration alike; your strength is my strength.

To my supervisor, Prof. Dalila Cherifi, for your invaluable guidance, intellectual generosity, and steadfast patience. Your wisdom challenged me to grow, and your trust in my potential gave me the confidence to persevere.

To my friends and colleagues; your camaraderie, late-night brainstorming sessions, and shared laughter made this marathon feel like a meaningful adventure.

To the professors and mentors who shaped my academic path with your kindness, insight, and constructive support; thank you for fostering an environment where curiosity thrives.

This achievement is not mine alone, but a tapestry woven by the hands of those who believed in me long before I did. With deepest gratitude, I dedicate this work to you all.

Acknowledgment

First and foremost, all praise is due to Allah, the Most Merciful, the Most Gracious, whose divine guidance, wisdom, and endless blessings granted me the strength, patience, and clarity to complete this journey. To Him I owe every moment of clarity, every ounce of resolve, and every humble accomplishment reflected in this work.

To my beloved mother and father, whose limitless sacrifices, unwavering love, and steadfast belief in me have been my foundation. Your financial and emotional support carried me through every challenge, and your encouragement illuminated my path even in moments of doubt. To my entire family, thank you for your patience, understanding, and unwavering faith in my pursuit of knowledge.

I am profoundly grateful to my supervisor, Prof. Dalila Cherifi, for your academic guidance, intellectual generosity, and relentless motivation. Your door was always open; not only to share your expertise but also to offer hospitality, encouragement, and a listening ear. Your mentorship has shaped me as a scholar, and your trust in my work inspired me to push boundaries.

My heartfelt gratitude extends to Dr. Nicolai Spicher and the University of Göttingen for their extraordinary hospitality, collaborative spirit, and the doors they opened to new academic horizons. The friendships, intellectual exchanges, and opportunities fostered during my time there enriched this research immeasurably. To the vibrant academic community at Göttingen; thank you for welcoming me into your fold and providing an environment where curiosity and innovation thrive.

Finally, to all mentors, colleagues, and friends who walked alongside me on this journey: your contributions, whether grand or subtle, are woven into these pages. May Allah bless you all abundantly, and may this work serve as a humble reflection of the collective support that made it possible.

Mohammed Abdenacer Merbouti

Table of Contents

List of Figures

List of Tables

List of Algorithms

List of Abbreviations

AAMI	Association for the Advancement of Medical Instrumentation
AFDB	Atrial Fibrillation DataBase
AMI	Anterior Myocardial Infarction
AMIGOS	A dataset for Multimodal research of affect, personality traits and mood on Individuals and GrOupS
ANN	Artificial Neural Network
ANS	Autonomous Nervous System
ANSI	American National Standards Institute
ART	Amplitude Ratio Threshold
ASCERTAIN	a multimodal databaASe for impliCit pERsonaliTy and Affect recognitIoN
AT	Angle Threshold
AUC	Area Under the Curve
aVL	lead augmented Vector Left
BBB	Bundle Branch Block
BEM	Boundary Element Method
BMI	Body Mass Index
CBAM	Convolutional Block Attention Module
CEBSDB	Combined measurement of ECG, Breathing, and Seismocardiograms DataBase
CED	Convolutional Encoder-Decoder
CNN	Convolutional Neural Network
CODE	Clinical Outcomes in Digital Electrocardiography
CPU	Central Processing Unit
CSE	Common Standards for Electrocardiography
CSP	Closest Scanned Peak
CW	Characteristic Waves
CWD	Characteristic Waves Delineation
CYBHi	Check Your Biosignals Here initiative
DC	Direct current
DREAMER	A Database for Emotion Recognition Through EEG and ECG Signals From Wireless Low-Cost Off-the-Shelf Devices
DWT	Discrete Wavelet Transform
EC57	ECG Committee 57
ECG	ElectroCardioGram
ECGID	ECG IDentity
EDA	ElectroDermal Activity
EDGAR	Experimental Data and Geometric Analysis Repository
EEG	ElectroEncephaloGram
ELSA-Brasil	Estudo Longitudinal de Saúde do Adulto-Brasil

ELU	Exponential Linear Unit
EMG	ElectroMyoGram
FMRI	Functional Magnetic Resonance Imaging
F-TENG	Flexible arc-shaped TriboElectric NanoGenerator
GRU	Gated Recurrent Unit
GSR	Galvanic Skin Response
HDC	HyperDimensional Computation
HT	Horizontal time Threshold
ICA	Independent Component Analysis
IQR	InterQuartile Range
KNN	K-Nearest Neighbors
LBBB	Left Bundle Branch Block
LGL	Lown-Ganon-Levine
LSTM	Long Short-Term Memory
LT	Length Transformation
MAHNOB-HCI	MAHBNOB-Human Computer Interaction
MASE	Mean Absolute Scaled Error
MCD	Mean Closest Distance
MCG	MagnetoCardioGraphy
MEG	MagnetoEncephaloGraphy
MITDB	Massachusetts Institute of Technology arrhythmia DataBase
MLII	Modified Limb lead II
MNG	Magneto-NeuroGraphy
MSE	Mean Squared Error
mTSI	mean Temporo-Spatial Isochrone
NB	Naïve Bayes
NCA	Neighbors Component Analysis
NN	Neural Networks
NPV	Negative Predictive Value
NSR	Normal Sinus Rhythm
PAF	Paroxysmal Atrial Fibrillation
PCA	Principal Component Analysis
PET	Positron Emission Tomography
PFRT	Peak over the Fiducial points Ratio Threshold
PMI	Posterior wall Myocardial Infarction
PPV	Positive Predictive Value
PSR	Phase Space Reconstruction
PTBDB	Physikalisch-Technische Bundesanstalt DataBase
QTDB	QT-DataBase
RBBB	Right Bundle Branch Block

RESP	Respiratory Responses
RL	Reinforcement Learning
RNN	Recurrent Neural Network
ROC	Receiver Operating Characteristic
SGD	Stochastic Gradient Descent
SP	Selected Peak/Scanned Peak
SQUID	Super-Conducting Quantum Interference Devices
ST	Skin Temperature
STD_DEV	STandarD DEViation
STDB	ST change DataBase
SVEB	SupraVentricular Ectopic Beats
SVM	Support Vector Machines
TDT	Tangent Deviation Threshold
TN	True Negative
VCG	VectorCardioGram
VEB	Ventricular Ectopic Beats
VFDB	Ventricular Fibrillation DataBase
WECG	Wrist ECG
WESAD	Wearable Stress and Affect Detection
WPW	Wolff-Parkinson-White
WT	Wavelet Transform
YAMNet	Yet Another Mobile Network

General Introduction

Background and context

Biological signals serve as the fundamental medium for communication within the human body. These signals, which include electrical, mechanical, optical, chemical, and thermal forms, facilitate the coordination between tissues and organs and are critical for monitoring physiological health, diagnosing disease, and supporting a wide array of applications. Technological advancements have transformed these signals into valuable tools for developing bionic organs, biometric authentication systems, and smart health monitoring solutions. Among these signals, the electrocardiogram (ECG) stands out for its vital role in assessing cardiac function. However, interpreting such signals poses challenges due to their complexity and high dimensionality. Artificial Intelligence (AI), particularly machine learning and neural networks, has become essential in extracting meaningful patterns from biological signals. This is especially important when detecting life-threatening conditions such as Wolff-Parkinson-White (WPW) syndrome, which can lead to severe tachycardia and sudden cardiac events. Casualties of such pathology unfortunately exists in Algeria.

Motivation

The ability to detect and interpret biological signals is central to advancing our understanding of human physiology. These signals offer noninvasive windows into bodily functions and pathologies. However, some conditions, such as WPW syndrome, are intermittent and may remain undetected during routine clinical examinations. This highlights the need for autonomous clinical systems capable of continuous monitoring and timely detection. Such systems not only improve diagnostic accuracy but also serve as life-saving tools by identifying critical conditions before they escalate. The motivation for this research lies in enabling more responsive and intelligent healthcare systems that can autonomously interpret biological signals to detect transient or rare disorders.

A substantial body of work has investigated the processing of biological signals, particularly the ECG, for various medical and non-medical applications. Earlier studies have applied heuristic algorithms for QRS complex detection [1], while more recent approaches incorporate machine learning and deep neural networks for arrhythmia classification [2], cardiac imaging [3], biometric identification [4], and emotion recognition [5]. Techniques such as Convolutional Neural Networks (CNN), Long Short-Term Memory (LSTM) networks, and hybrid models have been developed for tasks ranging from detecting myocardial infarction [6] to predicting sudden

cardiac death [7]. Biometric systems have employed ECG signals for robust identity verification, while affective computing has utilized ECG in detecting emotional states. Despite this progress, challenges remain in delineating ECG components accurately, especially under pathological conditions.

Problem statement

Several critical problems persist in the current landscape of biological signal analysis. First, biological signals are inherently complex and unfamiliar to new researchers, posing a steep learning curve. Their heterogeneity in origin, dynamic nature, and physical form creates an almost limitless range of signals, making standardized approaches difficult. Second, no method in the literature has been established to detect the delta wave of the WPW pattern, a key diagnostic feature. Third, ECG signals with independent rhythms of the P wave and QRS complex, such as those seen in third-degree atrioventricular blocks, pose significant difficulties in waveform delineation. These unresolved issues underscore the necessity for new methodological frameworks capable of handling signal variability and pathology-specific features.

Research objectives

This thesis addresses the aforementioned challenges across three chapters, each contributing to a layered understanding of biological signal analysis through the lens of AI. Chapter I lays the groundwork by offering a comprehensive overview of biological signal types, their classification, and specific attention to the ECG. Chapter II introduces a novel machine learning-based approach for detecting WPW syndrome with a focus on identifying the delta wave. Chapter III enhances peak detection and delineation using reinforcement learning and LSTM to improve the accuracy and efficiency of ECG interpretation, particularly for complex cases such as atrioventricular blocks.

Thesis structure

Chapter I begins with a general framework for categorizing biological signals based on origin, dynamics, and physical form. The focus then shifts to the electrocardiogram, covering its acquisition techniques, signal characteristics, and diagnostic significance. The chapter details the use of ECG in four major application areas: heart imaging, disease detection, biometric authentication, and emotion recognition. It also presents a statistical study on the performance of various heuristic-, machine learning-, and neural network-based approaches in these domains, highlighting trends, datasets, and methodological comparisons from the literature.

Chapter II delves into the detection of Wolff-Parkinson-White (WPW) syndrome. WPW is a rare and intermittent heart condition often overlooked due to its transient nature. The chapter introduces a new peak analyzer based on a three-parameter model that enables the detection of prominent ECG features, including the elusive delta wave in seven steps. By applying machine learning classifiers such as k-nearest neighbors, Naïve Bayes, and artificial neural networks, the method achieves accurate identification of P, Q, R, S, T, and delta peaks. The chapter emphasizes the clinical importance of early and automated detection of WPW, given its association with tachycardia and potential for fatal outcomes.

Chapter III builds upon the method developed in Chapter II by addressing its limitations, particularly in accurately delineating ECG waveform boundaries. A two-parameter peak analyzer is introduced and optimized using reinforcement learning, reducing the number of samples while maintaining signal integrity. This efficiency enables the use of LSTM networks for detailed classification and delineation of fiducial points (onsets, peaks, and ends) of the ECG waveform components. The approach targets complex ECG scenarios such as third-degree atrioventricular block, where P wave detection is nontrivial. The chapter also discusses the critical importance of speed in real-time applications, affirming the feasibility of the proposed method for continuous monitoring systems.

Chapter I. ECG position in biological signal family: machine learning applications

I.1. Introduction

The human body functions with multiple connected tissues that cooperate to keep the body properly alive for as long as possible. The cooperation of the tissues requires a means of communication for signaling transmission. The transmitted signals are named biological signals. Generally, any activity monitored or recorded from an organism in any form (electrical, mechanical, optical, thermal, etc.) is categorized as a biological signal. Scientists implement biological signals for monitoring the health of the body tissues, discovering the functionality of the tissues, and in other experiments such as bionics and biometrics. The interaction with biological signals is getting more reliable in different aspects, such as medical diagnosis where the electrocardiogram (ECG) for example is a tool for extracting the cardiac electrical activity for the detection of arrhythmias and heart pathologies. Additionally, the signal could also be used for estimating the respiratory rate [8], [9] and measuring the number of breaths per minute. Another aspect involves harnessing hidden biological signals for creating bionic organs such as the heart pacemaker, which monitors the electrical activity of the heart and regulates the heart rate if needed. Artificial limbs as prostheses also interact with the electromyogram (EMG) to simulate the job of real limbs [10], [11]. Some artificial products may cause incurable side effects, requiring commercial industries to perform safety assessments before acquiring administrative approval to enter the market. Biochemical tests for example play a role in monitoring the side effects of therapeutic drugs and assessing the safety of newly produced drugs [12], [13]. Cars could also benefit from the ECG signal and eye tracking [14] for assessing the emotion and behavior of drivers, ensuring road safety. These limitless sources of data consequently imply the existence of sensitive data. Biological signals such as face-, finger-, and iris-prints are also feasible as authentication methods to secure individuals' sensitive data. The advance of technology also opens possibilities for mining big data for building smart systems based on heuristic approaches or machine learning which neural networks are currently taking its lead and widening the set of application possibilities with different neural network architecture designs such as Convolutional Neural Networks (CNN), Recurrent Neural Networks (RNN), and lately the Transformers.

This overview chapter will highlight a general image of biological signals and present the state of the art of ECG analysis in detail. The rest of this chapter is structured as follows. Section I-2 covers the related works in biological signal applications in general and the ECG analysis

surveys in particular. A general view on the biological signals and suggested ways of classifying the unlimited types of biological signals are included in Section I-3. Section I-4 focuses more on the acquisition procedure and the characteristics of the ECG signal. Section I-5 introduces the possible objectives using the ECG signal, namely imaging, disease detection, biometric authentication, and emotion recognition. Section I-6 presents a statistical study on the different neural network- and non-neural network-based approaches proposed in the literature and their contributions to ECG analysis in the 4 aforementioned objectives. A discussion on the recent focus of the ECG applications with the limitations introduced is included in Section I-7, and Section I-8 concludes this chapter.

I.2. Related works

The limitless varieties of biological signals also engage the limitless applications to harness such signals. In the literature, Bouzid et al. [15] applied random forest as a classifier for the detection of culprit lesions from the ECG signal. Savadkoohi et al. [16] used the electroencephalogram (EEG) for predicting epileptic seizures with K-nearest neighbors (KNN) and support vector machines (SVM) as classifiers. Menon et al. [17] extracted features from the EMG signal using a hyperdimensional computation (HDC) approach and were able to accurately recognize six hand gestures. Terranova et al. [18] leveraged the deep learning model named YAMNet for sound classification, which was implemented in separating the wind sound from biological signals recorded in the wild. From the sensors' point of view, Yan et al. [19] developed a motion sensor named flexible arc-shaped triboelectric nanogenerator (F-TENG) for harvesting biomechanical energy. The applications are diverse and endless. However, focusing back on capturing the general image of biological signals facilitates the forward steps to harvest the best from such signals. Kaniusas [20] proposed three ways of classifying biological signals in his book named "Biomedical Signals and Sensors I". Therefore, this chapter will adopt and develop the proposed classification approach in the literature and lean towards the electrocardiogram applications specifically. The related works conducted a survey on the ECG signal processing steps [21], a survey on the ECG analysis using both time-frequency and machine-learning approaches [22], and introduced a review of the time-frequency methods applied to the ECG analysis [23]. This overview however will introduce the state of the art of the applications of the electrocardiogram in heart imaging, disease detection, biometric authentication, and emotion recognition.

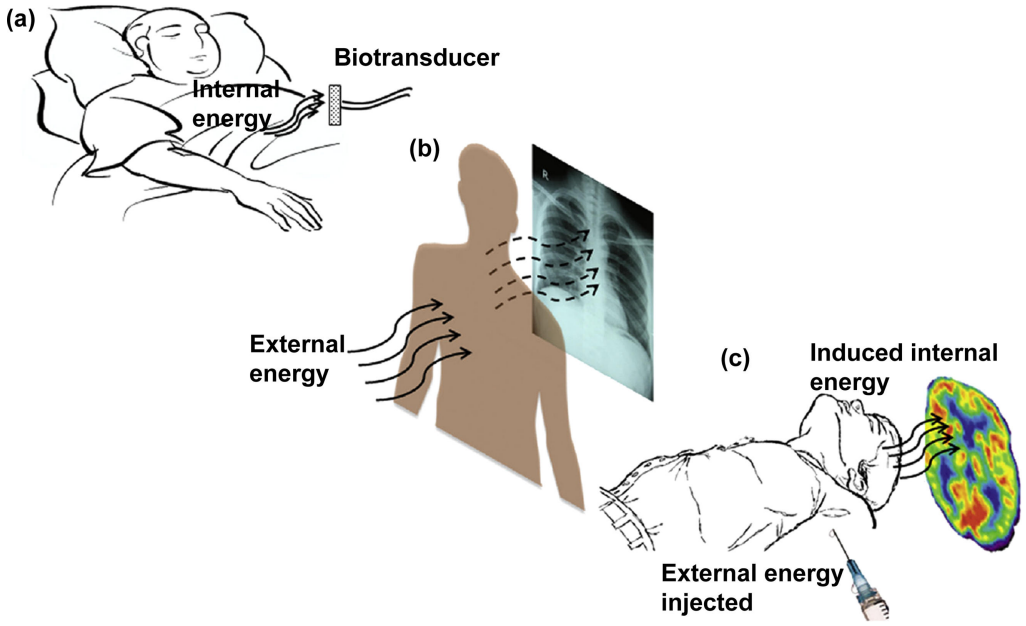

Figure I-1: Origin of biological signals [24]. (a) endogenous, (b) exogenous, (c) induced endogenous.

I.3. Biological signals: an overview

Any activity that occurs in time from an organism is considered a biological signal. The form of the signal could be electric, mechanical, optic, thermal, and many others. Some organism activities could be recorded in more than one form, such as the heart activity, which is recorded in at least electric, magnetic, and acoustic form, depending on the applied acquisition methods, which are evolving. Therefore, a better approach to understand and harness the unlimited biological signals is to start from the big picture. Such an approach is proposed by Kaniusas [20], which classifies biological signals based on the origin, the dynamic nature, or the physical form of the signal.

I.3.a. Origins

The acquisition method of the biological signal determines the origin of the signal. Kaniusas [20] classified the signals according to this criterion into permanent (endogenous) and induced (exogenous) signals. Semmlow [24] also proposed an additional class named induced-endogenous biological signals.

- *Endogenous biological signals* as depicted in Figure I-1 (a) are generated from inside the body and do not require an external excitation. The signal also exists permanently as long as the tissue is alive. Examples of such signals are body temperature, breath sounds, and ionic electrical signals.

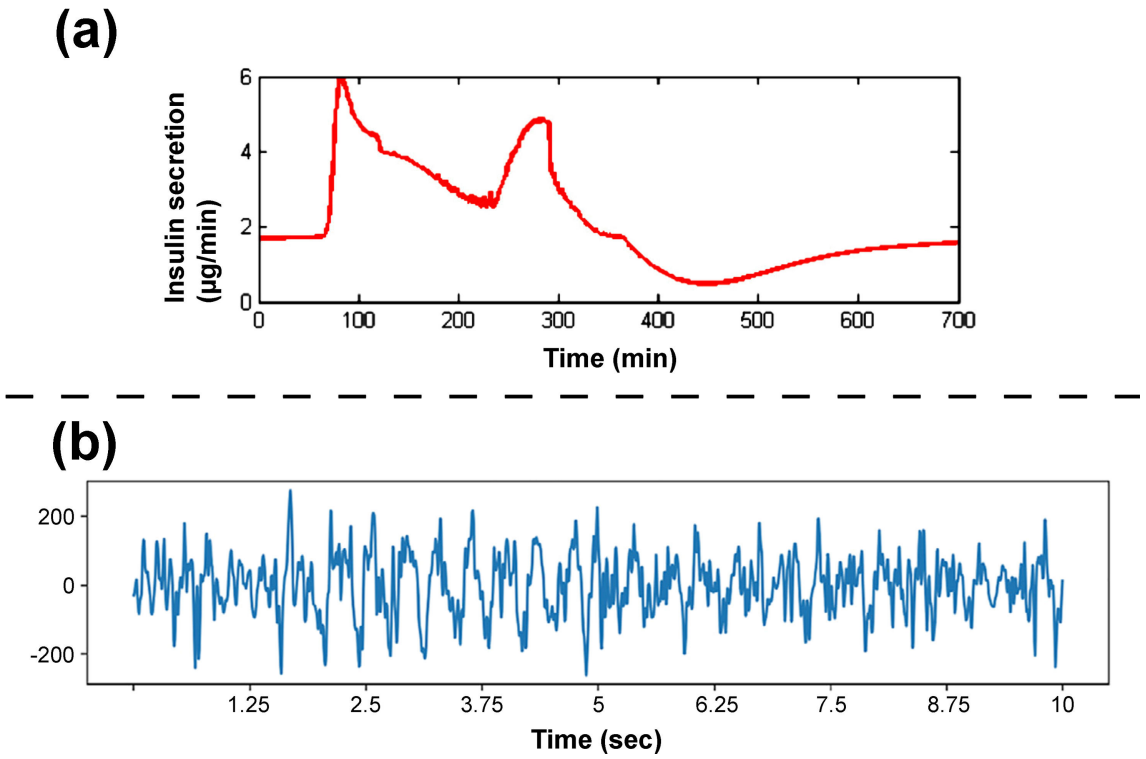

Figure I-2: Dynamic nature of biological signals. (a) quasi-static, (b) dynamic [25], [26].

- *Exogenous biological signals* are first generated from an external energy source, where tissues from inside the body will influence the received energy, absorb a portion then reflect the rest of the energy to the examining system. Such a group is named exogenous biological signals or induced biological signals. The signal is not permanent and exists only during excitation. X-ray imaging as shown in Figure I-1 (b) or temperature remote sensing is an example of such signals.
- *Induced endogenous biological signals* are a sort of combination of the two previous methods, where the body generates the biological signal only after being injected with an external energy source. The signal is not permanent and does not last long after the injection. An example of this is positron emission tomography (PET) as shown in Figure I-1 (c) [27].

I.3.b. Dynamic natures

The dynamic nature of the biological signal is related to the speed of its energy variation with respect to time. The energy variation of the biological signal could be quasi-static, or dynamic.

- *Quasi-static biological signals* vary their energy in a slow manner over time, such as the insulin secretion as depicted in Figure I-2 (a), and body temperature.

- *Dynamic biological signals* are characterized by rapid energy variation, such as the electroencephalogram (EEG) depicted in Figure I-2 (b), photoplethysmography, and electrocardiogram (ECG).

I.3.c. Physical forms

The common forms of biological signals are electric, magnetic, mechanic, optic, acoustic, chemical, and thermal.

- *Electric biological signals* were discovered from the study of muscles and the nervous system [28]. Hence, the signal is also called a bioelectric signal, which is the result of electrochemical passages in cellular systems. Electrocardiogram (ECG), electroencephalogram (EEG), and galvanic skin response (GSR) are examples of bioelectric signals, which are mostly used in medical studies and pathology diagnosis [29] such as epileptic seizure prediction using the EEG [16] and stress detection using GSR [30]. A way of acquiring ECG signals is illustrated in Figure I-3 (a) [31].
- *Magnetic biological signals* follow the existence of bioelectric signals [32]. The intensity of the magnetic biological signal, however, is much weaker and requires very complex magnetometers called Super-conducting quantum interference devices (SQUID) with very precise sensitivity [33] as shown in Figure I-3 (b) [34]. Some examples of magnetic biological signals include magnetoencephalography (MEG), magneto-neurography (MNG), and magnetocardiography (MCG).
- *Mechanic biological signals*, also named biomechanics, are motions that occur in biological systems at each level of the system, starting from the cell, to the tissue, and the whole-body motion. Biomechanics applies the laws of physics [35] and can be measured using different motion sensors, which could be optical transducers such as cameras as depicted in Figure I-3 (c) [36], vibration transducers such as microphones and accelerometers, or movement detectors using distance differentiation such as radars, and sonars. Biomechanic signals are mostly used in detecting diseases related to tissue movements [37] and in recording the kinetic energy of muscular tissues during movements for pattern recognition, which could be used in prostheses [38] and various other applications [19].
- *Optic biological signals* may be intrinsic to an organism such as bioluminescence, or extrinsic using an external source of light [39]. For the human body, light is generally projected into the organism, which by its optical structure influences the projected beams with absorption or reflection. Blood veins for example can be visible under the skin to the camera after being introduced to near-infrared light [40] as illustrated in Figure I-3 (d) [41]. Other applications include using optic biological signals as biosensors for unveiling hidden

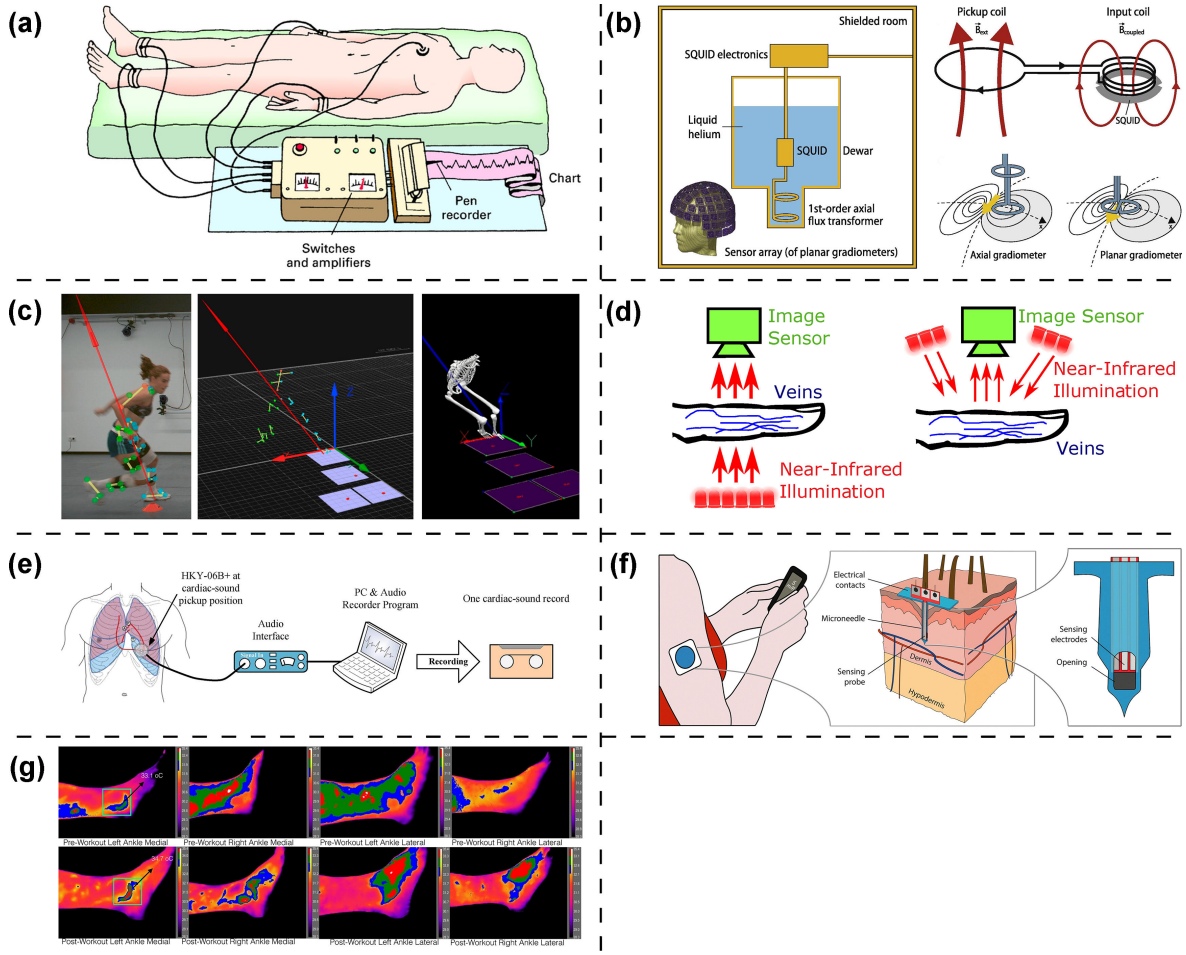

Figure I-3: Ways of acquiring biological signals in different physical forms.

substances such as toxins in polluted water [42] and cancer tumors [43], they are also used in microscopy imaging such as digital holographic microscopy [44] and in analyzing physiological parameters such as depression recognition using remote photoplethysmography [45].

- *Acoustic biological signals* are considered biomechanical signals specified for motions that produce acoustic vibrations. The respiratory system and heartbeats produce unique acoustic sounds, which can be measured using microphones for example as shown in Figure I-3 (e) [46], and processed for diagnosis [39] or as a biometric parameter for distinguishing individuals' sounds [47], [48].
- *Chemical biological signals*, also named biochemical signals, are communications between multicellular organisms, which are carried out by extracellular signals or messengers originating from the environment of an individual cell. These messengers make the coordination of individual cells possible. A biochemical process is the response of a cell to an extracellular messenger after it binds to the cell surface receptor, which is called signal

transduction [49], [50]. This process affects in concentration of various chemical substances that can be measured. Monitoring glucose from dermal interstitial fluid [51] as shown in Figure I-3 (f) is an example of a biochemical signal. Another example includes protein-ligand interaction prediction using machine learning for determining the efficacy and safety profiles of drugs in production [52].

- *Thermal biological signals* reveal the thermal behavior of the body, which can be used to determine the physiological response of parts of the body during a failure [53] since the increment of temperature is a way of defense against tumor cells, to prevent the spread of affected cells by malignancy [54]. Thermometers in this case are used as a way of measuring temperature in different parts of the body such as thermal cameras as shown in Figure I-3 (g) [55]. Other applications include facial emotion recognition by measuring facial skin temperature [56].

I.4. Electrocardiogram: Acquisition and characteristics

The electrocardiogram (ECG) is an endogenous dynamic biological signal of an electric type. It represents a recording of the heart activity during the depolarization and repolarization of the atria and ventricles, allowing for the observation of the overall rhythm of the cardiac activity, to reveal abnormalities of different kinds of arrhythmia [57]. The signal is mostly converted from an ionic electric signal to an electronic signal using transducers named electrodes. These electrodes measure biopotentials generated by the movement of ions across cell membranes from within the biological tissue. The electrodes are placed non-invasively on the skin, and depending on the implemented lead-positioning, the placement of the electrodes can be anywhere on the body. The most commonly known positioning is the 12-lead positioning using 10 electrodes, where 6 electrodes are placed on the chest and 4 on the limbs. A chosen difference of potentials between these 10 electrodes creates 12 signals named 12-lead [58]. As shown in Figure I-4, each lead exhibits information about the heart on one axis originating from the center of the heart, and follows a direction depending on the placement of the electrodes that make up the lead. Most of the leads include three ECG characteristic waves named P wave, QRS complex, and T wave as depicted in Figure I-5. The P wave corresponds to the depolarization of the atria, the QRS complex to the depolarization of the ventricles, and the T wave to the repolarization of the ventricles. The repolarization of the atria is hidden under the QRS complex (the depolarization of the ventricles). The segment between the T wave and the P wave represents a horizontal line named the isoelectric line. A wave that is above the isoelectric line is positive, and vice versa for a wave below the isoelectric line. A positive ECG wave indicates that the biopotential is moving towards the lead or the electrode, in which the heart muscle cells

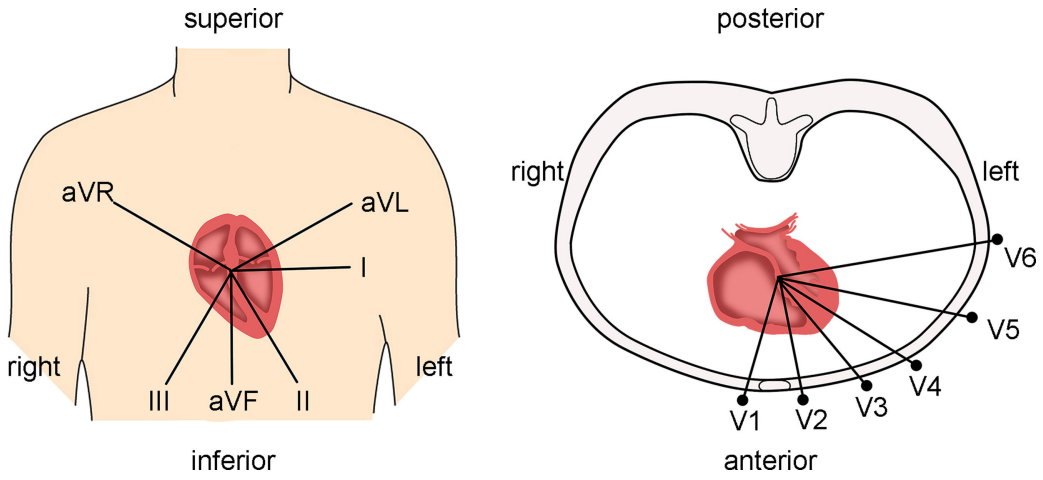

Figure I-4: ECG standard 12-lead axis orientations [59], [60].

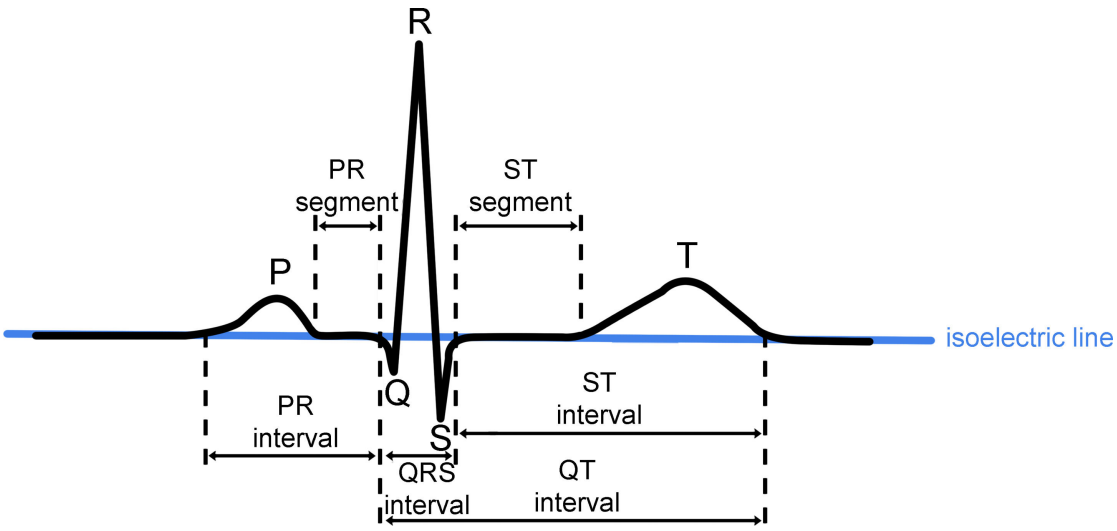

Figure I-5: ECG signal components [61].

become electrically excited and eventually cause either the contraction of the cells for pumping the blood out of the heart in the event named depolarization, or the relaxation of the heart in the event named repolarization. The negative ECG wave indicates that the biopotential is moving away from the lead, also during the electrical excitement of the heart in both events (depolarization and repolarization).

I.5. Applications of electrocardiogram

The ECG signal is usually stored as binary data, capable of being processed digitally for fast analysis and transmitted in a short period. Because digital technology advances have remarkably increased, signal processing applications have the benefit of enhancement and have led to involvement with big data with less effort. Many algorithms have been developed for

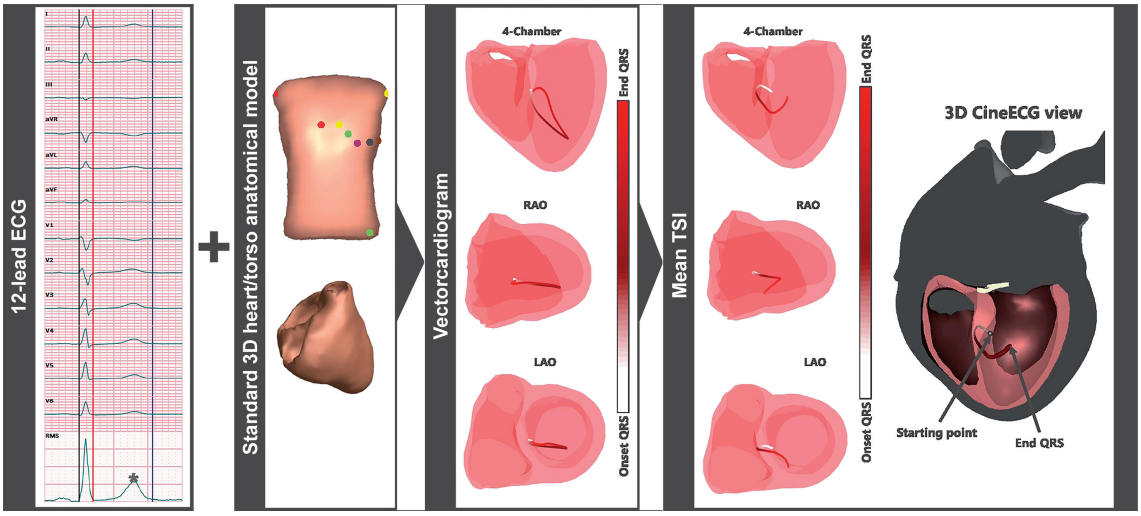

Figure I-6: Extraction of the trajectory of the QRS wave using Boonstra et al.'s method [62].

implementing big data for prediction purposes. The algorithms vary based on memory usage, interpretability, and the type of output. The criteria of the researcher decide the algorithm to work with. K-nearest neighbors (KNN) [63] and Naïve Bayes [64] for example are better in interpretability since they don't require complex learning computation. However, KNN requires more memory since it stores all the training data, unlike Naïve Bayes, neural networks, and support vector machines (SVM) where the training focuses on optimizing finite functions. The time complexity of the optimization also varies according to the number of parameters of the model. For instance, KNN has only one key parameter (k, the number of neighbors), making it computationally efficient during training. Naïve Bayes requires very few parameters, while SVM, functionally similar to a neural network with one hidden layer, has moderate complexity. In contrast, deep neural networks with multiple interconnected layers contain the highest number of parameters, drastically increasing their optimization time. However, a low number of parameters might introduce limitations to the algorithm, as Naïve Bayes and SVM are only classification algorithms, whereas KNN and neural networks can be used for both classification and regression. The available database [65] and objective of the research decides the type of output as being classification or regression. Currently, such research objectives focus on heart imaging, disease detection, biometric authentication, and emotion recognition.

I.5.a. Heart imaging

The visual reconstruction of the electrical activity of the heart is a practical option for the observation of the myocardial tissue in a computer-generated imagery using electrodes placed non-invasively on the skin. Recently, many studies worked on locating the source of the pacing site using methods based on neural networks [3], [66], [67], and heuristic approaches [68];

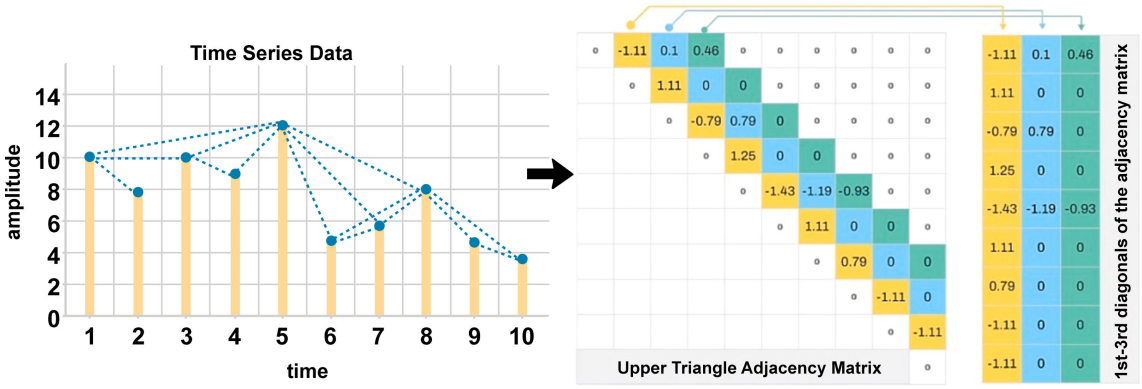

Figure I-7: Extraction of the adjacency matrix from the time series data [69].

others worked on identifying the site of ischemic changes [70], motion estimation of a beating heart [71], and the reconstruction of the position and orientation of the heart while being affected with respiratory motion [72]. Boonstra et al. [62] for example utilized the trajectory of the activation and recovery of the heart for identifying the anatomical location of the bundle branch block (BBB). For the extraction of the trajectory, they applied a process named "CineECG" [73] as illustrated in Figure I-6. The trajectory is built from the vectors of the heart potential movements named "mean temporo-spatial isochrone" (mTSI) [73], [74]. The direction of an mTSI vector follows a resultant named "vectorcardiogram" (VCG) [73], [74], which is extracted by adding the vectors directed between the position of each electrode and a chosen reference position in the heart. The difference between mTSI and VCG trajectories is that the stacked vectors of the mTSI trajectory have the same magnitude, which is the propagation velocity chosen as 0.7m/s, whereas the magnitude of each vector in the VCG trajectory follows the potential measured from the electrodes directing the vector. The classification of CineECG trajectories facilitated the discrimination between normal, right bundle branch block (RBBB), and left bundle branch block (LBBB) cases. However, their computations were based on a standard anatomical heart/torso model of a 58-year-old male rather than personalized models, which may affect the accuracy of the results because of differences in the heart anatomy and orientation of the patients. Therefore, they believe the measurement of the torso dimensions and the localization of the ECG electrodes using a 3D camera might increase the accuracy of their method.

I.5.b. Disease detection

Most of the focus in ECG processing research deals with the detection and classification of different cardiac pathologies since the heart is the most crucial organ in the human body, and all the tissues depend on the physiology of the heart in the delivery of blood full of nutrition.

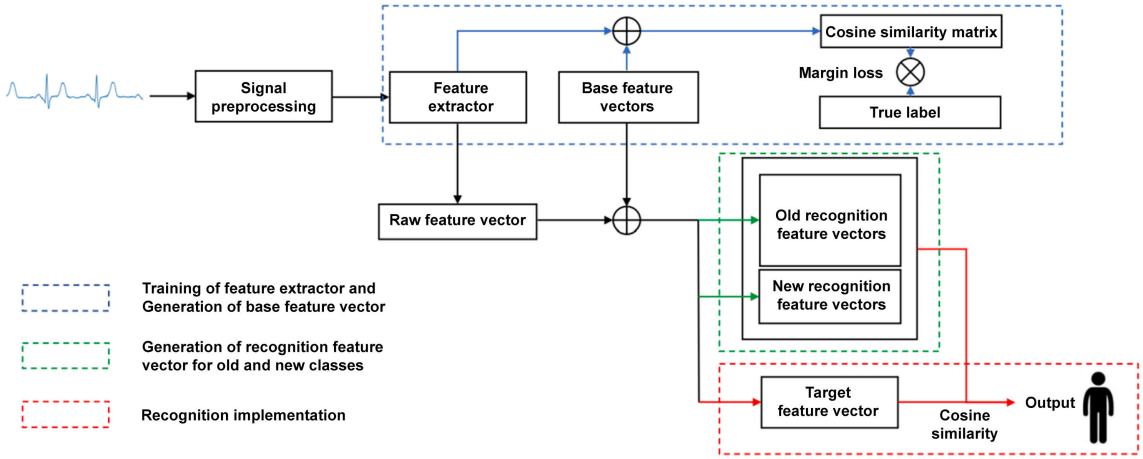

Figure I-8: Wang et al.'s model for biometric authentication [75].

Some applications include generating ECG signals for imbalanced data using generative adversarial networks (GANs) and transformers [76], classifying arrhythmia using convolutional neural networks (CNNs) and gated recurrent units (GRUs) [77], [78], and predicting sudden cardiac death using long short-term memory (LSTM) neural networks [7]. An example from Kutluana and Türker [69] includes ECG feature extraction using two methods based on natural visibility graph conversion. The algorithm natural visibility graph computes the relationship between each datapoint and the next datapoints based on human visibility, creating a matrix of adjacency of the datapoints as illustrated in Figure I-7. They proposed selecting the whole adjacency matrix as the first method for feature extraction, making it count $O(N^2)$ with datapoints of length N. The second method sums each row from the adjacency matrix into a single value to reduce the dimensionality of the features to O(N) (the same as the count of the datapoints). They applied their proposed feature extraction methods using ResNet and Inception models for a multi-label classification task (5 classes) and achieved an AUC score of 93.46% using ResNet as the classifier and the first method for feature extraction.

I.5.c. Biometric authentication

The advance of technology facilitates the accessibility to imitate individuals' identities, which has also raised a critical issue of user authentication. Simultaneously, biometrics are getting more involved in security concerns and user identification. Apart from finger, iris, and face recognition, researchers are also interested in applying the ECG signal as a biometric since its acquisition requires the presence of the living individual, making the ECG-based biometrics more secure and reliable. The related works in the literature implement CNN solely [79], or in collaboration with other feature extraction or classification methods such as phase space reconstruction (PSR) [80], scalograms [81], and LSTMs [82]. Wang et al. [75] developed an

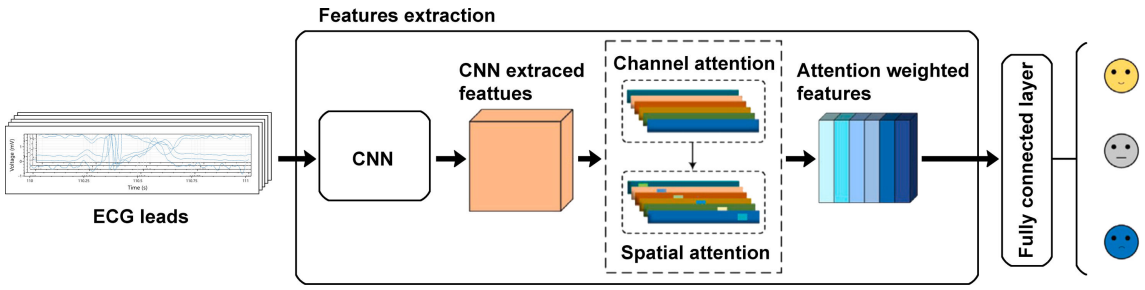

Figure I-9: Fan et al.'s model for emotion recognition [83].

approach for separating ECG beats from pre-delineated R peaks, and another for squeezing the separated ECG beats according to a chosen kernel size applied in the architecture of their designed CNN model. They used the squeezing technique as a flexibility advantage for identifying ECG beats with different lengths (heart rate variability), which equipped their model with the ability to classify ECG signals either at rest or after exercise. Figure I-8 summarizes the general steps of their method. The architecture of their model is also designed for appending new classes without the necessity of retraining the feature extraction parameters, but rather relying on storing the extracted features of the new classes. They applied their proposed method to ECGID [84], MITDB [85], and their private USSTDB databases and obtained an accuracy of 97.14%, 97.66%, and 95.54%, respectively.

I.5.d. Emotion recognition

The ECG signal can also vary according to the emotional state of the being since emotions influence the autonomic nervous system (ANS), which is responsible for regulating the heart rate. Patients' emotion monitoring can be beneficial in multiple scenarios such as tracking the negative effects of different drugs, the identification of stressors responsible for chronic stress, and reading the psychological category indirectly from the patient for a better treatment. Most of the previous studies worked on emotion recognition using multimodal signals, combining the ECG with electroencephalogram (EEG) [5], [26], [86], [87], galvanic skin response (GSR), also known as electrodermal activity (EDA) [87], [88], [89], skin temperature (ST) [88], and electromyogram (EMG) [89]. Fan et al. [83] worked instead on the ECG only. They applied an attention mechanism in a CNN model to mitigate an issue known as the differences in sensitivity to emotion-inducing sources of individuals. Figure I-9 presents the blocks and data processing tracks of their proposed method. For feature extraction, they applied six blocks of ResNet modules in which two CNN layers with a residual structure represent each block. Large convolution kernel sizes (17, 15, 13, 11, 9, 7) were chosen as they provided higher accuracies by experiment. As for the attention mechanism, the convolutional block attention module (CBAM) [90] was used to learn the importance of the extracted features from the six blocks. CBAM associates weights of attention in the channel and the spatial perspectives. Channel

attention learns the importance of the different simultaneously recorded signals (ECG leads) while spatial attention learns the important samples (parts) of the same signal (channel or ECG lead). Finally, the extracted features multiplied by their attention weights were fed to a fully connected layer for classification. They performed their proposed method on three datasets named WESAD [91], DREAMER [92], and ASCERTAIN [93] and obtained an accuracy of 96.5% using WESAD (4 classes), 83.6% and 84.2% for arousal and valence respectively using DREAMER (5 classes), and 68.0% and 64.5% for arousal and valence respectively using ASCERTAIN (7 classes).

I.6. Statistical study on electrocardiogram applications

To investigate the contributions of the proposed methods and the focus of the recent applications in the analysis of the ECG signals, statistical research is conducted using publicly available search engines to count the published articles with titles and abstracts mentioning selected keywords. Apart from ScienceDirect [94], PubMed [95], Constellate [96], and Google Scholar [97], Dimensions [98] provides better search tools and statistical information, allowing for counting yearly published articles according to the keywords searched for. The current study specified the analysis approach search keywords to “intelligence”, “machine learning”, and “neural network”; objective search keywords to “electrocardiogram”, “detection”, “classification”, “anatomy”, “imaging”, “disease”, “biometric”, and “emotion”; and limited the search time-span from 1980 to 2024. Dimensions’ search engine also provides a feature for combining multiple keywords using the Boolean operators “AND”, “OR”, and “NOT”. The results of the chosen combinations are displayed in Figure I-10, Figure I-11, and Figure I-12.

Additional comparisons between the neural network- and non-neural network-based approaches on ECG analysis are listed in Table I-1 and Table I-2. Table I-1 lists the decade’s most cited articles in the past five decades according to searched keywords related to ECG analysis, where the non-neural network approaches are listed on top and ordered chronologically from 1985 to 2010, while neural network-based approaches are listed below and ordered from 1990 to 2021. Table I-2 focuses more on the applications and the implemented datasets in the 4 aforementioned research objectives, namely imaging, disease detection, biometric authentication, and emotion recognition.

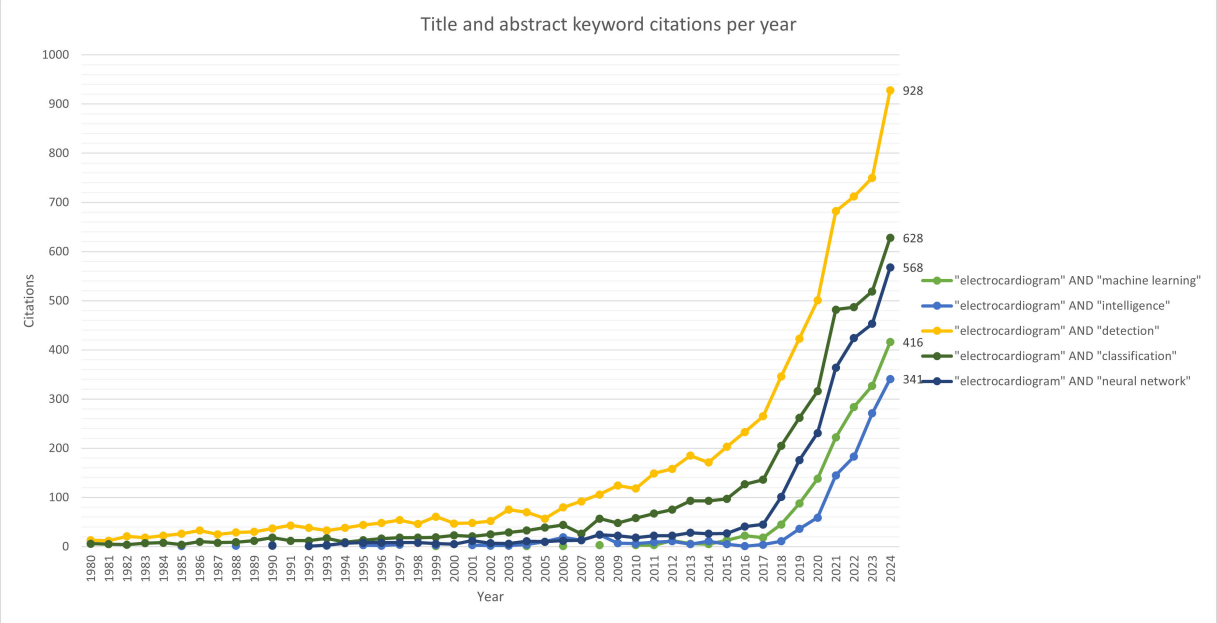

Figure I-10: Yearly interest in different approaches and objectives in ECG analysis since 1980.

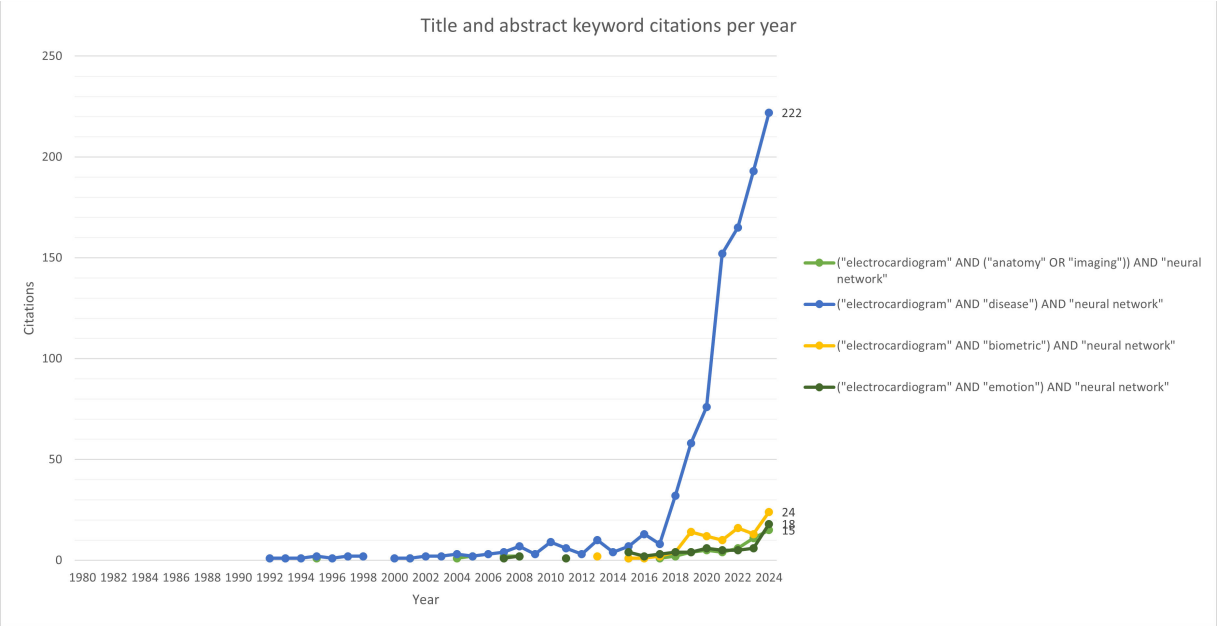

Figure I-11: Yearly interest in neural network applications in ECG analysis since 1980.

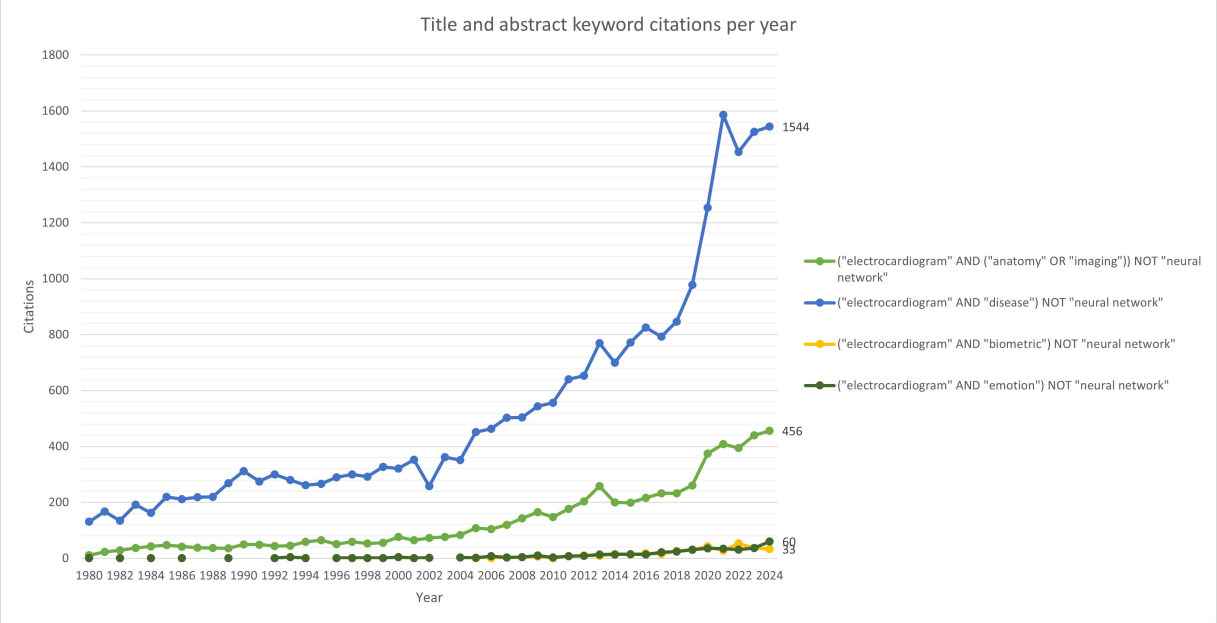

Figure I-12: Yearly interest in non-neural network applications in ECG analysis since 1980.

Table I-1: Methods and results of the decade's most cited articles in the analysis of ECG signals in the past five decades since 1980.

Author	Application	Method	Results	Keywords
Pan and Tompkins, 1985 [99]	QRS complex detection	Heuristic approach	• Accuracy: 99.3%	"detection"
Talmon et al., 1986 [100]	QRS onset and endpoint detection	Modified adaptive Gaussian filter	-	"classification"
Casale et al., 1987 [101]	Left ventricular hypertrophy detection	Heuristic logistic regression	• Accuracy: 77% • Sensitivity: 62% • Specificity: 92%	"detection"
Coast et al., 1990 [102]	QRS complex, P wave, and arrhythmia detection	Hidden Markov modeling analysis	• Sensitivity: 99.82%, 96.56%, 97.25% • Positive predictivity: 98.90%, 97.33%, 85.67% for QRS complex, P wave, and arrhythmia detection respectively	"classification"
Cuiwei Li et al., 1995 [103]	QRS complex, T, and P waves detection	Heuristic method based on DWT	• Accuracy: 99.8%	"detection"
Afonso et al.,1999 [104]	ECG beats detection	Heuristic approach based on Filter Banks decomposition	• Sensitivity: 99.59% • Positive predictivity: 99.56%	"detection"
De Chazal et al., 2003 [105]	Obstructive sleep apnoea detection	Linear and quadratic discriminants	• Minute-by-minute classification accuracy: 90%	"detection"
De Chazal et al., 2004 [106]	Heartbeat classification (normal sinus rhythm, ventricular ectopic beats (VEBs), supraventricular ectopic beats (SVEBs), fusion of normal and VEBs)	Linear discriminants	• Sensitivity: 75.9%, 77.7% • Positive predictivity: 38.5%, 81.9% for SVEBs, and VEBs respectively	"classification" AND "intelligence"
Niazy et al., 2005 [107]	QRS detection during functional magnetic resonance imaging (FMRI) (from the process of ballistocardiographic artifact removal)	Heuristic approach based on temporal principal component analysis	• Sensitivity: 99.27% • Specificity: 98.98%	"detection"

Table I-1: Continued.

Author	Application	Method	Results	Keywords
Khandoker et al., 2008 [108]	Obstructive sleep apnea syndrome detection	Wavelet decomposition and SVM	• Accuracy: 92.85%	"machine learning"
Jovic and Bogunovic, 2010 [109]	Heart rate variability classification	Random forest	• Average total classification accuracy: 99.7%, 99.6% for binary classification (normal, abnormal) and four (4) classes respectively	"machine learning"
Dassen et al., 1990 [110]	The localization of the accessory pathway of Wolff-Parkinson-White syndrome (6 locations)	Artificial neural networks	• Accuracy: 60%	"intelligence"
Stamkopoulos et al., 1998 [111]	ECG beats classification (normal and abnormal) for the detection of ischemic cardiac beats	Nonlinear principal component analysis and neural networks	• Accuracy: 80%, 90% for normal, and ischemic beats respectively	"classification"
Silipo and Marchesi, 1998 [112]	Arrhythmia classification (normal, ventricular ectopic beats, supraventricular ectopic beats)	Artificial neural networks	• Accuracy: 99%, 96%, 75% for normal, ventricular, and supraventricular ectopic beats respectively	"classification"
Kukar et al., 1999 [113]	Ischaemic heart disease detection	Neural networks	• Accuracy: 80% • Sensitivity: 82% • Specificity: 76%	"machine learning" AND "intelligence"
Pourbabaee et al., 2017 [114]	Paroxysmal atrial fibrillation detection	CNN + KNN	• Sensitivity: 90.20% • Specificity: 90.48%	"machine learning"
Hannun et al., 2019 [115]	Rhythm classification (12 classes)	CNN	• F1-score: 83.7%	"detection" AND "classification"
Attia et al., 2019 [116]	Asymptomatic left ventricular dysfunction detection	CNN	• Accuracy: 85.7% • Sensitivity: 86.3% • Specificity: 85.7%	"intelligence"
Attia et al., 2019 [117]	Atrial fibrillation and flutter detection	CNN	• Sensitivity: 79.0% • Specificity: 79.5% • F1-score: 39.2%	"intelligence" AND "machine learning"
Elayan et al., 2021 [118]	Arrhythmia classification	LSTM	• Weighted average: 97%	"detection" AND "intelligence" AND "machine learning"
Petmezas et al., 2021 [119]	Cardiovascular arrhythmia classification (normal, atrial fibrillation, atrial flutter, and AV junctional rhythm)	CNN + LSTM	• Sensitivity: 97.87% • Specificity: 99.29%	"classification"

Table I-2: Neural network- and non-neural network-based ECG analysis applications in the four aforementioned objectives.

Approach	Objective keyword	Author	Application	Dataset	Results
Neural network-based approach	Anatomy/imaging	Li and He, 2001 [66]	Origin of cardiac activation site localization	• Heart simulation model [120]	• Averaged localization errors for 24 testing sites being approximately equal to 3±1.5 mm
		Rajagopal et al., 2018 [67]	Imaging and reconstruction of endocardial potentials	• EDGAR [121]	• 0.327±0.221 Mv
		Gumpfer et al., 2021 [6]	Myocardial scar prediction	• Private dataset of 114 patients	• Sensitivity: 70% • Specificity: 84.3%
		Chen et al., 2022 [3]	Reconstruction of the electrocardiogram at the heart's surface	• Private dataset of five pigs	• Overall median of the correlation coefficient of the predicted ECG wave of 0.74
	Disease	Simon and Eswaran, 1996 [122]	Recognition of five different arrhythmia	• MITDB [85] • Glasgow ECG dataset • Waveforms scanned from Philips Cardioman manual [123]	• RBBB: 99.70% • AMI: 92.59% • PMI: 92.59% • LBBB:95.30% • Normal: 100%
		Yu and Chou, 2008 [124]	Classification of 8 different beat types	• MITDB [85]	• Accuracy of 98.71%
		Acharya et al., 2017 [125]	Detection of myocardial infarction	• PTBDB [126]	• Sensitivity: 95.49% • Specificity: 94.19%
		Huang et al., 2019 [127]	Classification of five different arrhythmias	• MITDB [85]	• Accuracy of 98.00%
		Lima et al., 2021 [128]	Mortality age prediction from the ECG-age	• Private CODE cohort [129] • CODE-15% cohort [130] • Private ELSA-Brasil cohort • SaMi-Trop cohort [131]	• p-value < 0.001
		Cui Et al., 2025 [2]	Classification of five different arrhythmias	• MITDB [85] • PTBDB [126]	• Precision: 99.11% • Recall: 98.82% on PTBDB
	Biometric	Zhang et al., 2017 [132]	Subject identification on 28 subjects	• CEBSDB [133] • Private WECG • Fantasia [134] • STDB [135] • MITDB [85] • AFDB [136] • VFDB [137]	• Accuracy: 93.5%
		Lynn et al., 2019 [138]	Human identification on 90 subjects	• ECGID [84] • MITDB [85]	• Accuracy: 98.60%
		Hammad et al., 2021 [139]	Human authentication on 290 subjects	• PTBDB [126] • CYBHi [140]	• Accuracy: 98.85%
		Srivastva et al., 2021 [141]	Biometric recognition on 113 subjects	• PTBDB [126] • CYBHi [140]	• Accuracy: 99.66%
		Maleki Lonbar et al., 2024 [4]	Identity verification on 18	• MITDB [85]	• Accuracy: 99.3%
	Emotion	Santamaria-Granados et al., 2019 [142]	Emotion recognition	• AMIGOS [143]	• Arousal accuracy: 81% • Valence accuracy: 71%
		Nita et al., 2022 [144]	Human emotion recognition	• DREAMER [92]	• Arousal accuracy: 85.56% • Valence accuracy: 95.16% • Dominance accuracy: 77.54%

Table I-2: Continued.

Approach	Objective keyword	Author	Application	Dataset	Results
Neural network-based approach	Emotion	Sedehi et al., 2025 [5]	Emotion recognition	• MAHNOB-HCI [145]	• Accuracy: 97.34±1.19%
Non-neural network-based approach	Anatomy/imaging	Pryor et al., 1993 [146]	Prediction of coronary anatomy	• Private dataset of 1030 patients	• C-index of 0.87 for significant of coronary artery disease • C-index of 0.78 for the severity of the disease
		Ramanathan et al., 2004 [147]	Reconstruction of the electrocardiogram at the heart's surface	• Private dataset of four subjects	• Location of pacing sites to within 7 mm (right ventricle) and 11 mm (left ventricle)
		Ortmaier et al., 2005 [71]	Measurement of heart motion for motion compensation of a beating heart in an invasive surgery	• Private dataset of five different beating-heart surgeries	• Mean measurement error in pixels (px) of 1.17 in x and 1.11 in y
	Disease	Martis et al., 2013 [148]	Classification of five different arrhythmias	• MITDB [85]	• Sensitivity: 99.97% • Positive predictive value: 99.21%
		Luo et al., 2016 [149]	Blood pressure measurement	-	• Average diastolic blood pressure < 4 mmHg mean absolute difference with the commercial device reading
		Elhaj et al., 2016 [150]	Classification of five different arrhythmias	• MITDB [85]	• Accuracy of 98.90%
		Houssein et al., 2021 [1]	Classification of five different arrhythmias	• MITDB [85]	• Accuracy: 98.26% • Sensitivity: 97.43%
	Biometric	Poon et al., 2006 [151]	Biometric approach on 99 subjects	• Private dataset of 99 subjects	• Half total error rate: 2.58%
		Wang et al., 2007 [152]	Human identification on 13 subjects	• PTBDB [126] • MITDB [85]	• Accuracy: 100%
		Chan et al., 2008 [153]	Person identification on 50 subjects	• Private dataset of 50 subjects	• Accuracy: 89%
		Arteaga-Falconi et al., 2016 [154]	Biometric authentication on 10 subjects	• MITDB [85]	• False acceptance rate: 1.41%. • True acceptance rate: 81.82%
		Farid et al., 2021 [155]	Biometric identification on 25 subjects	• Public dataset of 25 subjects [156]	• Accuracy: 100%
		Tanasković et al., 2025 [157]	Biometric identification on 202 subjects	• Public dataset of 202 subjects [158] • PTBDB [126]	• Accuracy: 97.2%
	Emotion	Tiller et al., 1996 [159]	The effect of positive emotions on heart rate variability	• Private dataset of 20 subjects	• p-value < 0.01
		Kim et al., 2004 [160]	Emotion recognition	• Private dataset of 50 subjects	• Three emotions accuracy: 78.43% • Four emotions accuracy: 61.76%
		Kim and Andre, 2008 [161]	Music-induced emotion recognition	• Private dataset of 3 subjects	• Subject-dependent accuracy: 90% • Subject-independent accuracy: 70%
		Chen et al., 2017 [162]	Driving stress detection	• Stress Recognition in Automobile Drivers [163]	• Sensitivity: 87.3% • Precision: 88.5%
		Sepúlveda et al., 2021 [164]	Emotion recognition	• AMIGOS [143]	• Arousal accuracy: 90.2% • Valence accuracy: 90.4%

I.7. Discussion

This overview highlights approaches in grouping the unlimited types of biological signals and introduces the recent applications of the most investigated signals such as the ECG signal. It also demonstrates research objectives implemented on the ECG signals specifically with a statistical study on the contribution of heuristic approaches, machine learning, and neural networks on the ECG signal processing. The statistics of research interest in ECG analysis displayed in Figure I-10 shows the ongoing ECG signal processing in "detection" and "classification" at a low rate with rare interests in "machine learning", "intelligence", and "neural network" from 1980 until 2017 which might refer to the first appearance of U-Nets in 2015 [165] that were used for biomedical image segmentation, and ResNets in 2016 [166] for handling the degradation of training accuracy in deep neural networks. Zooming into the neural network- and non-neural network-based approaches in the ECG analysis shown in Figure I-11 and Figure I-12, ECG signals were first utilized for disease detection and heart imaging, with rare applications in emotion recognition and biometric authentication, which is the case till 2024. Most of the published work represents case reports examining ECG signals along with other biological signals [167], [168], [169], [170] and less focus was considered on building autonomous systems for the ECG analysis until 2017 when neural network-based approaches showed promising abilities in arrhythmia classification and pathologies detection with less effort in the system design of the classifiers. Heuristic approaches on the other hand also present competitive results with values ranging from 77% to 99.8% in accuracy, from 62% to 99.82% in sensitivity, and from 92% to 98.98% in specificity against neural network approaches with values ranging from 60% to 99% in accuracy, from 82% to 97.87% in sensitivity, and from 76% to 99.29% in specificity in characteristic waves and pathologies detection as shown in Table I-1. Based on the application and method of the works listed in Table I-1, the autonomous ECG analysis systems have been proposed as heuristic-based approaches since 1985 by Pan and Tompkins [99], and as machine learning and neural network-based approaches since 1990 by Coast et al. [102] and Dassen et al. [110].

The listed works in Table I-2 address the familiarity of the research community with the various applications using the ECG signal since 1993 which introduce at least 14 different applications varying from the reconstruction of the ECG on the surface of the heart, to arrhythmia classification, biometric identification, blood pressure measurement, emotion recognition, and to mortality age prediction, etc. The implemented datasets are also diverse and mostly publicly available in the 4 aforementioned objectives, except for ECG-based imaging applications, which have EDGAR [121] as the only publicly available dataset to our knowledge. The performance of the proposed neural network- and non-neural network-based methods are

almost the same, with high accuracies ranging from 92.59% to 100% in disease detection and biometric authentication, and with low accuracies ranging from 61.76% to 97.34% in imaging and emotion recognition. However, challenges are still ongoing for building systems capable of generalizing over multiple applications, diverse datasets, and with a short running time.

From the previously published works in the literature, it is inferred that heart imaging is still facing generalization difficulties using the ECG signal, but rather relies on invasive techniques and additional cooperative technologies such as the 3D camera suggested in [62]. However, a combination of CineECG imaging and micro-computed tomography is found to be useful as an educational application for teaching cardiac anatomy [171] whereas ECG-gated computed tomography is also reliable for diagnostic purposes [172]. On the other hand, Machine learning applications to disease detection provide adequate precision values in ECG signal pattern recognition and multi-disease classification since the ECG signal holds important signs of most cardiac pathologies. Researchers focus on extracting these signs in addition to hidden patterns that could be revealed as features using proposed novel methods, such as implementing the convolutional neural network (CNN) architectures in classifying paroxysmal atrial fibrillation (PAF) and yielding an accuracy of 99.92% [173]. The classifiers for the extracted features are usually modified architectures of predesigned classifiers such as CNN, long short-term memory (LSTM), Transformers, or a simple artificial neural network (ANN).

Many studies also proved that ECG-based biometric authentication is showing a promising performance while handling individuals' heart rate variability and multi-session recognition [174], [175]. Yi et al. [176] for instance implemented a method based on CNN, an attention mechanism, and a domain adaptive feature fusion network and achieved an accuracy of 96.31% on the ECG-ID database. The same good results are also achieved using the electromyogram (EMG) analyzed with a model based on long short-term memory (LSTM) networks, yielding an accuracy of 99.17% on a database of 100 individuals [177]. Although, ECG-based emotion recognition achieved poor results, facing difficulties such as individuals' different sensitivity to stressors. Turchet et al. [178] performed an experiment of emotion recognition using ECG and EEG separately and jointly with support vector machine (SVM) as a classifier in a subject-independent classification task and achieved an accuracy of 86.86% using EEG, 14.77% using ECG, and 51.07% using EEG and ECG. Therefore, most studies combine the ECG with multiple biological signals such as the EEG, electrodermal activity (EDA), and respiratory responses (RESP) for emotion recognition [179], [180].

However, as much as the ECG signal is implemented in diverse applications, the ECG-based imaging, biometric authentication, and emotion recognition are still less inspected as displayed in Figure I-11 and Figure I-12. Also, machine learning algorithms are at an improvement pace, inspiring to involve more in the ECG analysis, allowing for multi-hidden-

patterns detection and multi-classification with less effort and less running time consumption, unlike heuristic approaches that are as high in accuracy as machine learning approaches but with limited abilities as shown in Table I-1 which implies that the challenges are still ongoing.

I.8. Conclusion

This chapter demonstrates the existence of unlimited types of biological signals and introduces ways of sorting such signals using suggested criteria such as the origin, the dynamic nature, and the physical form of the signal. Using these criteria, the ECG is defined as an endogenous dynamic biological signal of electric type. The objectives of the signal analysis vary mostly into imaging, disease detection, biometric authentication, and emotion recognition, where disease detection is more addressed than the other three objectives. However, diverse datasets are publicly available for the 4 objectives, except for imaging, which has EDGAR [121] as the only publicly available dataset to our knowledge.

Neural network- and non-neural network-based approaches are almost similar in accuracy. However, neural network-based approaches are getting easier to interact with and provide diverse architecture designs with strong generalizing abilities. Even though challenges are still ongoing with the 4 aforementioned objectives, especially with ECG-based imaging and emotion recognition.

Chapter II. Machine learning based ECG peak analyzer for WPW syndrome

II.1. Introduction

Naturally, the functionality of the heart follows a regular beat rhythm. Any long disorder in the rhythm of the beats may drain the strength of the heart and thus lead to sudden cardiac death [181], [182], especially if the rhythm increases as in the case of tachycardia [78], [183], [184], [185]. Early diagnosis of patterns of malfunction in the heart allows for choosing between multiple choices in the treatment process. One of these patterns is known as Wolff-Parkinson-White (WPW) pattern [186], [187]. The diagnosis of the WPW pattern considers three abnormalities in the electrocardiogram (ECG) signal of a patient (short PR, Delta wave, and prolonged QRS complex), it is also known as ventricular preexcitation [188], [189]. If a patient experiences tachyarrhythmia in combination with WPW pattern then the diagnosis refers to WPW syndrome [190], [191]. The incidence of the WPW pattern can occur at any age and is mostly witnessed in childhood [192]. Therefore, an automatic system dedicated to detecting pathological patterns such as WPW pattern in addition to the surveillance of ECG signals is a significant worth for the early diagnosis of heart pathologies, especially for detecting abrupt changes in the signal.

This chapter introduces an artificial intelligence-based method for robust detection of ECG waveforms (P, QRS, and T waves) across multiple lead types, using a single unified model. Our method adapts to diverse ECG signals without structural modifications, demonstrating its robustness. Additionally, we propose a novel technique to scan peaks for Wolff-Parkinson-White (WPW) pattern by precisely localizing the slurred upstroke named Delta wave rather than relying on time-interval ratios as seen in prior work.

Our approach compresses the input signal by extracting key statistical parameters, including the mean, min, max, standard deviation, and interquartile range to reduce computational complexity while preserving critical waveform features. These parameters guide the adjustment of two core functions: one for peak detection (P, QRS, T) and another for tangent deviation analysis (Delta wave identification). Machine learning models process extracted intervals and amplitudes from the scanned peaks to support decision-making, further reinforcing the method's robustness.

The rest of this chapter is organized as follows. Related works in ECG characteristic waves detection, arrhythmia classification, and Wolff-Parkinson-White pattern detection is covered in Section II-2. Section II-3 introduces generalities about the acquisition of the Electrocardiogram

(ECG), its structure, and its importance. It also introduces generalities about the Wolff-Parkinson-White pattern, its origin, characteristics, and similarities to other heart abnormalities. Section II-4 covers details of a function named "Peak analyzer", developed for peaks detection and tangent deviation, in addition to the seven steps proposed in our methodology for WPW pattern detection. The experiment and results using Neural Networks, Naïve Bayes, and K-Nearest Neighbors machine learning algorithms, with more detail about the structure of the models are presented in Section II-5. Also, the models of the experiment are evaluated using 122 signals from the MIT Arrhythmia database. A discussion about the obtained results is included in Section II-6, and Section II-7 concludes our study.

II.2. Related works

Most of the ECG analysis methods proposed in the literature rely on the detection of well-known waves (P wave, QRS complex, and T wave). Using Length Transformation (LT) and a function for threshold determination, Gritzali et al. [193] proposed a method for the detection of P, QRS, and T waves. The method gave significant results on the detection of QRS, and T waves, with difficulty in handling the detection of small amplitude P waves. Another method based on Shannon energy estimation and Hilbert transform [194] has shown good results in the detection of R peaks even in noisy and arrhythmic signals. Maršánová et al. [195] also proposed an algorithm dedicated to P wave detection using phasor transform. They also developed the same algorithm with some decision rules for the detection of P waves in the case of second-degree atrioventricular block pathology. Tuncer et al. [196] on the other hand extracted and compressed features from the whole signal using a method named "Discrete Wavelet-Concatenated Mesh Tree and ternary chess pattern", which is based on Discrete Wavelet Transform (DWT) and Local Ternary Pattern. They also used Neighbors Component Analysis (NCA) for features selection making it to 128 features as input, and they have shown good results in classifying the 17 different categories of ECG signals from the MIT Arrhythmia database in addition to the St Petersburg database. The method is developed from the previous study by Tuncer et al. [197] with changes in the configurations of the performed steps. Subasi et al. [198] also improved the method and gained a better performance using (max, min, and average) pooling for signal decomposition instead of Discrete Wavelet Transform, ternary and signum functions for features extraction, ReliefF and NCA for features selection, and Deep Neural Networks for the classification. They have obtained better results with 97.10% in accuracy in classifying the 17 arrhythmia classes of the MIT Arrhythmia database. Li et al. [199] proposed a method for the detection of the characteristic waves (P, QRS, and T waves); with also their onset and end. The method fundamentally functions on the deconstruction of the ECG

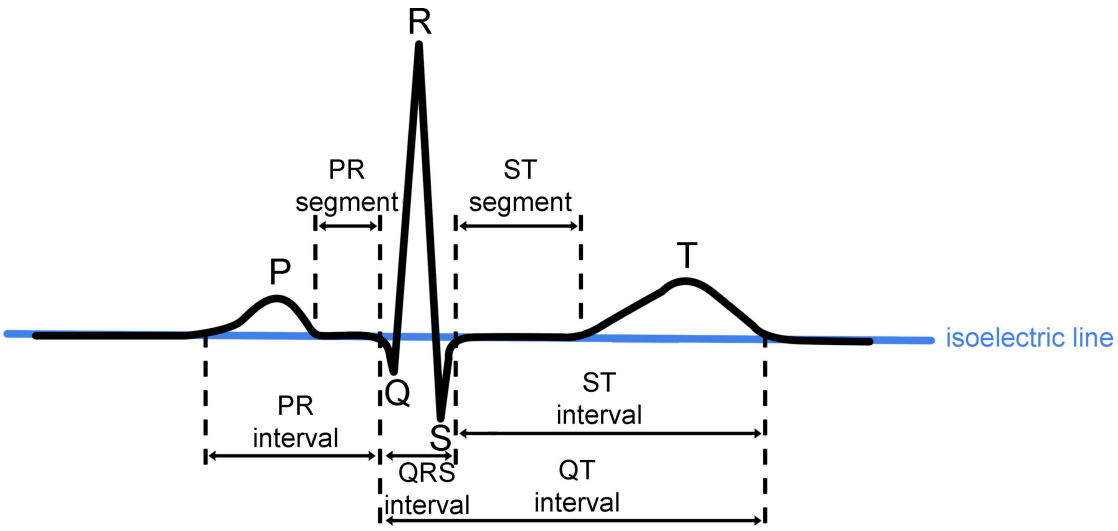

Figure II-1: ECG signal components **[61]**.

signal using Wavelet Transform and then extracting information from the second level of the DWT according to each wave detection with the help of predefined time windows and amplitude thresholds that are dedicated for each operation (wave peak, onset, or end detection). These predefined windows though make the method dependent on the type of the lead and the rhythm of the signal, which eventually takes off the robustness of the method. For WPW pattern detection, a method was proposed using wavelet transform and the absolute value of the tangent of the branch QR or QS according to which is higher [200]. They used wavelet transform for the detection of P, QRS, and T waves, and the absolute value of the tangent as an indicator of the existence of the slurred upstroke of Delta according to a predefined threshold. It checks the value (amp_R /QR) if $amp_R > amp_S$, or (amp_S /QS) if $amp_R < amp_S$. However, a decision made from this condition might confuse with other pathologic symptoms such as complete bundle branch block where QR is lengthened [201], [202]; ventricular hypertrophy where amp_R or amp_S are taller[22, 23]; or low QRS voltage [201], [202].

II.3. Wolff-Parkinson-White (WPW) pattern detection in Electrocardiogram

II.3.1. ECG components definition

Electrocardiogram (ECG) is a biological signal of electric type generated from the movement of heart activity. Such electrical signal is recorded using electrodes placed non-invasively on the skin of the body [203], [204]. The difference in potential between these electrodes creates different types of leads [58] (axes of different orientations with the same origin placed in the center of the heart) that exhibit the functionality of the heart (beat rate, heart

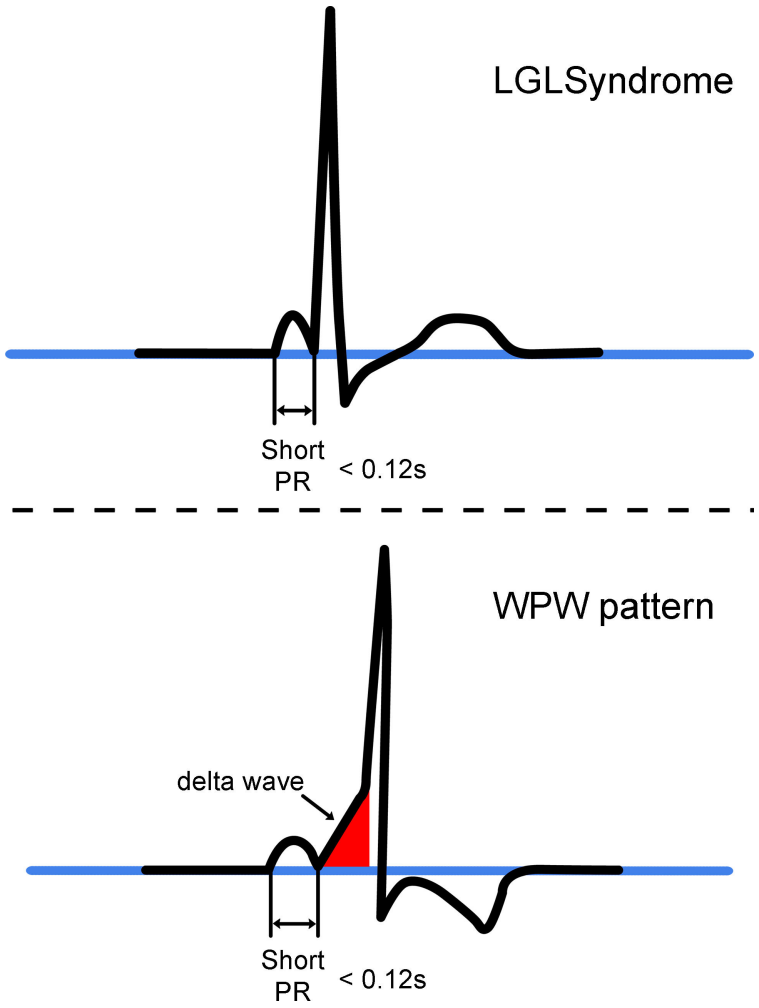

Figure II-2: Preexcitation syndrome **[201]**.

morphology, heart orientation, and also to diagnose many kinds of diseases) [205], [206], [207]. Most of the leads include three well-known waves of an ECG (P wave, QRS complex, and T wave) as shown in Figure II-1.

Scientists mainly consider the structure of these waves, their periods, and the interval between each of them. These three pieces of information alter according to the position of the heart, the morphology, and the manner the heart depolarizes and repolarize with [208]. For example, a positive peak (above the isoelectric line) indicates movements of the heart towards the lead and vice versa for a negative peak [209]. Different diseases also affect these three pieces of information; such affectation is useful in diagnosing the type of the disease. One of these affectations is “short PR interval” [210], which could indicate either “Wolff-Parkinson-White syndrome” or “Lown-Ganong-Levine syndrome” [211] as shown in Figure II-2. More on ECG is mentioned in detail and in a fun way with examples in the book “ECG Mastery Yellow belt” [201].

II.3.2. WPW pattern review

PR interval in normal sinus rhythm usually takes between 0.12 seconds to 0.2 seconds. A shorter period of this interval than 0.12 seconds refers to a disease named “preexcitation syndrome”. This kind of disease indicates an additional bundle called “Accessory Pathway” other than the normal bundle in the atrioventricular node (AV node) [212]. The accessory pathway conducts the impulse from the atrium to the ventricle faster than the normal one in the AV node, which excites the ventricular depolarization earlier than natural. In WPW syndrome, this early excitation distorts the shape of the QRS complex with a short ascending angle between Q and R peaks called “Delta wave”. This ascending slope prolongs the QRS complex duration and might be confusing as referring to the diagnosis of “complete bundle branch block” [201], [213]. More on WPW syndrome is covered in detail by K. James et al. [214].

II.4. Wolff-Parkinson-White (WPW) pattern detection methodology

The method proposed in our research consists of several steps with different algorithms. The objective is to find the slurred upstroke named “Delta” before the R peak, after the determination of short PR interval existence. Therefore, the process is arranged into seven steps (R peaks scan, false positive R removal, beat peaks scan, P and T peaks selection, short PR scan, slurred upstrokes scan, and Delta examination). Each step applies different filters to the input ECG signal, extracts some features, and provides them to a machine learning model either for manipulating a function of peaks detection named “Peak analyzer”, or selecting a desired appropriate feature of the signal.

II.4.1. Peak analyzer

ECG analysis depends on the morphology of the signal, and also on the location, the amplitude, and the rhythm of the characteristic peaks (P, QRS complex, and T peak). The detection of these peaks is essential in the process of ECG analysis. Thus, a function is developed with two main roles (peaks scan, and tangent deviation scan) for analyzing the morphology of the signal. Both functions’ task is placing labels in the signal samples. These labels are distinguished as up-peak, down-peak, or stable. The placement of the labels in the peaks scan function seeks for an amplitude ratio threshold (ART) and a horizontal time threshold (HT). The ratio of the amplitude is considered according to ($max - min$), which represents the amplitude interval, and the activation of its condition corresponds to a placement of up-peak or down-peak. Therefore, if the difference of amplitude between a sample of the signal and its previous scanned state is higher than ART, then this sample corresponds to an up-peak state, and vice versa for a down-peak as depicted in Figure II-3.

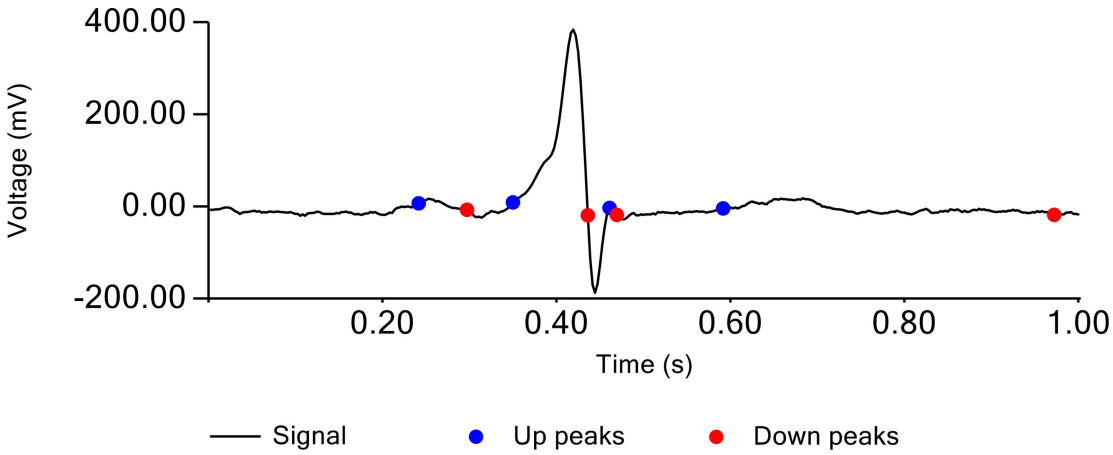

Figure II-3: One beat of ECG signal with up and down peaks as states of the signal after exceeding a threshold of 0.023% in amplitude from any last state.

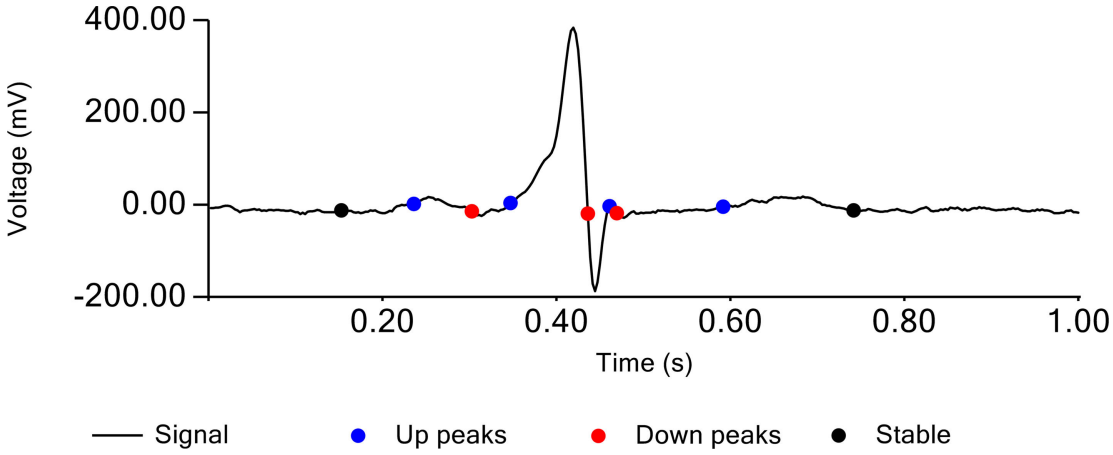

Figure II-4: One beat of ECG signal with previously placed up and down states in addition to the newly placed stable states after exceeding a horizontal threshold of 0.15sec from any last state.

Stable states of the signal correspond to the activation of the condition of HT. Therefore, if the absolute difference of amplitude between a sample of the signal and its previous scanned state is less than ART, and is apart from the same last state with a period greater than HT, then this sample corresponds to a stable state. Figure II-4 represents an illustration of implementing both thresholds (ART and HT) conditions.

A flow chart to these events is shown in Figure II-5 where $St_0 = [stable, 0, 0]$. St_k represents the k^{th} state of the signal x(n) at i^{th} sample, and it holds a vector with three elements (state label, its index "i", and its first appearance index). $St_{k-1}(1)$ is the sample index of $(k-1)^{th}$ state, for example if $St_{k-1} = [up, 43, 30]$, then $St_{k-1}(1) = 43$, and $St_{k-1}(2) = 30$. ART, HT are amplitude ratio threshold and horizontal threshold respectively. *ampInterval* is the amplitude interval of x(n).

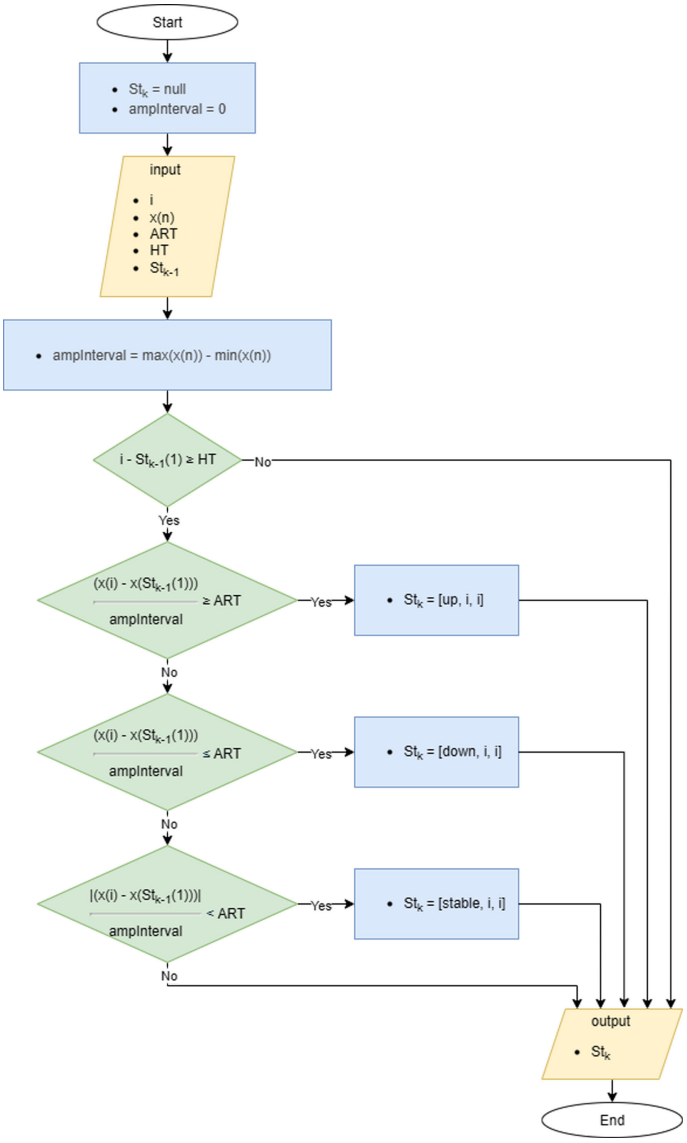

Figure II-5: Flow chart of signal peak detection.

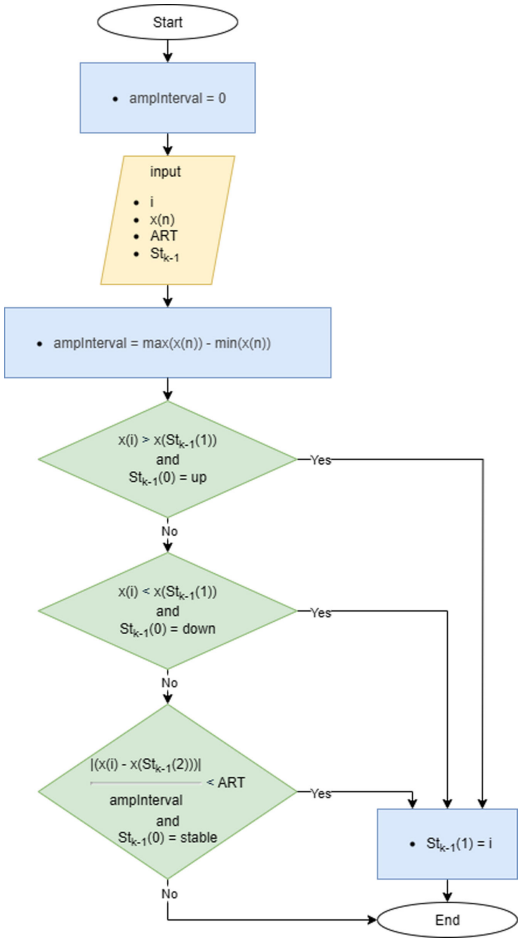

Figure II-6: Flow chart of signal peak position update.

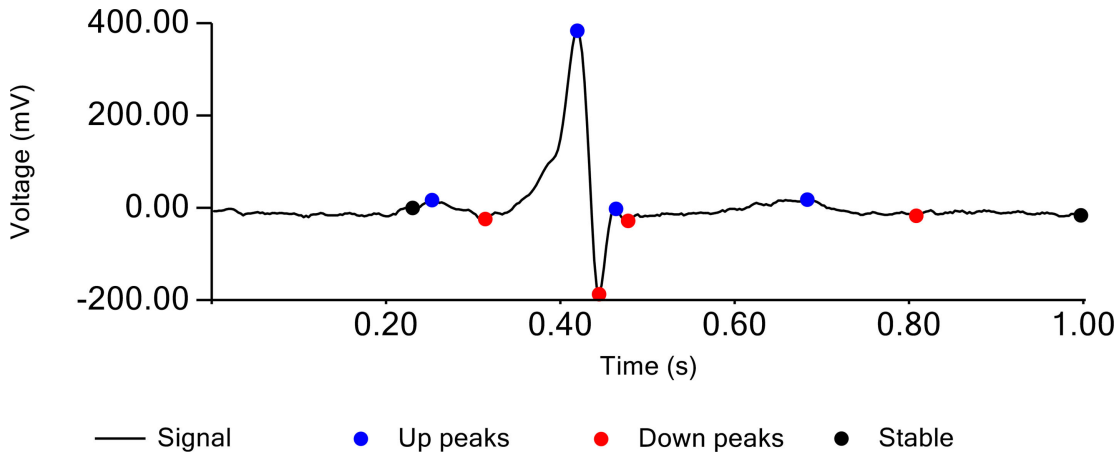

Figure II-7: One beat of ECG signal with the previously mentioned states placed in their correct position after applying the algorithm represented in Figure II-6.

Usually, the signal persists in the same state after crossing the threshold. Hence, the newly created state (last state) keeps updating the position index as depicted in Figure II-7 using the algorithm shown in Figure II-6.

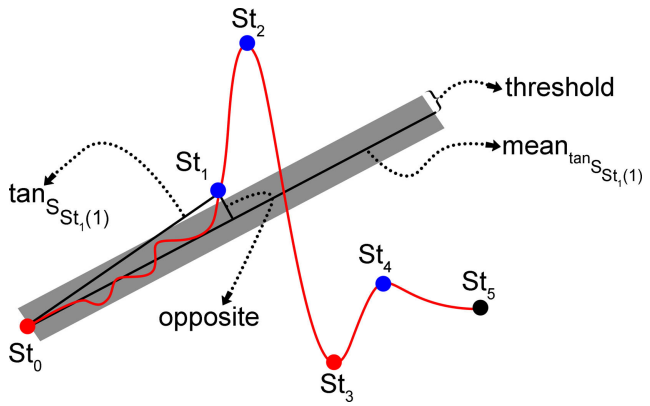

Figure II-8: Example of creating up-peak state (St_1) on the process of tangent deviation scan.

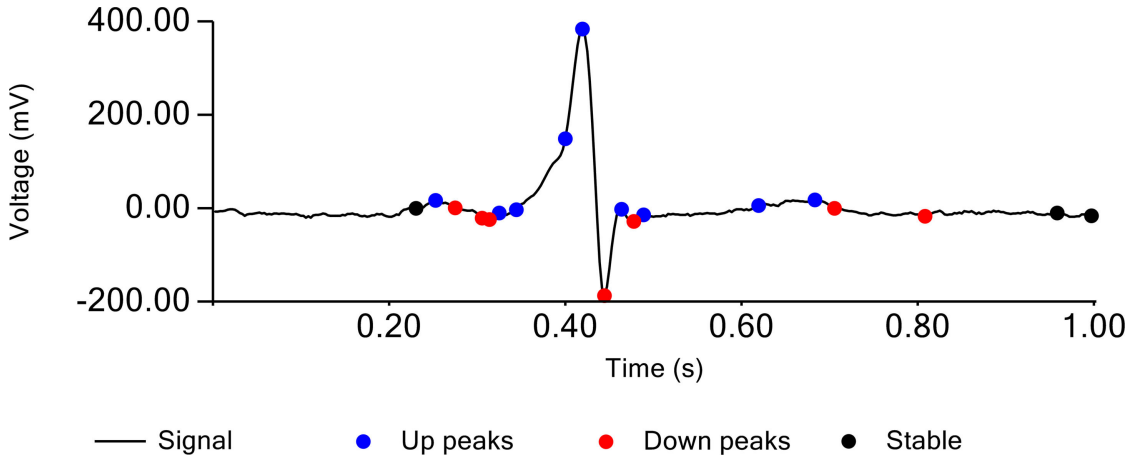

Figure II-9: ECG signal with the previously placed states in addition to tangent deviation scanned states with a threshold of 0.4%.

The tangent deviation scan depicted in Figure II-9 as the name indicates places new states at a position of the signal where a sample reaches a threshold in deviating from the mean tangent from the latest state as depicted in Figure II-8. The threshold is an amplitude ratio according to (*max* – *min*) of the signal, and the activation of its condition corresponds to the amplitude ratio of the opposite of an angle between a vector $\overrightarrow{S_{St_{k-1}(1)}S_i}$ and the mean tangent from the latest state as illustrated in Figure II-8 , where $S_i = [i, x(i)]$. The operation of the tangent deviation scan procedure consists of calculating the tangent of a vector $\overrightarrow{S_{St_{k-1}(1)}S_i}$ and the mean value of all the tangents of the curve enclosed between the borders of the vector $\overrightarrow{S_{St_{k-1}(1)}S_i}$, and is named as the mean tangent. The opposite of the difference in angle between the two tangents is then the deviation of the sample (S_i) from the mean tangent. Calculations of this procedure are sequenced as follows:

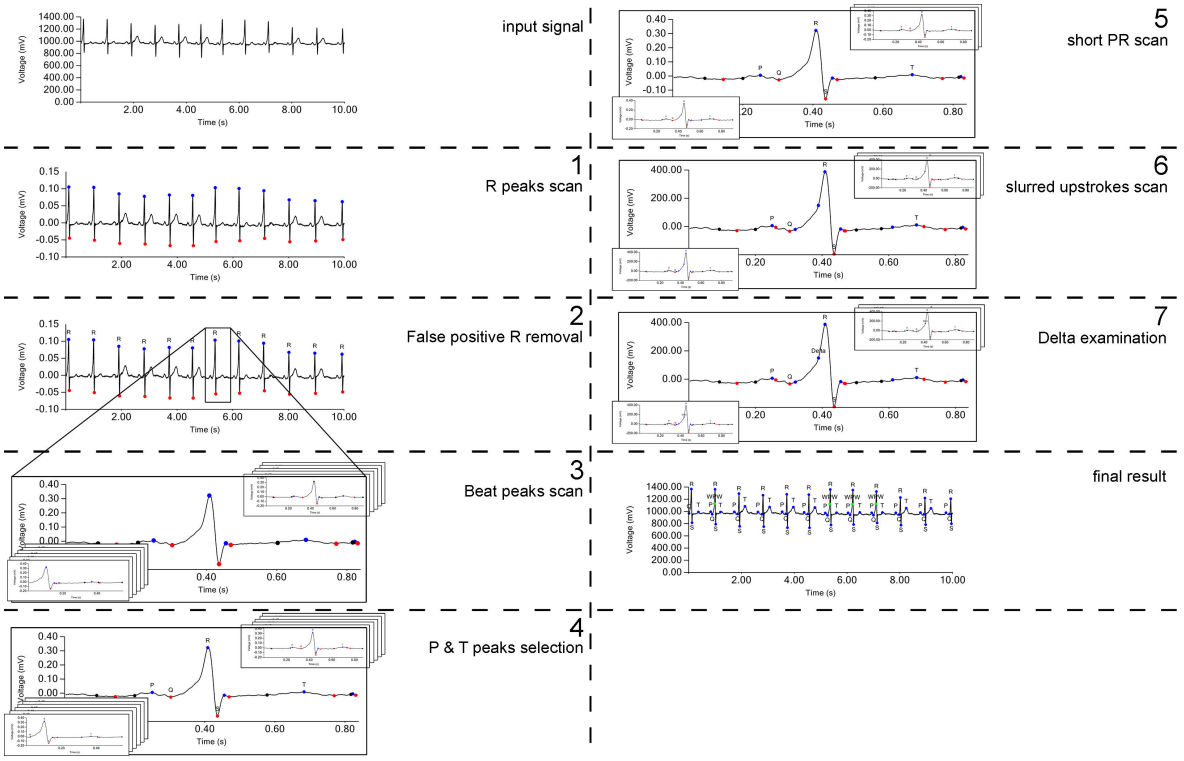

Figure II-10: General steps of the proposed WPW pattern detection method.

$$tan_{S_i} = \frac{x(i) - x(St_{k-1}(1))}{i - St_{k-1}(1)} \tag{II-1}$$

$$mean_{tan_{S_i}} = \frac{1}{i - St_{k-1}(1)} \sum_{r=St_{k-1}(1)+1}^{i} tan_{S_r} \tag{II-2}$$

$$\angle(tan_{S_i}, mean_{tan_{S_i}}) = tan^{-1}(tan_{S_i}) - tan^{-1}\left(mean_{tan_{S_i}}\right) \tag{II-3}$$

$$\overrightarrow{\|S_{St_{k-1}(1)}S_i\|} = \sqrt{(x(i) - x(St_{k-1}(1)))^2 + (i - St_{k-1}(1))^2} \tag{II-4}$$

$$opposite_{\angle(tan_{S_i}, mean_{tan_{S_i}})} = sin(\angle(tan_{S_i}, mean_{tan_{S_i}}))\ \overrightarrow{\|S_{St_{k-1}(1)}S_i\|} \tag{II-5}$$

II.4.2. Steps of the WPW pattern detection process

The general steps of the proposed method are arranged in Figure II-10. To better explain the functionality of our methodology, each step is fragmented separately.

II.4.2.1. R peaks scan

The system usually receives an ECG signal with multiple beats. However, working on each beat separately would simplify the tasks of the next steps. Thus, scanning for the most significant

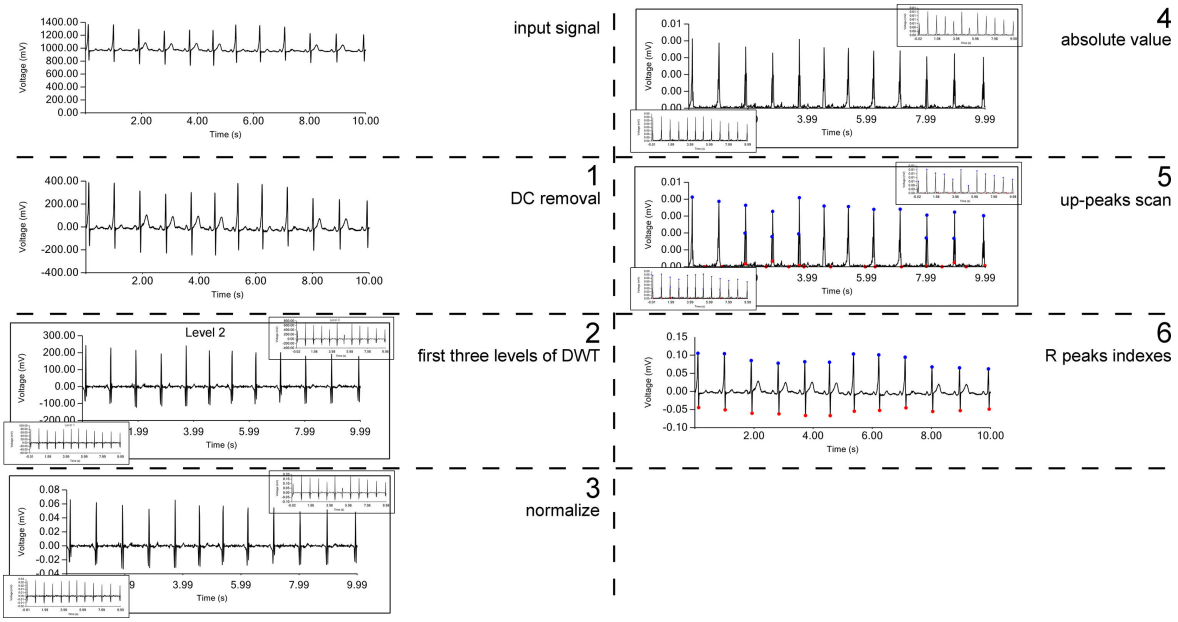

Figure II-11: R peaks scan in detail.

sign of a beat is the first step in the system. QRS complex is the most easily discovered wave in an ECG signal beat, and Discrete Wavelet Transform (DWT) is used for filtering only the high-frequency bands of the QRS complex.

Ordered in Figure II-11, this task comprises six steps; removing the DC component of the signal, applying DWT, normalizing the signal, taking the absolute value of the signal, and then passing the result to the function named "Peak analyzer" presented in Section II.3.1, which scans for states of the signal (up-peak, down-peak, or stable) according to amplitude and time threshold.

DC component removal is straightforward. The signal then passes through DWT for extracting high frequencies of the QRS complex. We try extracting only from the first level of DWT taking into account fewer computations. However, signals with high sampling frequency don't convolve well in exhibiting some QRS complex in the first three levels. Therefore, combining the result of the first three levels makes each level compensates for the others. The three levels then pass through the function named "Peak analyzer" after taking their absolute value; where it scans for signals states (up-peaks, down-peaks, stable). Any up-peak index in the input signal that is near to an up-peak index in one of the first three levels of DWT decomposition is likely considered an R peak.

II.4.2.1.1. DC component removal. It means the removal of the frequency 0 Hz, which is the mean value of the signal. The equation of DC removal of a signal x(n) is defined as:

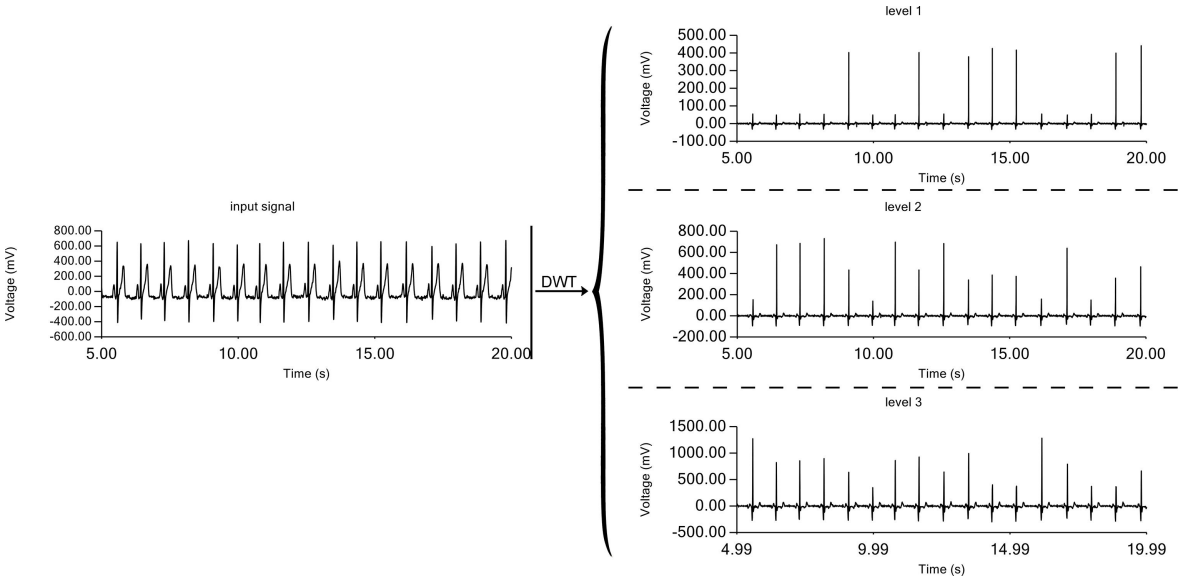

Figure II-12: ECG signal from "standard lead III" before and after applying DWT.

$$y(n) = x(n) - \frac{1}{N}\sum_{i=1}^{N} x(i) \tag{II-6}$$

II.4.2.1.2. Normalization of the signal. It is a way of scaling data so that all of its values are within the range of 0 to 1. The type of normalization method that is implemented in our approach is known as Min-Max normalization. Its formula is known as:

$$y(n) = \frac{x(n) - min\ (X)}{max(X) - min\ (X)} \tag{II-7}$$

where min(X) and max(X) are the min and max of the input signal x(n).

II.4.2.1.3. Absolute value of the signal. It transfers a signal x(n) to a positive signal that is denoted by |x(n)|. Its equation is defined as:

$$|x(n)| = \begin{cases} x(n), & if\ x(n) \geq 0 \\ -x(n), & if\ x(n) < 0 \end{cases} \tag{II-8}$$

II.4.2.1.4. *Discrete Wavelet Transform (DWT).* It is a transform that decomposes a discrete signal into several output signals, where each of them describes the input signal in a corresponding frequency band. Figure II-12 represents an example of applying DWT on an ECG signal. Each output signal is labeled with a number as its level, starting from the first level which represents the highest frequency band. Each band of the following levels covers half of the frequency band of its previous level *[215]*.

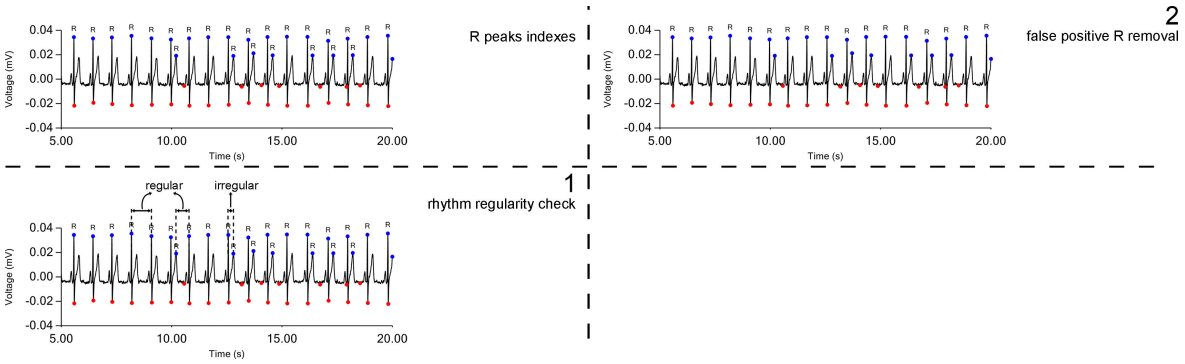

Figure II-13: False positive R removal in detail.

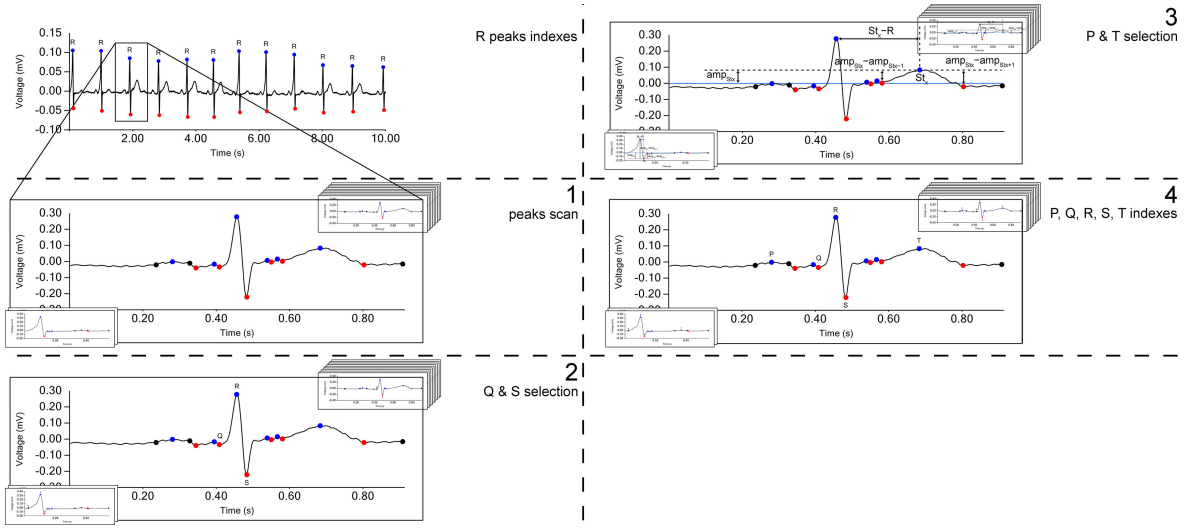

Figure II-14: Scan and selection of P, Q, S, and T peaks in detail.

II.4.2.2. False positive R removal

Some ECG signal leads present T waves in high amplitude close to that in the QRS complex, with an abrupt return to the isoelectric line, which might be selected as R peaks in the previous stage. Thus, in this stage, the system checks for the regularity of the selected R peaks rhythm. Then removes any miss-selected R peak that is out of the rhythm as illustrated in Figure II-13.

II.4.2.3. Beat peaks scan

After the selection of R peaks, each beat is then separated and passes through the same steps as in the first stage, except for taking DWT and the absolute value of the signal. Step 1 in Figure II-14 displays the result of beat peaks scan operation. In this stage, the function “Peak analyzer” is used for scanning all the peaks that are similar to what is included in P and T waves. Following the process of this scan, the next and previous peaks to the known R peak are naively selected as an S peak and a Q peak respectively.

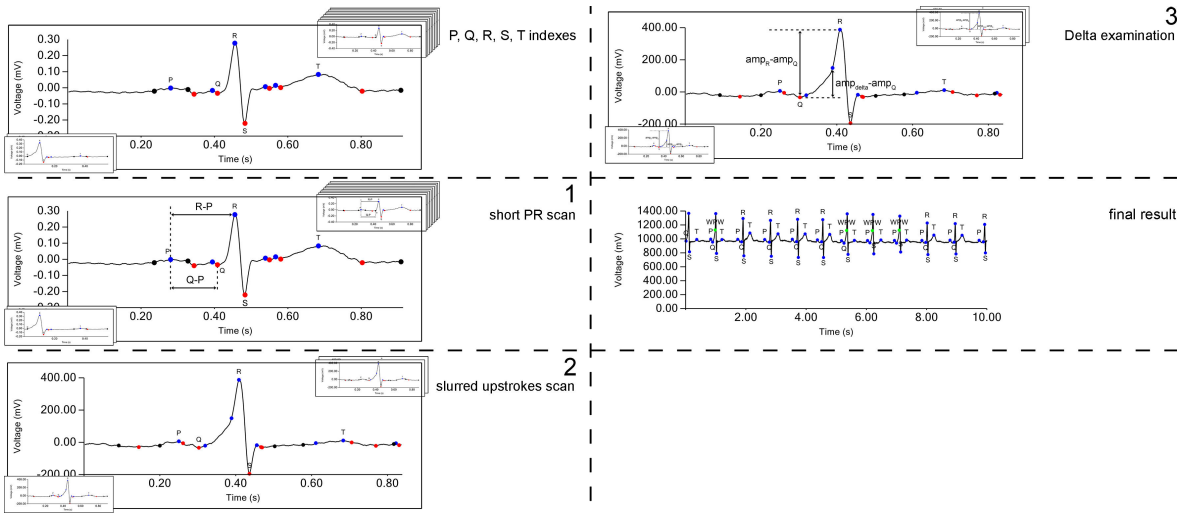

Figure II-15: Scan and examination of WPW pattern in detail.

II.4.2.4. P and T peaks selection

This stage considers the parameters that identify the position and amplitude of each state (up-peak, down-peak, stable) scanned from the previous stage (step 1 in Figure II-14). The position parameter is calculated as a ratio $(St - R)/(R - R_{prev})$, where $(St - R)$ is the interval between the scanned state and R peak, and $(R - R_{prev})$ is the interval between current and previous R peaks as illustrated in step 3 in Figure II-14. This ratio makes the position identity robust to rhythm changes of the signal. The states with parameters that are most probable to be P and T peaks are selected.

II.4.2.5. Short PR scan

This stage is straightforward, as it only considers the ratio $(Q - P)/(R - P)$, where $(Q - P)$ is the interval between Q and P peaks, and $(R - P)$ is the interval between R and P peaks. Step 1 in Figure II-15 well displays the concerned intervals. A low value of this ratio implies the existence of a short PR interval.

II.4.2.6. Slurred upstrokes scan

Beats that were identified as having short PR interval passes then to the function "Peak analyzer" for tangent deviation scan. This function states any deviation in the signal according to a selected threshold implementing the equations presented in Section II.3.1. Any state that is scanned before the R peak is considered the end of the slurred upstroke edge. A result of this operation is illustrated in step 2 in Figure II-15.

II.4.2.7. Delta examination

This stage checks if the selected state in the previous stage resembles the characteristics of the known slurred upstroke called "Delta". The ratio $(amp_{Delta} - amp_Q)/(amp_R - amp_Q)$ examines this condition, where $(amp_{Delta} - amp_Q)$ is the amplitude between the state considered as Delta and Q peak, $(amp_R - amp_Q)$ is the amplitude between R and Q peaks as illustrated in step 3 in Figure II-15. A high value of this ratio implies the existence of Delta.

II.5. Experiments and Results

For a quick and easy process of operating signals, we wrote a little sophisticated desktop application in "C#" using "Visual Studio". The application is uploaded to a repository in "GitHub" [216]. It is equipped with the materials mentioned before in our proposed methodology in addition to many other different tools for experimental purposes. The application is also equipped with three types of machine learning algorithms (Neural Networks, K-Nearest Neighbors [63], and Naïve Bayes [64]) in favor of performance comparison. Each of the previously discussed seven steps in WPW pattern detection is performed in a machine learning model. All of the steps follow the same chosen type of machine learning algorithm. Four steps solve classification problems, while the other three are for regression problems.

II.5.1. Dataset description

MIT Arrhythmia database is implemented as it consists of several types of cardiac pathologies recorded as an ECG signal in MLII lead (Modified Limb II lead). Even though, since our proposed machine learning models perform differently on the input ECG signal, where it passes through different stages with different input and output data, we had to create our dataset based on each ECG signal from the training dataset. Our customized dataset consists of 122 signals copied from the MIT Arrhythmia database. Each record contains the samples of 10 seconds of the signal, description data (starting of the signal, sampling rate, quantization steps in 1 mV) in addition to the ECG signal beats characteristics, and the labeled features extracted from the signal at each of the seven steps. More details are included in the supplementary data (Appendix A).

II.5.2. Architecture of the implemented models

The architectures of K-Nearest Neighbors (KNN) [63] and Naïve Bayes [64] models are simple and don't require optional customization. Except for the fact Naïve Bayes suits well only for classification problems. Thus, the output is split into 10 classes when applied to a regression problem. Also, the optimal value of K in KNN is chosen automatically depending on the training dataset. Neural Networks model architecture on the other hand is customizable. It is structured

in four layers (an input layer, two hidden layers, and an output layer). The number of neurons in the hidden layers is determined using the method proposed by Jeff Heaton [217], which is "The number of hidden neurons should be 2/3 the size of the input layer, plus the size of the output layer". The activation functions of the two hidden and output layers are "tanh", "linear", and "hard_sigmoid" respectively. The implementation of "tanh" is for expanding the values of input data, which is mostly condensed around zero. Whereas the other two activation functions are designed for prediction intent. Mean-Squared-Error is used as the loss function, and Stochastic-Gradient-Descent as the optimizer. All of the seven steps models follow the same architecture of the chosen machine learning algorithm. The differences are set in the input and output parameters. Some of the output parameters depend on the structure of the signal, and thus the statistical parameters of the signal are used as a way of defining the whole signal to the model as input parameters.

II.5.2.1. Statistical parameters

Statistical parameters are quantitatively calculated values for summarizing a set of collected data. Working with big data is always computationally expensive. Therefore, these kinds of parameters are used as a way of describing ECG signals. Such implemented parameters are mean, min, max, standard deviation (STD_DEV), and interquartile range (IQR). Standard deviation and interquartile range are chosen since standard deviation describes data according to the mean value, whereas interquartile range describes it according to the median. Min and max values are scanned from the signal in a straightforward procedure.

II.5.2.2. Input and output parameters at each step

II.5.2.2.1. Step 1: R peaks scan. The machine learning model in this stage controls the function "Peak analyzer" for choosing the appropriate amplitude ratio threshold (ART) and horizontal threshold (HT) for the input signal. Therefore, the input data is the statistical parameters (mean min, max, STD_DEV, IQR) of the normalized three levels of DWT of the input signal. The output is two continuous values ART and HT.

II.5.2.2.2. Step 2: False positive R removal. The removal of false positive selection of R peaks in this stage considers the amplitude and rhythm of the scanned R peak in the previous stage. The input data is the two ratios $(R_{cur} - R_{prev})/RR_{av}$ and $(amp_{R_{cur}}/amp_{R_{prev}})$, where $(R_{cur} - R_{prev})$ is the interval between current and previous scanned R peaks, RR_{av} is the average interval between scanned R peaks, $amp_{R_{cur}}$ and $amp_{R_{prev}}$ are the amplitude of current and previous scanned R peaks respectively. The output is a one-class value of either removing the current R peak or not. The choice of the two input ratios is taken so that the amplitude ratio would

compensate for the case of an arrhythmic R peak and gives it a higher chance of not being removed.

II.5.2.2.3. Step 3: Beat peaks scan. The input and output data of this stage are the same as in the first stage (R peaks scan). The difference is that the statistical parameters of the input data are taken from the normalized selected beat signal.

II.5.2.2.4. Step 4: P and T peaks selection. As mentioned in Section II.3.2.4, the position and amplitude of a scanned state affect its label of being P or T peak. Thus, the input data contains three values (position, amplitude, and difference in amplitude to nearby scanned states). The calculation of the position parameter is clarified in Section II.3.2.4. The difference in amplitude to nearby states is defined as $\frac{(amp_{St_k}-amp_{St_{k-1}})+(amp_{St_k}-amp_{St_{k+1}})}{2}$, where amp_{St_k} is the amplitude of the signal at state k. The third parameter (amplitude), is just amp_{St_k}, and is considered to compensate the second parameter if any miss-positioned states around existing. The output data is just two classes pointing to whether the selected state is P or T peak.

II.5.2.2.5. Step 5: Short PR scan. The input data in this stage is the ratio *(Q – P)/(R – P)*, which is explained in Section II.3.2.5. The output is one class indicating whether short PR exists or not.

II.5.2.2.6. Step 6: Slurred upstrokes scan. The model in this stage controls the function "Peak analyzer" for choosing the appropriate amplitude ratio threshold (ART) for tangent deviation according to the statistical parameters of the signal and how much is the PR interval short. Hence, the input data is the five statistical parameters of the signal and the ratio *(Q – P)/(R – P)*. The output is the continuous value ART.

II.5.2.2.7. Step 7: Delta examination. Checking the characteristics of scanned slurred upstrokes from the previous stage considers the ratio $(amp_{Delta} - amp_Q)/(amp_R - amp_Q)$ explained in Section II.3.2.7. However, the value of this ratio depends also on the type of the recorded ECG lead (the structure of the signal). Therefore, the input data in the model of the current stage is the statistical parameters of the beat signal in addition to this ratio. The output is one class of the existence of WPW syndrome.

II.5.3. Evaluation metrics

Evaluation metrics of classification models are given as accuracy (Ac), sensitivity (Se), and specificity (Sp), their values are determined as follows:

$$Ac = \frac{TP + TN}{TP + FP + FN + TN} \tag{II-9}$$

$$Se = \frac{TP}{TP + FN} \tag{II-10}$$

$$Sp = \frac{TN}{TN + FP} \tag{II-11}$$

where TP is True Positive, TN is True Negative, FP is False Positive, and FN is False Negative.

The Mean Absolute Scaled Error (MASE) on the other hand is suitable for evaluating regression models because of its resistance to different data scales, and effectiveness against zero value outputs. However, any result tending to infinity due to the stability of actual outputs is ignored, and replaced with the preceding real value. The prediction of the first sample is also ignored for the simplicity of the formula, which is computed as follows:

$$MASE = \frac{1}{N-1}\sum_{i=2}^{N}\left|\frac{A_i - F_i}{A_i - A_{i-1}}\right| \tag{II-12}$$

where A_i is the actual value and F_i is the forecast or predicted value.

II.5.4. Results

Nine cross-validation configurations are applied to the three machine learning algorithms for evaluating the ability of the models in an imbalanced dataset. The dataset includes 21 signals diagnosed with WPW patterns and 101 signals in normal sinus rhythm (NSR). The signals are ordered for being as equally distributed as possible across the dataset using a shuffling function that runs before the validation. Each validation experiment performs the same previously mentioned steps. Results are represented in the three following tables, where “NN”, “NB”, and “KNN” are Neural Networks, Naïve Bayes, and K-Nearest Neighbors respectively, “Ac”, “Se”, and “Sp” are accuracy, sensitivity, and specificity respectively.

Table II-1 represents a comparison in the performance of three machine learning algorithms (Neural Net, Naïve Bayes, and KNN) in 9 different cross-validation configurations, where the evaluation metric values are computed as the mean accuracy, sensitivity, and specificity of the steps solving classification tasks (false positive R removal, P and T peaks selection, short PR scan, and Delta examination). The mean MASE of the steps R-peaks scan, beat peaks scan, and slurred upstrokes scan represent the evaluation metric of the steps solving regression tasks. Table II-3 is an extension of Table II-1, including a comparison in running time of the performed validation techniques of the three machine learning algorithms.

Table II-1: Overall performance of Neural Net, Naïve Bayes, and KNN models on different validation techniques on 122 signals from the MIT Arrhythmia database.

Evaluation metric	Accuracy (%)			Sensitivity (%)			Specificity (%)			MASE		
Validation configuration	**NN**	**NB**	**KNN**	**NN**	**NB**	**KNN**	**NN**	**NB**	**KNN**	**NN**	**NB**	**KNN**
Holdout cross-V (75% training)	99.25	74.55	99.11	97.16	53.67	94.64	74.37	48.79	74.37	2.33	5.39	1.26
3-fold cross-validation	98.47	81.23	98.33	90	46.91	86.9	74	57.84	74.07	1.24	5.63	1.16
4-fold cross-validation	98.32	79.76	98.36	87.33	49.77	87.02	74.02	55.82	74.11	1.6	5.47	1.04
5-fold cross-validation	98.22	77.35	98.4	87.74	46.12	86.8	73.88	53.56	74.16	2.05	5.73	1.13
6-fold cross-validation	98.38	78.31	98.33	87.08	51.33	86.97	74.1	53.98	74.07	1.39	5.92	1.02
7-fold cross-validation	98.08	77.76	98.4	82.94	52.47	86.99	74.03	53.22	74.15	1.08	4.94	1.16
8-fold cross-validation	98.46	76.6	98.3	89.64	50.39	86.81	74.02	52.17	74.05	1.16	7.95	1.03
9-fold cross-validation	98.48	75.75	98.37	88.87	48.29	86.86	74.08	51.49	74.13	1.94	4.87	0.93
10-fold cross-validation	98.38	76.54	98.31	88.66	50.53	86.82	74	52.08	74.06	1.28	4.89	1.12

Table II-2: Validation of the highest recorded precision of Neural Net, Naïve Bayes, and KNN models in detail at each step on 122 signals from the MIT Arrhythmia database.

Dataset description	122 signals (21 of WPW and 101 of NSR)								
Model type		**Neural Net**			**Naïve Bayes**			**KNN**	
Validation configuration		Holdout cross-V (75% training)			3-fold cross-validation			Holdout cross-V (75% training)	
Running time		30 min, 15 sec			1 second			1 min, 19 sec	
Model label	**Dataset size**	**MASE/ Ac (%)**	**Se (%)**	**Sp (%)**	**MASE/ Ac (%)**	**Se (%)**	**Sp (%)**	**MASE/ Ac (%)**	**Se (%)**	**Sp (%)**
R-peaks scan	122	0.71	-	-	2.94	-	-	0.64	-	-
False positive R removal	~1418	99.44%	100%	99.42%	94.09%	0%	100%	99.19%	100%	99.13%
Beat peaks scan	~1410	5.48	-	-	11.13	-	-	2.01	-	-
P and T peaks selection	~20678	98.71%	88.63%	99.32%	89.67%	12.79%	94.51%	97.53%	78.55%	98.69%
Short PR scan	~1410	98.83%	100%	98.75%	41.15%	74.84%	36.85%	99.71%	100%	99.68%
Slurred upstrokes scan	~480	0.80	-	-	2.79	-	-	1.13	-	-
Delta examination	~480	100%	100%	0%	100%	100%	0%	100%	100%	0%

Table II-3: Running time of the performed validation techniques of Neural Net, Naïve Bayes, and KNN models.

	Running time		
Validation configuration	**NN**	**NB**	**KNN**
Holdout cross-V (75% training)	30 min, 15 sec	1 sec	1 min, 19 sec
3-fold cross-validation	54 min, 4 sec	1 sec	4 min, 24 sec
4-fold cross-validation	1 hr, 17 min, 4 sec	1 sec	4 min, 59 sec
5-fold cross-validation	1 hr, 8 min, 49 sec	1 sec	5 min, 21 sec
6-fold cross-validation	1 hr, 52, 27 sec	1 sec	5 min, 40 sec
7-fold cross-validation	1 hr, 54 min, 20 sec	1 sec	5 min, 49 sec
8-fold cross-validation	2 hr, 1 min, 55 sec	1 sec	6 min, 25 sec
9-fold cross-validation	2 hr, 9 min, 44 sec	1 sec	6 min, 23 sec
10-fold cross-validation	2 hr, 11 min, 16 sec	1 sec	6 min, 30 sec

Table II-4: Running time and Figure 14 labels references of the automatic annotation of the test dataset using our method in Neural Networks, Naïve Bayes, and KNN.

		Neural Networks		Naïve Bayes		KNN	
Evaluation paradigm	**Signal name**	**Label**	**Running time**	**Label**	**Running time**	**Label**	**Running time**
Intra-patient	112m (1)	Figure 14 (a)	14 seconds	Figure 14 (c)	1 second	Figure 14 (e)	6 seconds
	113m (3)	Figure 14 (b)	8 seconds	Figure 14 (d)	1 second	Figure 14 (f)	3 seconds
	230m (0)	Figure 14 (g)	7 seconds	Figure 14 (i)	1 second	Figure 14 (k)	3 seconds
	230m (1)	Figure 14 (h)	9 seconds	Figure 14 (j)	1 second	Figure 14 (l)	4 seconds
Inter-patient	112m (1)	Figure 15 (a)	45 seconds	Figure 15 (c)	1 second	Figure 15 (e)	7 seconds
	113m (3)	Figure 15 (b)	33 seconds	Figure 15 (d)	1 second	Figure 15 (f)	2 seconds
	s0351lre_V6	Figure 15 (g)	9 seconds	Figure 15 (h)	1 second	Figure 15 (i)	3 seconds

Table II-2 is a zoom-in to the cross-validation configurations with the highest precision reached from each of the three machine learning algorithms, which are holdout cross-validation for Neural Net and KNN; 3-fold cross-validation for Naïve Bayes. The detail includes the dataset size, accuracy, sensitivity, specificity, and the mean absolute scaled error (MASE) of each step (Models labels). Due to the different precisions of the models in scanning the peaks of the signals, the sizes of the datasets starting from the second step (false positive R removal) to the last step (Delta examination) are represented as approximations since each model tunes the ART, HT, and TDT differently. The values in the column "MASE/Ac(%)" represent either MASE or accuracy according to the task of the step as being regression or classification respectively. Sensitivity and specificity cells are kept empty in the table for the steps with regression tasks.

The signals in Figure II-16 and Figure II-17 represent five samples used as test dataset for the three types of models. The models implemented for Figure II-16 results are trained with 127 samples without the test dataset. However, the evaluation paradigm is an intra-patient paradigm, which means that other parts of the test dataset are included in the training dataset. The chosen four samples are NSR signals (112m (1), 113m (3)), and WPW signals (230m (0), 230m (1)) from the MIT Arrhythmia database. Results in Figure II-17 are obtained using an inter-patient paradigm as an evaluation where the subjects in the training dataset are completely different from the subjects in the test dataset. The models are trained with 114 samples. The training dataset is chosen as two samples of NSR signals (112m (1), 113m (3)) from the MIT Arrhythmia database, and one sample of WPW signal (s0351lre_V6) from "PTB Diagnostic ECG Database". More information about running time, the signal name, and the model type of the results shown in Figure II-16 and Figure II-17 are included in Table II-4.

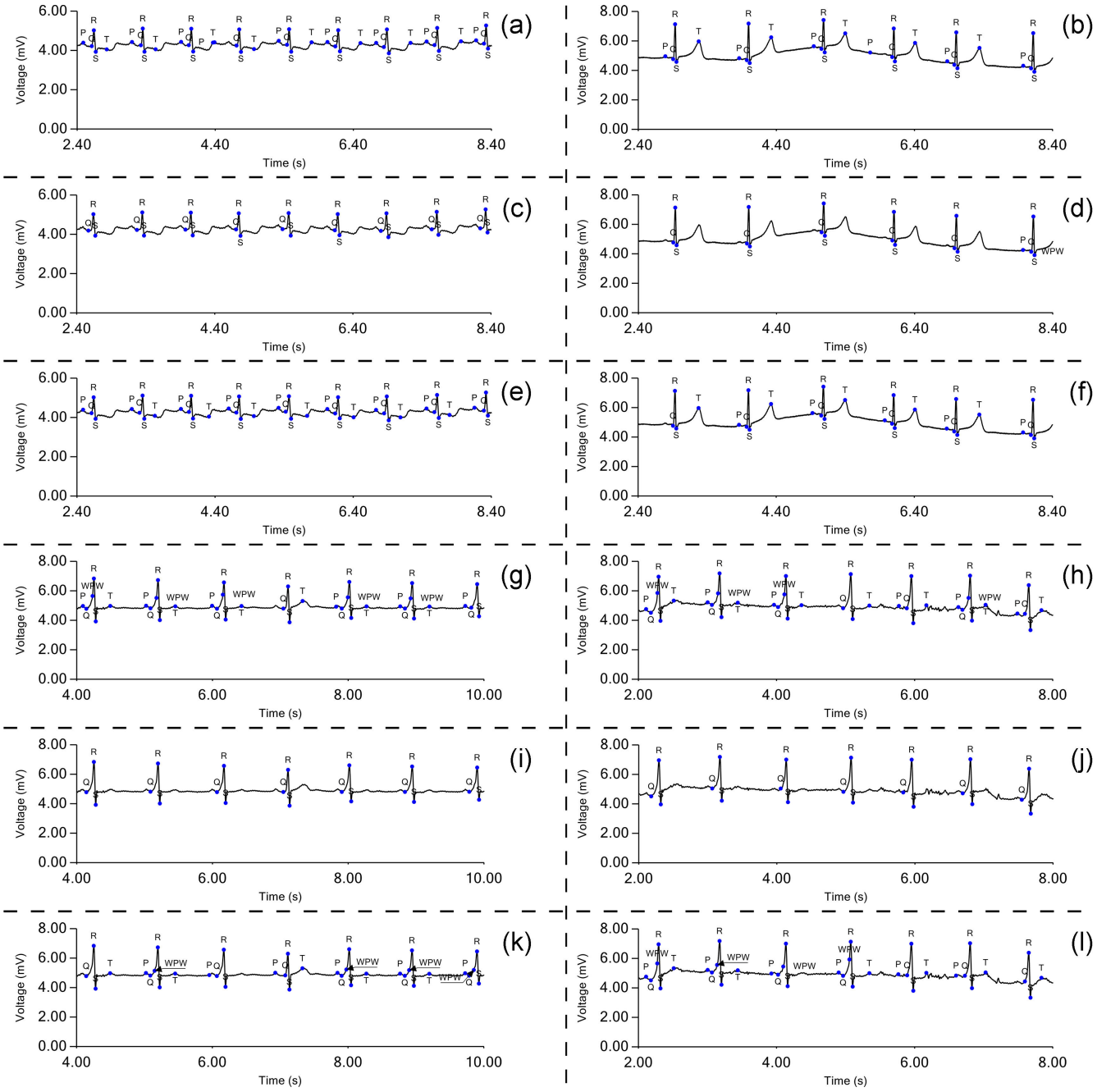

Figure II-16: Intra-patient paradigm evaluation results of testing the proposed method in automatically annotating four signals in Neural Networks, Naïve Bayes, and KNN.

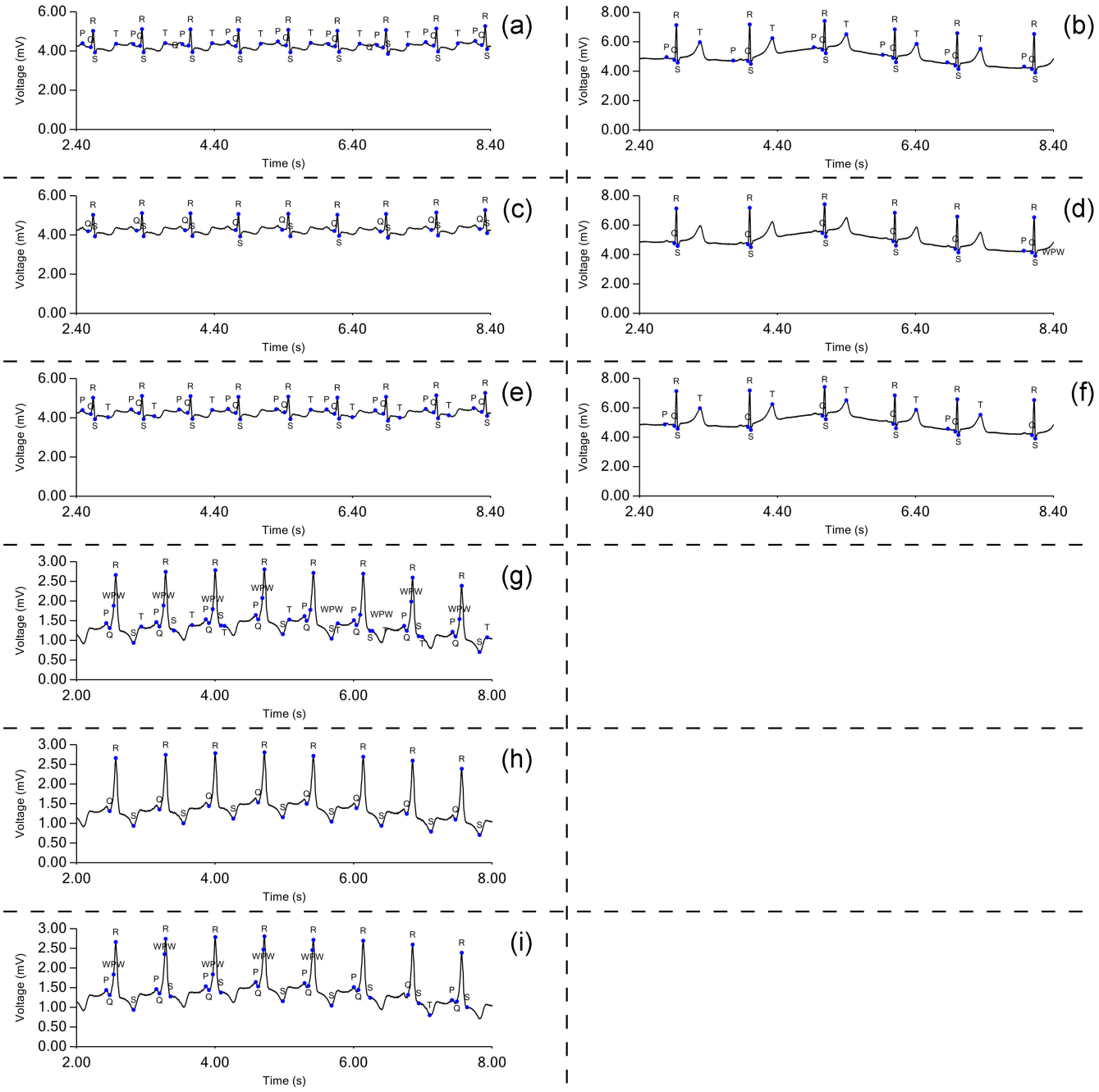

Figure II-17: Inter-patient paradigm evaluation results of testing the proposed method in automatically annotating three signals in Neural Networks, Naïve Bayes, and KNN.

Table II-5: Eigenvectors (loading scores) of PCA "Beat peaks scan".

	Eigenvectors				
Feature name	**PC1**	**PC2**	**PC3**	**PC4**	**PC5**
mean	0.24	0.88	$2.1\ 10^{-13}$	-0.39	0
min	0	0	0	0	0
max	$-1.1\ 10^{-14}$	$-2.4\ 10^{-13}$	1	$6.5\ 10^{-15}$	0
STD_DEV	-0.72	-0.09	$-2.7\ 10^{-14}$	-0.67	0
IQR	-0.64	0.45	$9.7\ 10^{-14}$	0.62	0

II.6. Discussion

This chapter proposes a new method for scanning the characteristic peaks (P, QRS, and T) of the ECG signal using the proposed algorithm named "Peak analyzer" which can be tuned according to the morphology of the signal for extracting the main curving points of the signal, in addition to the deviation of the curves for delineating the Delta wave of the Wolff-Parkinson-White pattern. The scanned peaks are then classified using machine learning algorithms that also reinforce the robustness of the proposed method. The result of the validation in different techniques from Table II-1 shows that the evaluation of Neural Networks and KNN are both almost identical across different cross-validation configurations (k-fold and holdout) with a small random alternation in accuracy, specificity, and MASE with a variance of 0.095, 0.015, and 0.175 respectively for Neural Networks; and with 0.058, 0.008, and 0.008 respectively for KNN. The high alternations appear in sensitivity with a variance of 12.51 for Neural Networks and 5.92 for KNN. The precisions in different validation configurations appear as alternating due to the different sorting of the samples before each validation begins. Both of the algorithms show good performance of our method. Naïve Bayes on the other hand handles it poorly because of the high error rate shown in the column MASE, which shows the low performance of dealing with regression tasks. Steps with regression tasks are responsible for peaks scan in our method, and any lack of scanning enough peaks will eventually affect also the performance of classification tasks that rely on peaks parameters, even though Naïve Bayes is good at dealing with classification tasks. Configuring Naïve Bayes in scanning more peaks will overcome this deficiency with the cost of increasing running time. However, its affectability is negligible since the algorithm is extremely fast which takes less than 1 second in both the validation configurations and the testing results as is evident in Table II-3 and Table II-4. Alternatively, KNN and Neural Networks perform slowly with a rate of 390 times, and 7876 times slower than Naïve Bayes respectively according to 10-fold cross-validation running time in Table II-3. Principal Component Analysis (PCA) results in Figure II-18 show that the extracted features are dependent on each other and need more improvements and selections as is in the case of the steps "R-peaks scan", "Beat peaks scan", "P and T peaks selection", "Slurred upstrokes scan",

and “Delta examination”. Likewise, the Eigenvectors listed in Table II-5 which correspond to the statistical parameters (mean, min, max, STD_DEV, and IQR) show the ineffectiveness of the parameters “min” and “max” since these parameters are extracted from the normalized signal. These statistical parameters are implemented as features in four steps (R-peaks scan, beat peaks scan, slurred upstrokes scan, and Delta examination). Eliminating the dependency and redundancy of the features in these steps will lower the cost of running time.

The validation configurations of the highest accuracy of the three model types in Table II-1 show that Neural Networks and KNN gave their best performance in holdout cross-validation. Naïve Bayes performed well in 3-fold cross-validation. A zoom into the results of these configurations is represented in Table II-2. It includes the evaluation of the seven steps of the selected configuration since each step performs with a machine learning model of the same chosen model type (Neural Networks, Naïve Bayes, or KNN). Both Neural Networks and KNN performed well on the regression task of “R-peaks scan” and the classification tasks “false positive R removal” and “Short PR scan” with a MASE below 1 and a precision higher than 98 in accuracy, sensitivity, and specificity. For the “Upstroke scan”, KNN got a little higher error rate with a MASE of 1.13 while Neural Networks kept it below 1. The challenge occurs in the “Beat peaks scan” where MASE is much higher than 1 and affected the number of the peaks to be classified, which eventually lowers the sensitivity of “P and T peaks selection”. The same difficulty affects severely on Naïve Bayes because of the low resolution of its outputs of the regression tasks. Hence, the detection of P and T peaks is low, which clarifies the low accuracy of the “Short PR scan” since the existence of the P peak is critical in examining the PR interval. Also, Naïve Bayes is sensitive to imbalanced data and that furthermore explains its low sensitivity in “false positive R removal” compared to Neural Networks and KNN. The evaluation of the step “Delta examination” shows a good performance of the three types of models with 100% in both accuracy and sensitivity. The 0% in specificity is due to the inexistence of Lown-Ganon-Levine (LGL) syndrome samples in the dataset.

The reflection of the data in Table II-2 is illustrated in the results of the test dataset in Figure II-16 and Figure II-17 where the scan and selection of QRS peaks of the four samples (112m (1), 113m (3), 230m (0), 230m (1)) are well extracted either in intra-patient or inter-patient evaluation paradigm using the three types of models even though the MASE of Naïve Bayes in “R-peaks scan” is much higher with a value of 2.94. Except for the result of the test (c) in Figure II-16 and Figure II-17, the label of Q peak is shifted to the left due to the high error rate of “Beat peaks scan” with a value of 11.13, which yields the absence of P and T peaks in (c), (d), (i), and (j) of Naïve Bayes performance. This affectation is present in some beats of Neural Networks and KNN performance. The existence and position of P and Q peaks are critical in checking the

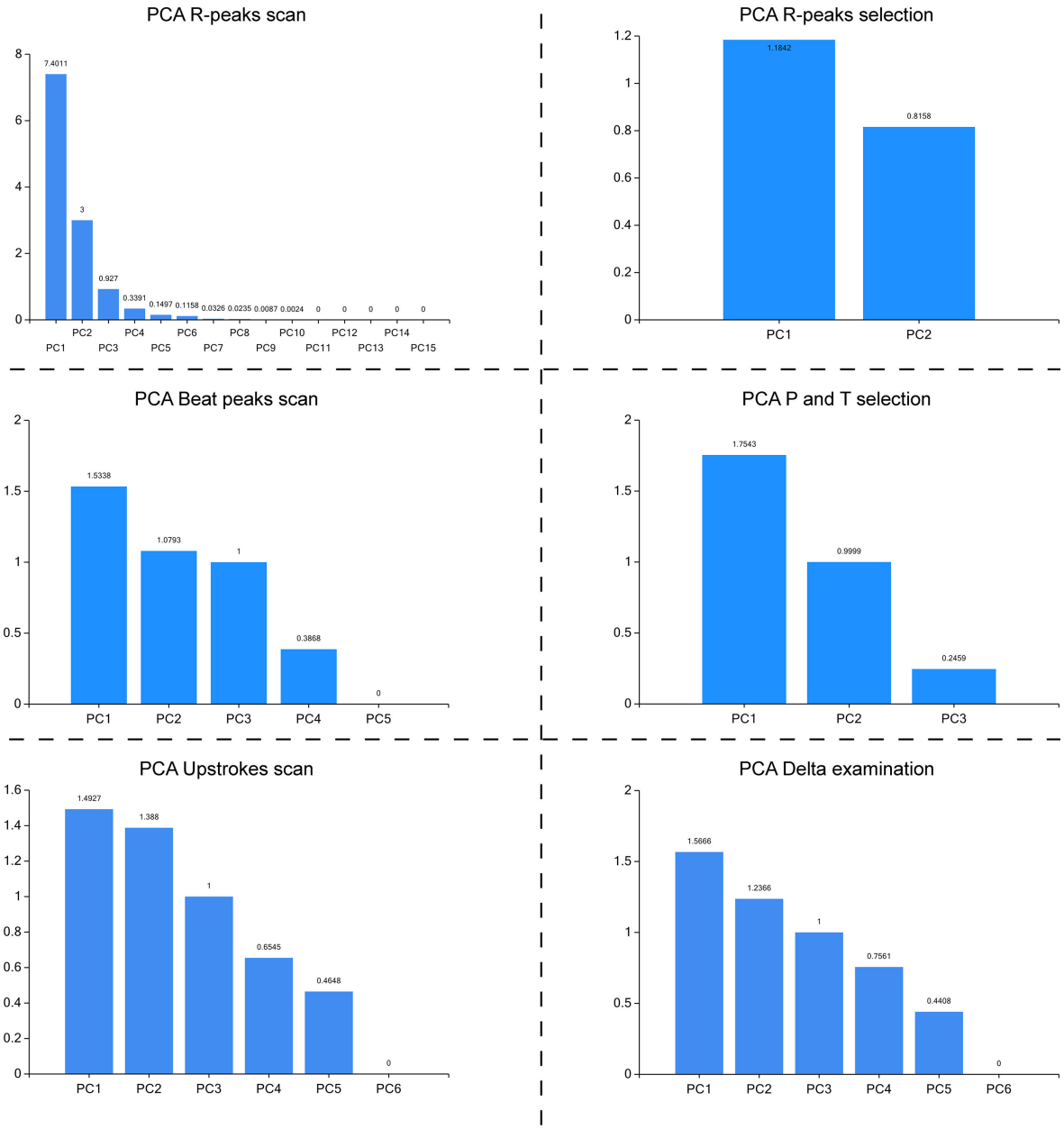

Figure II-18: PCA results of the datasets of the steps containing more than one feature.

Table II-6: Performance comparison of four different studies in the detection of characteristic waves in ECG signal.

					Waves detection metric values			
Study	**Database**	**Subjects count**	**Beats count**	**Metrics**	**P (%)**	**R (%)**	**T (%)**	**Delta (%)**
Proposed method	MIT Arrhythmia	17	1368	Ac (%)	**98.71**	**99.44**	**98.71**	**100**
				Se (%)	88.63	**99.42**	88.63	**100**
				Sp (%)	**99.32**	**100**	**99.32**	**0**
Mahamat et al. [200]	PTBDB	-	-	Ac (%)	94	97	94	-
				Se (%)	-	-	-	-
				Sp (%)	-	-	-	-
Li et al. [199]	MIT Arrhythmia	4	4398	Ac (%)	97.40	97.40	97.30	-
				Se (%)	**98.68**	98.68	**98.64**	-
				PP (%)	98.68	98.68	98.64	-
Maršánová et al. [195]	MIT Arrhythmia	12	22108	Ac (%)	-	94.35	-	-
				Se (%)	97.41	91.20	-	-
				Sp (%)	-	93.60	-	-
				PP (%)	92.91	-		-

abnormality of the PR interval. The inaccuracy of positioning P and Q peaks leads to miss-annotating beats with WPW pattern as is in the case of some beats in (g), (h), (k), and (l) in Figure II-16; and in (k) in Figure II-17. The last beat in (g) and (h) in Figure II-16, and the last part of (k) in Figure II-17 are odd miss-annotated beats with WPW pattern; P and Q peaks seem well positioned whereas the Delta wave is not stated as a consequence of inaccuracy of "Upstroke scan" step, besides the Q peak is a bit lifted up, which might cause miss-calculations in tangent deviation scan. The test results of the samples (112m (1), 113m (3)) of the inter-patient evaluation paradigm in Figure II-17 prove the effectiveness of the proposed method. However, due to the lack of ECG signals of different pathologies in the training dataset, the location of S and T peaks in the sample "s0351lre_V6" is not well selected.

To better evaluate the proposed method, a performance comparison is conducted and arranged in Table II-6. The comparison lists the evaluations of four different studies including the proposed method in the detection of the characteristic waves in ECG signals. It also considers the detail of the implemented database of each study for clarifying the diversity of the evaluation. Different metrics are also included denoting what each study has implemented. The metrics are abbreviated as "Ac", "Se", "Sp", and "PP", which stand for Accuracy, Sensitivity, Specificity, and Positive predictivity respectively. Any non-reported value is replaced with "-". Positive predictivity isn't applied as an evaluation metric in this study, and its value can be obtained as follows:

$$PP = \frac{TP}{TP + FP} \tag{II-13}$$

where TP is True Positive, FP is False Positive, and FN is False Negative.

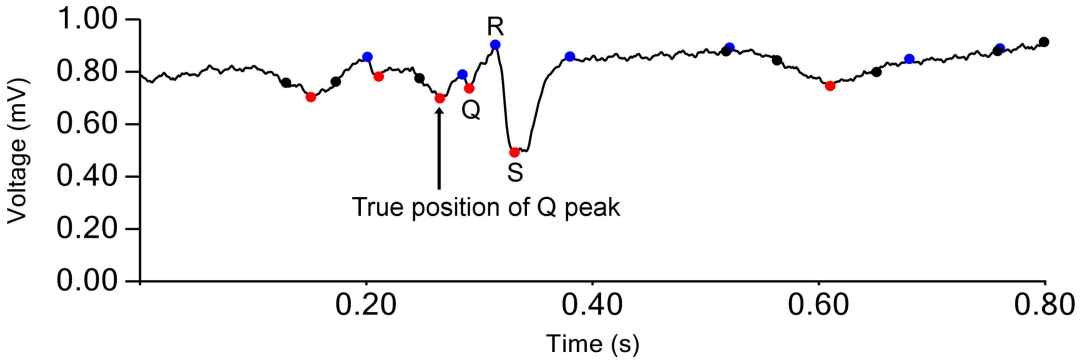

Figure II-19: False positioning of Q peak in a noisy ECG signal (signal s0351lre_aVL from PTB Diagnostic ECG DB scanned with HT: 0.016 sec, ART: 0.093%).

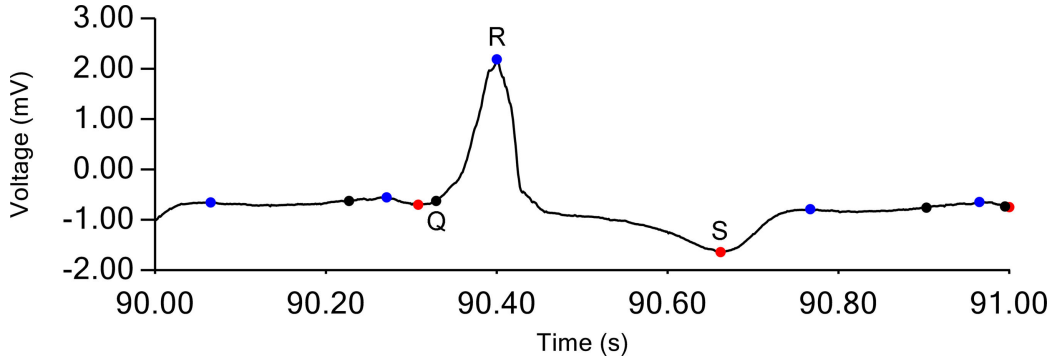

Figure II-20: Poor S peak scan in a beat signal with slowly declining negative T (signal s0351lre_V5 from PTB Diagnostic ECG DB scanned with HT: 0.016 sec, ART: 0.017%).

As stated in Table II-6, it is evident that the proposed method outperformed the other mentioned methods in accuracy in the detection of P, R, and T peaks, even with a more diverse dataset (17 different patients) and fewer beats count. However, precision in sensitivity is low in the detection of P and T peaks as a consequence of not relying on predefined windows for narrowing the scanning time interval. Even though, these predefined windows are also dependent on the position of the R peak, which will cause a completely random selection of P peaks in the case of "2nd degree atrioventricular block Mobitz type I". The values of R peaks detection of the proposed study are taken from the evaluation of the step "false positive R removal". Since the proposed method is very sensitive in R peaks detection, the specificity of "false positive R removal" is taken as sensitivity in "R peaks detection" and vice versa with a sensitivity of "false positive R removal". Almost the same case is applied to the study of Maršánová et al. [195] where the evaluation of R peaks detection is considered from the evaluation of classifying beats between "Premature ventricular complex" and other types of beats. Also, from the listed values of the detection of R peaks in Table II-6, it is clear that the proposed method outperformed the three mentioned studies in accuracy and sensitivity.

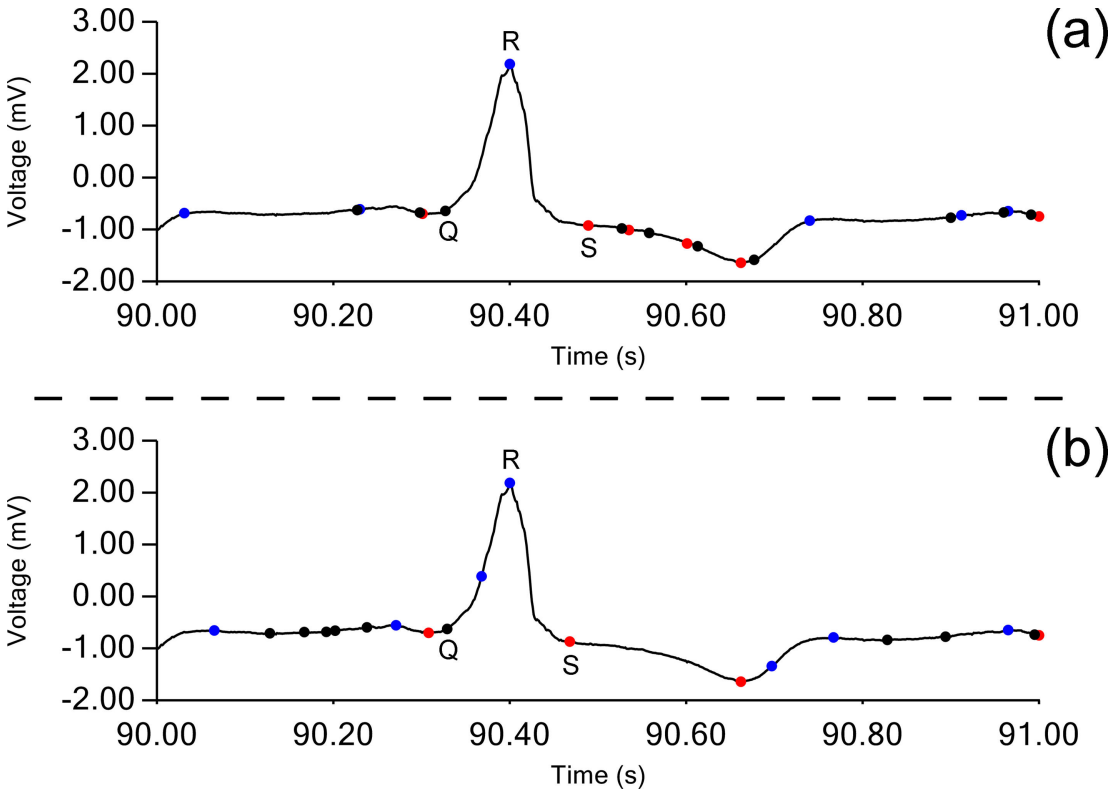

Figure II-21: Two proposed solutions to the deficiency of poor S peak scan: (a) shortening HT as with (HT: 0.004 sec, ART: 0.017%); (b) activating tangent deviation scan as with (HT: 0.016 sec, ART: 0.017%, TDT: 0.5%).

Furthermore, though Mahamat et al. [200] proposed a method for annotating beats containing the Delta wave and not precisely locating the Delta wave, no published studies were found that have performed in accurately locating the Delta wave of the Wolff-Parkinson-White pattern.

II.7. Conclusion

In this chapter, a new method is proposed and examined for ECG signals classification in the case of WPW pattern detection using a developed algorithm named “Peak analyzer” that operates almost like the human vision analysis for locating the dominant curving points in the signal. Also, the robustness of the proposed method is the outcome of the cooperation of machine learning algorithms (Neural Networks, Naïve Bayes, and K-Nearest Neighbors) helping with tuning the proposed “Peak analyzer” for each signal rather than relying on predefined fixed size windows as is mentioned in the literature [195], [199], [200]. The method is serialized in seven steps, where it identifies P, Q, R, S, and T peaks using a function dedicated to peaks scan, in addition to the detection and examination of the slurred upstroke named Delta wave using a function for tangent deviation scan for accurately locating Delta wave, instead of relating its diagnosis with the time interval and the absolute maximum amplitude of QRS

complex as is applied in the literature [200], which might conduct to false positive or false negative diagnosis if the concerned beat is pathological in complete bundle branch block or ventricular hypertrophy respectively [201], [202].

The performance of the three types of models using our proposed method is validated in different cross-validation configurations on 122 signals from the MIT Arrhythmia database. The highest precision obtained in Neural Networks and KNN is reflected in holdout cross-validation with mean accuracy, sensitivity, specificity, and MASE of the seven steps of 99.25%, 97.16%, 74.37%, 2.33 respectively from Neural Networks performance, and 99.11%, 94.64%, 74.37%, 1.26 respectively from KNN performance. Naïve Bayes obtained the same evaluation metrics results in 3-fold cross-validation with 81.23%, 46.91%, 57.84%, and 5.63 respectively.

Even though Neural Networks and KNN perform well using our proposed method, the selected features need more refinement for improving the detection of P, Q, S, and T peaks in addition to reducing running time. Naïve Bayes also needs improvement in dealing with regression tasks. Furthermore, the proposed method selects Q and S peaks naively from the position of R, which might lead to miss-locating their true positions in noisy signals as is illustrated in Figure II-19 and Figure II-20. Even though, the deficiency of miss-locating S peak can be contained with shortening the value of HT, or activating tangent deviation scan as is illustrated in Figure II-21. The pathology "2nd degree atrioventricular block Mobitz type I" where the rhythm of P waves is completely independent of the rhythm of R waves will also affect the performance of the proposed method in the detection of P peaks, since the detection of P peaks in the proposed method relies on the detection of R peaks.

Chapter III. LSTM and RL based peak analyzer for ECG characteristic waves delineation

III.1. Introduction

Most biological organs in a living body rely entirely on the heart's delivery of oxygens and nutrients to sustain healthy functions [218]. The heart maintains this operation by continuously pumping blood through the circulatory system. Consequently, disruptions to its activity eventually affect the whole body and may lead to permanent death caused by cardiac arrest. While the heart is mostly a victim of cardiac arrest which originates within the coronary arteries and is related to hypertension [219] and body mass index (BMI) [220], it is also a source of vulnerabilities due to mal-functionalities that could be congenital [221], [222] or acquired [223] such as arrhythmias and structural complications. Both deficiencies could be recorded from the electrical activity of the heart using an electrocardiogram (ECG). With the help of electrodes attached non-invasively to the skin surface, the ECG signal is considered one of the first options in the diagnosis of heart-related defects. The normal sinus rhythm (NSR) of the ECG signal consists of well-known characteristic waves (CW) named P, QRS, and T waves. The fiducial points (onset, peak, and end) of these characteristic waves carry the major information on the waveforms of the ECG signal. However, the continuous periodic repetition of the waveforms with the intermittent arrhythmias [224] makes the analysis of the signal a strenuous and time-consuming activity for a human being such as a doctor. Thus, the design of an autonomous system handling the redundant activity of the ECG signal analysis would save time for the experts while keeping high attention on the surveillance of the patients.

The standard ECG recording contains 12 leads (signals) recorded from the biopotential measurements using 10 electrodes placed on the skin [225], [226]. However, the advance of technology nowadays is pushing towards the utilization of small and portable devices with less skin contact [227]. Thus, pushing towards more quantitative and system design optimization. Such requirements assist with the elimination of redundant data and introduce the challenge of processing noisy and maybe limited data.

According to the related works introduced below, most of the ECG signal delineation methods are dependent on the sampling frequency of the input signal, pre-segmented CW; limited to defined windows; and susceptible to distortions such as signal soothing and phase distortion due to the applied filters. This chapter introduces a novel method containing the

aforementioned issues in the previous related works for the delineation of the fiducial points of the ECG characteristic waves (CW). The proposed method utilizes a novel peak analyzer algorithm manipulated using a reinforcement learning (RL) [228], [229] model for delineating the prominent peaks of the ECG signal as a compression step and for the selection of the samples to be fed sequentially to the LSTM classifier. The peak analyzer supports the method with its independence from the sampling frequency of the input signal and rather relies on the features extraction method and the LSTM memory property.

The rest of the chapter is organized as follows. Section III-2 introduces the heuristic- and neural network-based approaches proposed in the literature. The method is then thoroughly described in Section III-3 covering the steps involved in the proposed method, the algorithm of the peak analyzer, a signal segmentation method for speeding up the peak analyzer's step and enhancing its accuracy, the design of the reinforcement learning and the LSTM models, and the features extraction method for the LSTM model. The description of the implemented dataset with the required preprocessing is included in Section III-4 as well as the delineation results. Section III-5 covers the discussion of the obtained results in addition to classification and running time comparison with the state of the art. The issues addressed in our previous work [230] are also discussed in Section III-5 and Section III-6 concludes this work with new limitations and perspectives addressed.

III.2. Related works

Multiple methods are proposed in the literature for the delineation of the fiducial points of the ECG characteristic waves using the single and the 12-lead ECG signals. Li et al. [199] proposed a heuristic three-stage method for the detection of the fiducial points of a single lead ECG signal based on the wavelet transform (WT) decomposition and obtained good results around 98.48%-98.68% and 98.48%-98.68% in sensitivity and positive predictive value (PPV) respectively on the QT-dataset (QTDB). Spicher and Kukuk [231] also proposed a different heuristic method based on the extraction of the fiducial points from an estimated model generated and designed from a modified Gaussian function model to simulate the ECG characteristic waves. They improved their model at a step named exhaustive search by applying domain-specific knowledge (defining limits of possible peaks according to real ECG signals) [232] and obtained results with high sensitivity ranging from 99.89% to 99.93 in the detection of the fiducial points using the QTDB.

On the other hand, for the neural network-based methods, Krasteva et al. [233] presented a neural networks model with a convolutional encoder-decoder architecture named "CED-Net" for a binary segmentation of the P wave, QRS complex, and the QT interval of 12-lead

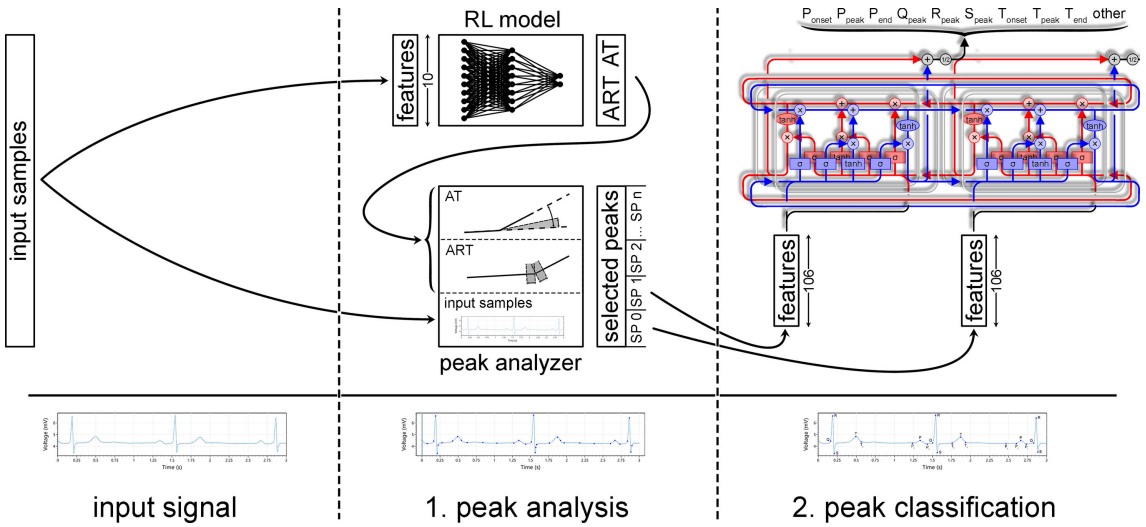

Figure III-1: General steps of the proposed method for the delineation of the electrocardiogram characteristic waves.

representative beats. They tested their model on the PTB-diagnostic dataset with its ground truth generated from separate commercial software named ETM-2.6.5 and obtained a PPV and a negative predictive value (NPV) of 95.6% and 97.4% respectively. Li et al. [234] designed another U-Net encoder-decoder model with a transformer block in between for the binary segmentation of the P, QRS, T, and other waves on single-lead records. Their method alternatively does not rely on separate software for the generation of representative beats but rather divides the entire record into 4.8-sec. They validated their model on the QTDB and obtained highly precise results with sensitivity and PPVs ranging from 97.28% to 99.81% and from 96.60% to 99.82% respectively. Peimankar and Puthusserypady [235] proposed a decoder model that expands each input sample to 128 feature samples fed to an LSTM model for sample classification to P, QRS, T, or no wave. They validated their model on the QTDB and obtained good results in sensitivity and PPV ranging from 95.49% to 99.75% and from 88.77% to 96.51% respectively. Alternatively, Nurmaini et al. [236] implemented an LSTM model for classifying the samples of an entire beat at once by estimating the durations of the P wave, PR segment, QRS complex, ST segment, and T wave. They also validated their method on the QTDB and obtained high values in sensitivity and PPV ranging from 98.38% to 99.10% and from 97.92% to 99.24% respectively.

III.3. Method description

The proposed method for delineating and classifying the fiducial points of the ECG signal relies fundamentally on the detection of the prominent points of the signal using a novel peak

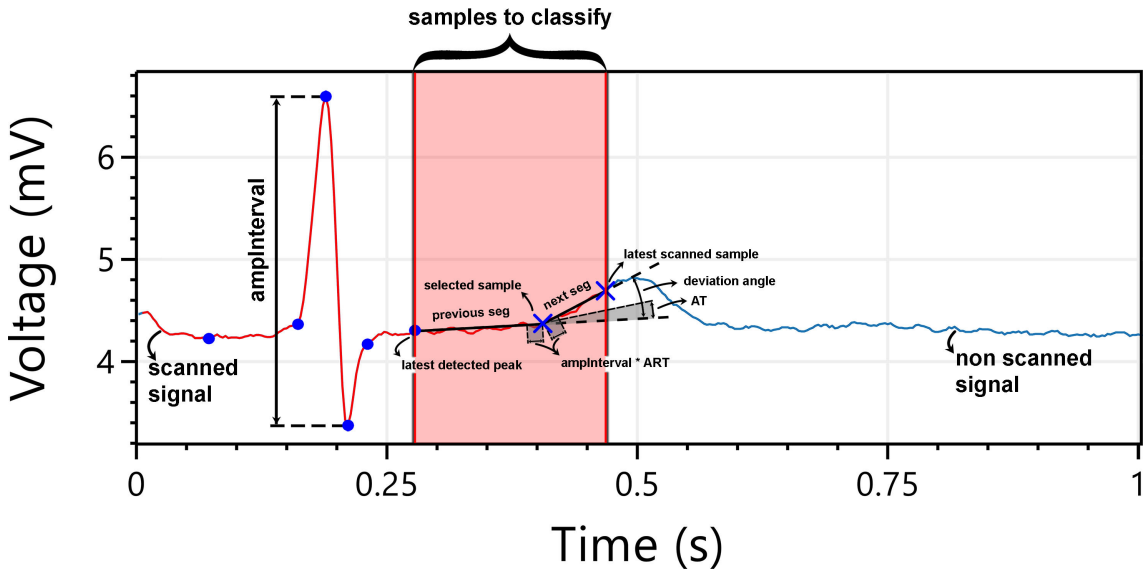

Figure III-2: Elements of the peak analyzer.

analyzer for scanning the peak and deviations of the signal as highlighted points to be classified sequentially using the long short-term memory neural network (LSTM) model. The method consists of two steps (peak analysis, and peak classification) as outlined in the graphical abstract in Figure III-1.

III.3.1. Peak analysis

The first step of the method selects the prominent peaks from the input signal and discards nonessential samples. Achieving such task is possible using reinforcement learning for automatically tuning the peak analyzer additional to signal segmentation for improving the accuracy and speed of the task.

III.3.1.1. Peak analyzer

The proposed novel method for the detection of the prominent peak and deviations of a 1-D signal in this work is an improvement to the proposed method in our previous work (Section II-4.1) [230] which considers three parameters (amplitude ratio threshold, horizontal time threshold, and tangent deviation threshold) for examining the amplitude of the sample, its time interval from the previous detected peak, and its tangent deviation from the mean tangent. The current proposed method considers two parameters instead (amplitude ratio threshold, and angle threshold) for examining the magnitude of the segments between the selected sample and its surrounding samples, and the deviation angle between the segments. Each sample from the signal is associated with two segments (previous and next segment) as depicted in Figure III-2. The previous segment is computed once and covers the interval from the latest detected peak to

Algorithm III-1: Pseudo code of the signal peak analyzer.

```
Input: samplesArray, sFreq, ART, AT.
Output: PeaksArray.
1:      latestPeak = samplesArray[0]
2:      ampInterval = Interval(samplesArray)
3:      for i = 1 to len(samplesArray) do
4:        sam1 = samplesArray[i]
5:        if i - latestPeak.index > 0 do
6:          (sam1.prevMag, sam1.prevTan) = MagTan(latestPeak, sam1, sFreq)
7:        end if
8:        if i - latestPeak.index > 1 do
9:          for j = latestPeak.index + 1 to i do
10:           sam2 = samplesArray[j]
11:           (sam2.nextMag, sam2.nextTan) = MagTan(sam2, sam1, sFreq)
12:           sam2.devAngle = Angle(sam2.nextTan, sam2.prevTan)
13:         end for j
14:         selSams = samplesArray.Where
            (
            latestPeak.index < sam.index and
            sam.index < i and
            sam.nextMag > ampInterval * ART and
            sam.prevMag > ampInterval * ART and
            sam.devAngle > AT
            )
15:         if len(selSams) > 0 do
16            newPeak = selSams.Max(sam.nextMag + sam.prevMag)
17:           PeaksArray.Add(newPeak)
18:           latestPeak = newPeak
19:           for j = latestPeak.index + 1 to i do
20:             sam3 = latestPeak
21:             sam2 = samplesArray[j]
22:             (sam2.prevMag, sam2.prevTan) = MagTan(sam3, sam2, sFreq)
23:           end for j
24:       end if
25:     end if
26:   end for i
```

the selected sample while the next segment is computed and updated after each iteration in scanning new samples and it covers the interval from the selected sample to the latest scanned sample. If the magnitude and deviation angle of the segments of a sample meet the conditions of creating a new peak, then the previous segments of the next samples (between the new peak and the latest scanned sample) which were computed according to the previous peak are updated according to the new peak. The computation of the method is based on calculating the magnitude (mag), tangent (tan), and deviation angle of two segments from three samples which are defined as follows:

$$adj(x_1, x_2) = \frac{x_2 - x_1}{S_{freq}} \tag{III-1}$$

$$opp(x_1, x_2) = y_2 - y_1 \tag{III-2}$$

$$mag(x_1, x_2) = \sqrt{[adj(x_1, x_2)]^2 + [opp(x_1, x_2)]^2} \quad \text{(III-3)}$$

$$tan(x_1, x_2) = \frac{opp(x_1, x_2)}{adj(x_1, x_2)} \quad \text{(III-4)}$$

$$angle(tan(x_2, x_3), tan(x_1, x_2)) = arctan(tan(x_2, x_3)) - arctan(tan(x_1, x_2)) \quad \text{(III-5)}$$

where x1, x2, and x3 are the position indexes of the latest detected peak, selected sample, and latest scanned sample respectively as illustrated in Figure III-2, y_1 and y_2 represent the amplitude values corresponding to x_1 and x_2 respectively, S_{freq} is the sampling frequency of the signal. The method is summarized in Algorithm III-1.

The pseudo-code in Algorithm III-1 takes four arguments as input (the samples array of the signal, its sampling frequency, the amplitude ratio threshold (ART), and the angle threshold (AT)) and outputs the positions of the detected peaks where ART represents a ratio value between 0 and 1, and AT is an angle value from 0° to 360°. The algorithm also implements seven additional functions (Interval, len, MagTan, Angle, Where, Max, and Add) where "Interval" computes the amplitude interval of the signal ($max_{value} - min_{value}$), "len" returns the number of elements in an array, "MagTan" computes the magnitude and tangent of a segment between two samples using the equation (III-3) and (III-4), "Angle" calculates the angle between two tangents using the equation (III-5), "Where" generates an array of items from the original array that correlate with the conditions given in parenthesis, "Max" generates an array from the original array using the expression given as argument in parenthesis and returns the element from the original array that corresponds to the greatest value in the generated array, and "Add" appends the value given as argument in parenthesis to the list it was called from. The conditions in line 14 in Algorithm III-1 determine the samples that could be classified as the next peak which should be after the latest peak and before the latest scanned sample as indicated under the highlighted portion of the signal in Figure III-2, and the magnitude and deviation angle between their next and previous segments should satisfy ART and AT conditions respectively. The amplitude interval of the signal is used with the ART condition as an approach of normalization since the magnitude of the segments doesn't have specific bounded interval. The selected samples in line 14 are then compared in line 16 to get the sample with the longest accumulated magnitude of its previous and next segments making it at the highest end on both sides as illustrated in Figure III-3.

III.3.1.2. Signal segmentation

The method in Algorithm III-1 is not efficient in terms of running time since it lunches many repetitive loops in addition to the dependency of the magnitudes condition in line 14 to

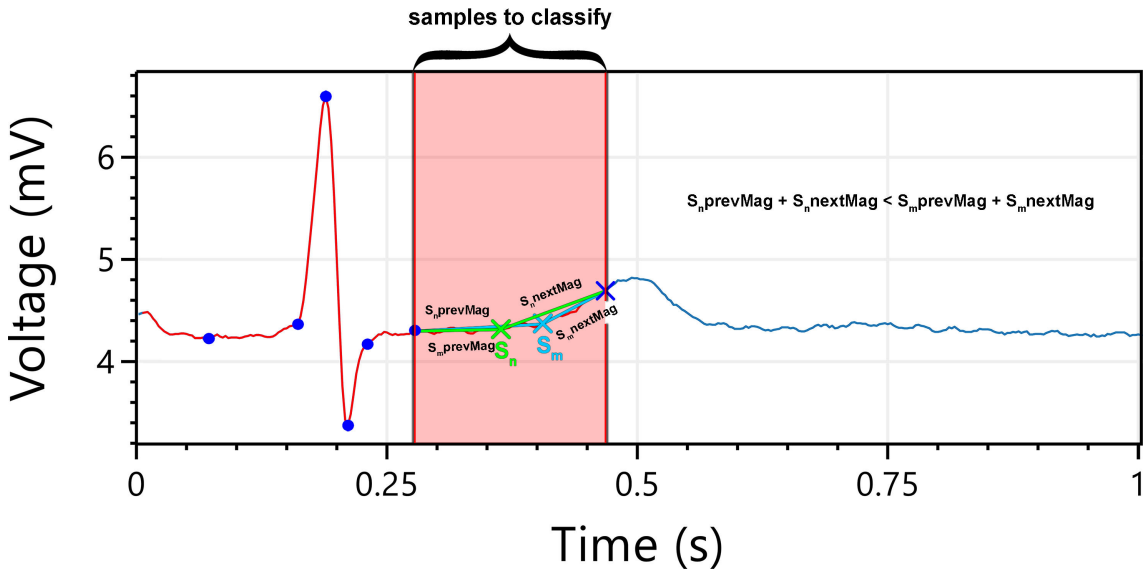

Figure III-3: Comparison of the accumulated magnitude of the previous and next segments of the selected samples to classify as a new peak.

the amplitude interval of the global signal which sometimes misses detecting small segments such as the PR segment (from P_{end} to QRS_{onset}). Therefore, a signal segmentation method is proposed for creating a list of signal segments of short length while maintaining the distribution of the samples' amplitudes of the segments almost equiprobable. The conditions defined by experiments for this purpose ensure the length of the segment to be no less than 0.2 seconds and no more than 1 second, and the amplitude probability distribution values to be less than 0.5 (50%). The amplitude interval of the signal is discretized to 10 equiprobable intervals and thus yields 10 distribution values. A probability value reaching 50% while scanning new samples refers to the beginning of a new segment from the signal as shown in (b) in Figure III-4. However, the distribution of ECG signal samples is susceptible to low-frequency noise which might impact outlining the beginning of new segments (covering the low amplitude T and P waves with the high amplitude QRS complex in one segment) such as the example depicted in Figure III-5 (a). Thus, the signal segmentation is extrapolated from segmenting the absolute values of the first level of the discrete wavelet transform (DWT) using the "Haar" mother wavelet which eliminates the noisy low frequencies and keeps the high frequencies of the QRS complexes (Figure III-5 (b)). The segments bounded using the distribution method are then extended for up to 0.1 seconds at both sides in case the extension keeps the segment amplitude interval within its first amplitude boundaries as illustrated in Figure III-6. This extension facilitates to the peak analyzer the detection of any peaks located at the edges of the signal segments.

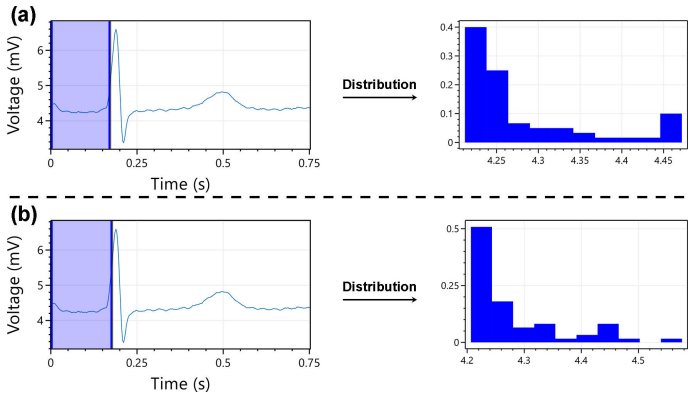

Figure III-4: Extraction of the distribution of the samples' amplitudes in two highlighted areas: (a) all probability values being lower than 0.5 indicating the association of the segments in the same segment; (b) the first probability value exceeding 0.5 signifying the beginning of a new segment.

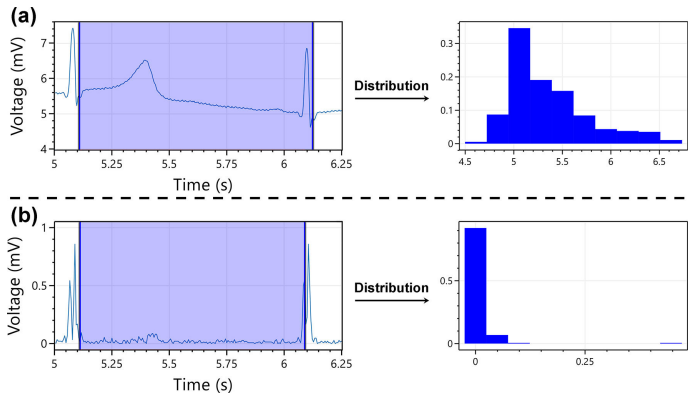

Figure III-5: Suppression of the effect of low noise in the distribution using DWT: (a) low noise keeping the distribution values of the highlighted area lower than 0.5 even after exceeding the beginning of the next segment; (b) the elimination of low noise using DWT allowing the distribution indicating the segmentation boundaries.

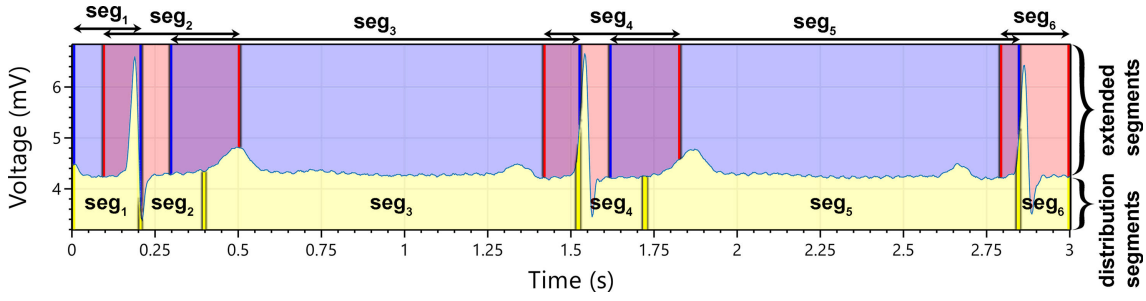

Figure III-6: Extension of the boundaries of the distribution segments (the yellow segments delineated below the signal) to overlapped extended segments (the blue and red segments above the signal).

Table III-1: Architecture of the proposed models.

Method	Batch size	Epoch	Early stopping	Loss function	Optimizer	Seq length	Architecture		
							Input	Output	Activation
RL model	4	1000	activated	MSE	SGD	-	10	8	ELU
							8	2	linear
Bi-LSTM model	4	200	activated	MSE	SGD	2	106	10	linear

III.3.1.3. Reinforcement learning for autonomous peak analysis

The peak analyzer detects the prominent peaks according to the amplitude ratio threshold (ART), and the angle threshold (AT) which affect its sensitivity to peak detection related to the signal being scanned. However, the segments of the signals differ in amplitude, rhythm, noise, and morphology. Therefore, each segment requires tuned ART and AT parameters for the prominent peaks analysis. Achieving this when dealing with big-data is possible using reinforcement learning where an agent is placed in an environment (signal segment) having two dimensions to move on (ART and AT), and two functions for computing the reward of the states and determining the end of the episodes. The proposed method implements deep reinforcement learning with two artificial neural networks (ANN) models (a temporal model for the training phase only and the final model). As sorted in Table III-1, both models have the same architecture with 10 neurons input layer, 8 neurons "ELU" activated hidden layer, and 2 neurons linear output layer. The mean squared error (MSE) and stochastic gradient descent (SGD) were chosen as the cost and optimizer functions respectively. The signal segment samples are converted to 10 probability distribution values as a features extraction approach and fed to the input of the ANN model. The output is then ART and AT values normalized. The generation of the training dataset to the final model is managed with the reinforcement learning mechanism where the agent is given the signal segment and expected to find the best state of ART and AT that corresponds to the highest reward. The continuous values of the ART and AT are discretized to 60 and 30 states respectively covering the interval 0-0.3 and 1°-25° which frame the step of the agent to 0.005 and 0.8° respectively. The chosen interval and step values favor the agent to focus more on high sensitivity to prominent peaks. The agent has then 4 actions to move through the states of the two dimensions ART and AT using the value function for computing the reward and updating the Q-table. The reward is computed with respect to two parameters (tolerance of the fiducial points (Tol) and the detected peak over the fiducial points ratio threshold (PFRT)) and is distributed as follows:

- –1 as movement penalty.
- +1 if a peak is within the Tol of a fiducial point.
- –1 if a peak is not within any Tol of a fiducial point or is a duplicate peak within the Tol of a detected fiducial point.
- –5 if a fiducial point is not detected.

- +5 if all fiducial points are detected and if *detected_peaks_count / fiducial_points_count* < *PFRT*.

At first, exploring each signal segment, the Q-table of the environment is reset. The agent is then given 3 episodes for exploring the environment. Three episodes are chosen as a generalization approach for the ANN model since only the final state matters to the model and not the full trajectory of the agent. The starting state of the agent at each episode is predicted using the temporal model while the state at the end of the episode is used for training the model if the predicted starting state is far from the final state according to a chosen threshold for avoiding overfitting the temporal model. The agent is also given a random state if it is stuck between two states and does not reach a final state. The final state of the episode is identified as finding all fiducial points of the signal segment and *detected_peaks_count / fiducial_points_count* < *PFRT*. However, the PFRT is incremented by 0.5 and up to 80 increments after every 50 steps if the agent does not reach the final state of an episode. Finally, the state with the highest reward of the three episodes is then selected for the final model's training dataset. The final model is then trained with the generated dataset at once with a batch size of four.

III.3.2. Peak classification

Though the detected peaks are not equally distanced, their sequential property could use the advantage of storing or removing information using the long short-term memory (LSTM) neural network architecture for the classification step. Table III-1 summarizes the design of the proposed model which contains one layer of two bidirectional-LSTM cells with 106 input features and 10 output labels. The output labels represent P_{onset}, P_{peak}, P_{end}, Q_{peak}/QRS_{onset}, R_{peak}/QRS_{peak}, S_{peak}/QRS_{end}, T_{onset}, T_{peak}, T_{end}, and Other. The input peak features are selected to hold information related to its surrounding samples in a range of 1 second, the ECG characteristic waves (P, QRS, and T waves) rhythms, the signal segment's amplitude interval, and the global signal's amplitude interval. These features assist the LSTM model in identifying the fiducial points locally and globally (related to local and global samples as illustrated in Figure III-7 and Figure III-8 respectively). The first 100 features are extracted from the surrounding 1-second time span, a 0.5-second following and a 0.5-second preceding time span where each span is divided into 5 intervals of 0.1 seconds. The intervals are used for creating combinations of two sub-spans, a long sub-span and a short sub-span where the long sub-span could take 2-5 intervals and the short sub-span should not reach or exceed the long sub-span making the following 10 combinations {2, 1}; {3, 1}; {3, 2}; {4, 1}; {4, 2}; {4, 3}; {5, 1}; {5, 2}; {5, 3}; {5, 4} of long and short sub-spans respectively. Each combination is used for computing 5 features from the following span as well as the same 5 features from the preceding

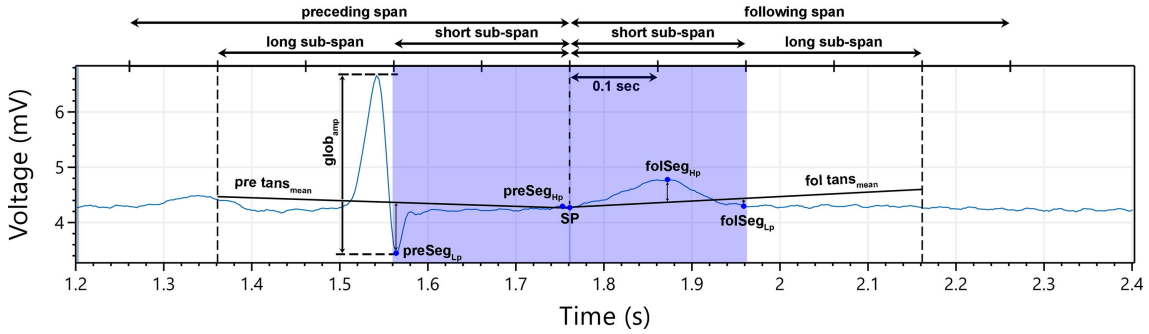

Figure III-7: Elements for extracting the features of the signal morphology using the combination {4, 2} of the long and short sub-spans respectively for the LSTM classification model where SP refers to selected peak, "pre" to preceding, "fol" to following, "seg" to segment, "Lp" to lowest point, "Hp" to highest point, "glob" to global, and "amp" to amplitude.

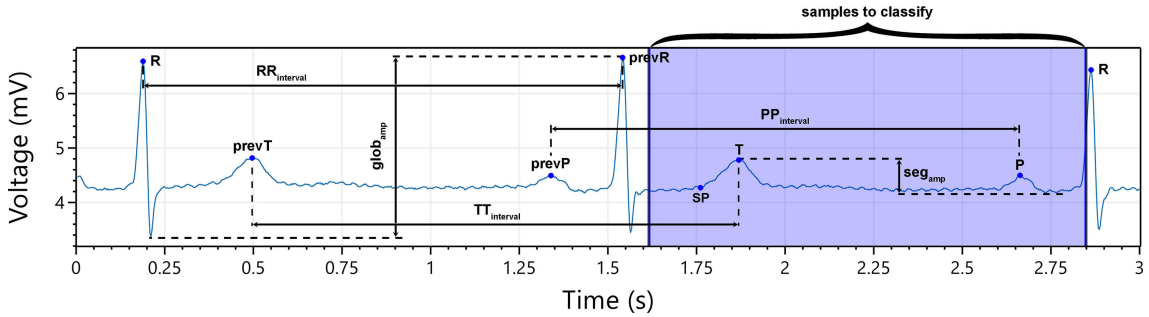

Figure III-8: Elements for extracting the features of the characteristic waves' rhythm for the LSTM classification model where SP refers to selected peak, "prev" to previous, "glob" to global, and "seg" to segment.

span making 10 features for each combination. Illustrated in Figure III-7, these features are based on computing the tangents mean ($tans_{mean}$) of the long sub-span segment and finding the position of the highest and lowest points away from the $tans_{mean}$ in the short sub-span segment (x_{segHp} and x_{segLp} respectively). Therefore, using the equation (III-4), the $tans_{mean}$, x_{segHp} and x_{segLp} are computed as follows:

$$tans_{mean} = \frac{1}{N}\sum_{i=1}^{N} tan(x_0, x_i) \tag{III-6}$$

$$x_{seg_{Hp}} = \underset{1\le i<M}{argmax}\left[y_i - \left(y_0 + tans_{mean}\frac{i}{S_{freq}}\right)\right] \tag{III-7}$$

$$x_{seg_{Lp}} = \underset{1\le i<M}{argmin}\left[y_i - \left(y_0 + tans_{mean}\frac{i}{S_{freq}}\right)\right] \tag{III-8}$$

where x_{SP} and y_{SP} are the position index and amplitude of the selected peak respectively, x_i and y_i are the position index and amplitude of the i^{th} sample from the sub-span segment respectively, N and M are the length of long and short sub-spans respectively, S_{freq} is the sampling frequency

of the signal, and argmax and argmin return the position index of the max and the min of the interval values between the square brackets respectively. The function ($y_0 + tans_{mean}\ i\ /\ S_{freq}$) represents the $tans_{mean}$ line and its subtraction from y_i yields the difference in amplitude from the $tans_{mean}$. Accordingly, the LSTM features are then obtained as follows:

$$comb_{feat1} = \frac{angle(tan(x_0, x_{seg_{Hp}}), tans_{mean})}{180} \tag{III-9}$$

$$comb_{feat2} = \frac{angle(tan(x_0, x_{seg_{Lp}}), tans_{mean})}{180} \tag{III-10}$$

$$comb_{feat3} = \frac{y_{seg_{Hp}} - y_{seg_{Lp}}}{glob_{amp}} \tag{III-11}$$

$$comb_{feat4} = \frac{mag(x_0, x_{seg_{Hp}})}{glob_{amp}} \tag{III-12}$$

$$comb_{feat5} = \frac{mag(x_0, x_{seg_{Lp}})}{glob_{amp}} \tag{III-13}$$

$$feat101 = \frac{x_{peak} - x_{prevP}}{PP_{av}} \tag{III-14}$$

$$feat102 = \frac{x_{peak} - x_{prevR}}{RR_{av}} \tag{III-15}$$

$$feat103 = \frac{x_{peak} - x_{prevT}}{TT_{av}} \tag{III-16}$$

$$feat104 = \frac{y_{peak} - seg_{min}}{seg_{amp}} \tag{III-17}$$

$$feat105 = \frac{y_{peak}}{glob_{amp}} \tag{III-18}$$

$$feat106 = \frac{seg_{amp}}{glob_{amp}} \tag{III-19}$$

where $comb_{feat1}$ and $comb_{feat2}$ are computed using the equation (III-4) and (III-5); $comb_{feat5}$ and $comb_{feat4}$ are computed using the equation (III-3); x_{segHp} and x_{segLp} are the highest and lowest points away from the $tans_{mean}$ in the short sub-span segment respectively; y_{segHp} and y_{segLp} are the amplitude values corresponding to x_{segHp} and x_{segLp} respectively; x_{prevP}, x_{prevR}, and x_{prevT} are the position indexes of the previous P_{peak}, R_{peak}, and T_{peak} respectively; and PP_{av}, RR_{av}, and TT_{av} are their average peak-to-peak interval respectively; seg_{amp} and $glob_{amp}$ are the amplitude interval of the segment signal and the global signal respectively; 180° and $glob_{amp}$ are normalization values for angle and amplitude/magnitude features respectively. Finally, the 106 features of each of the detected peaks are fed sequentially to the two-cell LSTM model and only

the output of the first cells is considered for the classification. The classification thresholds of the labels are tuned using the receiver operating characteristic (ROC) curve. However, the LSTM model might classify adjacent peaks with the same label. In this case, the only peak with the highest prediction is selected.

III.4. Experiments and Results

The proposed method is evaluated in several experiments for selecting the normalization and reinforcement learning thresholding parameters, and for validating its ability on the delineation.

III.4.1. Datasets description

The delineation method is trained and evaluated on two separate datasets (the QT dataset, and our own manually delineated dataset) with different QRS delineations. The QT-dataset (QTDB) [237] is a collection of 105 two-channel ECG signals obtained from 6 different datasets. The signals are stored with a sampling frequency of 250 Hz and are 15 minutes long each and associated with at least three annotation files generated from two sources namely "ecgpuwave" and the expert annotators. ecgpuwave is a software for the automatic delineation of the fiducial points of the ECG characteristic waves which is used for generating the annotation files for both channels of each signal and covering its entire length. These files are given the extension "pu*" where "*" represents the signal channel number. On the other hand, unlike ecgpuwave-generated annotations, the experts' annotations are manually generated and limited to covering on average up to 30 seconds each for one channel only and positioned at the time position 00h10m00 in each signal. These files are given the extension "q*c" where "*" represents the annotator number. However, only the first annotator's annotation is valid while the second annotator covered 11 signals with limited delineation. Additionally, the two annotation sources of the QTDB are not similar in T waves delineation where some waves are annotated biphasic with ecgpuwave whereas the expert marked them as normal, as well as the T_{onset}s are not delineated in 51 signals in the expert annotation. Furthermore, 29 and 34 out of the 105 signals were rejected from ecgpuwave and the expert annotation respectively due to different issues in the annotation, making 76 and 71 signals selected from ecgpuwave and the expert annotation respectively. Alternatively, our own manually delineated dataset named characteristic waves delineation (CWD) dataset includes 160 annotated signals from 19 individuals. The signals are 10 seconds long each and obtained from three datasets namely MIT Arrhythmia, PTB Diagnostic ECG, and our own ECG recordings with sampling frequencies of 360 Hz, 1000 Hz, and 1000 Hz respectively. The dataset covers examples of

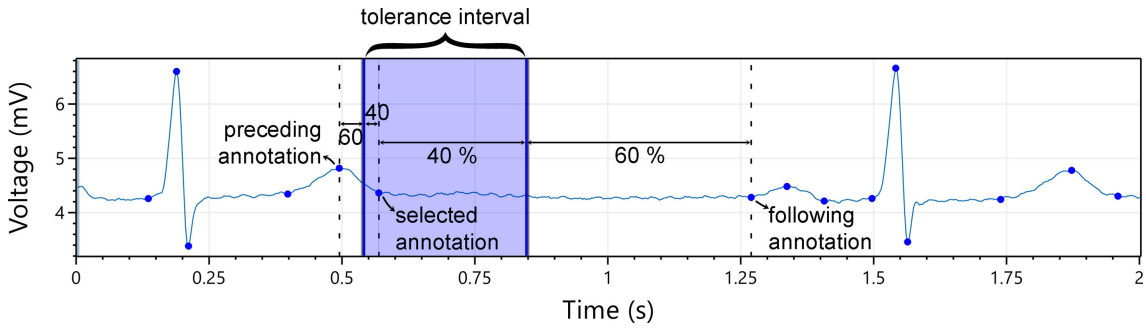

Figure III-9: Example of flexible tolerance of 40% annotation-to-annotation interval.

NSR, ST-depression, complete bundle branch block, tachycardia, Wolf-Parkinson-White pattern, baseline noise, low P waves, positive T waves, and negative T waves. However, the delineation of the QRS complexes is taken as Q_{peak}, R_{peak}, and S_{peak}, unlike the QTDB where they are taken as QRS_{onset}, QRS_{peak}, and QRS_{end}. Also, the peaks are delineated more precise in our dataset other than variating in a tolerance interval as the case in the QTDB. More details on the chosen datasets with regard to their validation results are included in the supplementary data (Appendix B).

III.4.2. Preprocessing

According to several experiments, it is found that the peak analyzer is more suitable with signals normalized to an amplitude interval of 4 giving robustness to tangent computations to signals with both higher and lower waves. Therefore, the signal is firstly normalized to having an amplitude interval of 4 before being fed to the reinforcement learning model and the LSTM model. Additional several experiments were also applied for choosing the reward computing conditions of the reinforcement learning model namely the tolerance of the fiducial points (Tol) and the detected peak over the fiducial points ratio threshold (PFRT). Four different Tol computing approaches and five PFRT are applied making 20 different experiments. The Tol intervals are chosen both as fixed values from the ANSI/AAMI-EC57:1998 standard and the committee for Common Standards for Electrocardiography (CSE) [238], as well as flexible values of annotation-to-annotation interval ratios as illustrated in Figure III-9. Table III-2 lists the results of five experiments using five PFRT values (2, 5, 10, 20, and 30) and a flexible Tol value of 40% annotation-to-annotation interval where MCD is the mean closest distance, sd is the standard deviation, Se is the sensitivity, PPV is the positive predictive value, SP count is the scanned peaks count, and R time is the running time which is the reinforcement learning exploration time. MCD is the mean distance from the annotations to their closest scanned peaks and is computed using the equation (III-3) as follows:

Table III-2: Evaluation results of the performance of the reinforcement learning model in peak analysis using a flexible Tol of 40% and variable PFRT parameters.

Signals count		28										
Samples count		100800										
Annotations count		2825										
Fixed parameter		Tol 40% from annotation-to-annotation										
PFRT	**Metrics**	**P_{onset}**	**P_{peak}**	**P_{end}**	**Q_{peak}**	**R_{peak}**	**S_{peak}**	**T_{onset}**	**T_{peak}**	**T_{end}**	**SP count**	**R. time**
2	**MCD ± sd**	0.05 ± 0.041	0.009 ± 0.031	0.025 ± 0.037	0.018 ± 0.036	**0 ± 0**	0.019 ± 0.056	0.079 ± 0.067	0.013 ± 0.025	0.041 ± 0.035	4099	3 min, 11 sec, 537 millis
	Se (%)	**87.67**	98.61	**89.19**	**98.63**	**100**	98.63	89.86	95.65	**82.61**		
	PPV (%)	**86.11**	92.21	**95.77**	**98.63**	**100**	88.89	76.54	92.42	**88.71**		
5	**MCD ± sd**	0.034 ± 0.032	0.007 ± 0.023	0.019 ± 0.031	0.01 ± 0.024	**0 ± 0**	0.01 ± 0.043	0.043 ± 0.05	0.009 ± 0.017	0.031 ± 0.03	5719	1 min, 6 sec, 439 millis
	Se (%)	82.19	**100**	**89.19**	93.15	**100**	98.63	92.75	**97.1**	62.32		
	PPV (%)	72.15	92.31	85.96	95.77	97.33	98.63	76.74	87.01	82.26		
10	**MCD ± sd**	0.026 ± 0.031	0.004 ± 0.014	0.012 ± 0.026	0.007 ± 0.018	**0 ± 0**	0.005 ± 0.026	0.035 ± 0.048	0.008 ± 0.0143	0.023 ± 0.028	7660	39 sec, 381 millis
	Se (%)	79.45	**100**	78.38	94.52	**100**	**100**	**98.55**	92.75	65.22		
	PPV (%)	79.69	**93.42**	90.14	97.26	**100**	94.74	**78.31**	**95.38**	71.43		
20	**MCD ± sd**	0.019 ± 0.025	**0.002** ± 0.011	0.009 ± 0.019	0.007 ± **0.016**	**0 ± 0**	**0.003** ± **0.02**	**0.022** ± 0.036	**0.006** ± 0.014	**0.016** ± 0.023	12144	24 sec, 561 millis
	Se (%)	64.38	93.06	74.32	91.78	**100**	**100**	91.3	79.71	56.52		
	PPV (%)	78.12	85.71	71.62	97.01	98.65	97.33	72.15	**95.38**	76.92		
30	**MCD ± sd**	**0.017** ± **0.024**	0.003 ± **0.009**	**0.008** ± **0.018**	**0.006** ± **0.016**	**0 ± 0**	0.006 ± 0.03	**0.022** ± **0.034**	**0.006** ± **0.012**	**0.016** ± **0.021**	13089	22 sec, 749 millis
	Se (%)	76.71	94.44	82.43	89.04	**100**	91.78	88.41	92.75	76.81		
	PPV (%)	70	84.34	75.36	95	**100**	**100**	55.56	81.48	71.43		

$$MCD = \frac{1}{N}\sum_{anno=1}^{N} mag(x_{anno}, x_{CSP}) \tag{III-20}$$

where x_{anno} is the position index of the annotation, x_{CSP} is the position index of the closest scanned peak to the selected annotation, and N is the total number of annotations of the same label. The objective with the PFRT and Tol choices was to reduce the scanned peak count while keeping the MCD short and the classification accuracy high. Therefore, the parameters PFRT and Tol are fixed as 2 and 40% respectively. The results of the other 15 experiments are included in the supplementary data (Appendix B).

III.4.3. Delineation results

As an objective to evaluate the performance of the LSTM model as well as the features extraction approach, the proposed method is validated on six experiments using both long signals of 10 and 5 minutes for training and validation respectively as well as selected short fragments for the same assessment. The inter- and intra-patient evaluation paradigms are also taken into consideration and results of the performance of the method in the aforementioned experiments in the delineation of the fiducial points of ECG signals from the QTDB and the

Table III-3: Performance results of the LSTM model in the delineation of the fiducial points of the ECG characteristic waves on the QTDB.

Dataset	Eval paradigm	Metrics	P_{onset}	P_{peak}	P_{end}	QRS_{onset}	QRS_{peak}	QRS_{end}	T_{onset}	T_{peak}	T_{end}
QT ecgpuwave long signals	inter-patient	Se (%)	66.05	93.69	61.38	71.71	**98.6**	69.78	85.79	77.54	47.97
		PPV (%)	**74.37**	81.59	57.94	70.85	97.48	71.07	**77.34**	89.41	74.11
		m±sd (ms)	**0±0.9**	-2.8±11.7	**0.1**±2.4	0±0.3	-0.1±**1.9**	0±1.2	-5.2±18.5	-0.2±8.8	**-0.2±5.2**
	intra-patient	Se (%)	57.09	95.11	58.47	47.68	97.95	73.47	**86.32**	84.72	65.86
		PPV (%)	71.72	88.76	70.67	67.8	**98.38**	72.85	71.87	90.06	**81.3**
		m±sd (ms)	0±1.0	-1.2±7.0	0±2.8	0±0.3	-0.1±3.0	**0**±1.15	6.1±20.1	-1.5±13.3	**-0.2±5.2**
QT ecgpuwave short signals	intra-patient	Se (%)	63.35	89.88	69.9	60.01	96.94	**78.48**	80.91	86.95	60.27
		PPV (%)	73.19	88.8	75.13	72.04	98.13	**75.53**	71.42	82.64	76.32
		m±sd (ms)	0±1.1	-1.0±6.8	-0.8±2.9	**0±0.2**	**0**±2.8	-0.2±1.5	**-2.0±18.2**	-0.7±13.4	-0.2±7.1
QT expert short signals	inter-patient	Se (%)	**79.52**	**95.78**	**80.72**	**84.04**	93.07	68.37	-	**92.17**	**69.28**
		PPV (%)	69.29	**96.07**	**78.59**	**87.46**	85.36	67.56	-	**90.27**	66.47
		m±sd (ms)	0±1.1	**0±3.7**	-0.5**±2.1**	0±2.2	-3.0±11.5	-0.1±**1.1**	-	**-0.1±3.9**	1.1±5.8

Table III-4: Performance results of the LSTM model in the delineation of the fiducial points of the ECG characteristic waves on the CWD dataset.

Dataset	Eval paradigm	Metrics	P_{onset}	P_{peak}	P_{end}	Q_{peak}	R_{peak}	S_{peak}	T_{onset}	T_{peak}	T_{end}
CWD	inter-patient	Se (%)	56.71	**92.73**	63.03	77.18	**100**	79.82	88.96	94.51	50.93
		PPV (%)	48.82	91.62	62.46	75.59	**100**	77.03	69.21	90.91	73.99
		m±sd (ms)	-0.5±2.2	**-0.6±5.6**	-0.6±2.2	**0±0.5**	**0±0**	0.1±1.0	12.5±24.2	-0.9±**10.4**	**0±4.3**
	intra-patient	Se (%)	**74.95**	92.5	**71.01**	**78.78**	99.81	**91.76**	**89.96**	**95.91**	**72.69**
		PPV (%)	**77.59**	**95.25**	**78.95**	**78.33**	99.24	**92.83**	**79.07**	**92.32**	**81.86**
		m±sd (ms)	**0±0.9**	-0.7±7.9	**-0.2±1.4**	0±0.6	0±0.8	**0±0.3**	**-4.3±15.2**	**-0.6**±10.8	0.1±5.3

CWD datasets are listed in Table III-3 and Table III-4 respectively. The tables contain values of the classification evaluation in sensitivity (Se) and positive predictive value (PPV) together with the time error of the positively classified peaks from their true annotations in milliseconds (ms). The values of the sensitivity and PPV are obtained as follows:

$$Se = \frac{TP}{TP + FN} \tag{III-21}$$

$$PPV = \frac{TP}{TP + FP} \tag{III-22}$$

where TP is the true positive, FN is the false negative, and FP is the false positive. Classification is considered as true positive if it falls within the standardized tolerances defined by ANSI/AAMI-EC57:1998 which considers the time error of the classified points from the true annotation within a tolerance of ±75 ms as true positives, in addition to the fiducial point's specific tolerances defined by CSE proposing five different tolerance values of 10.2 ms, 12.7 ms, 6.5 ms, 11.6 ms, and 30.6 ms associated to P_{onset}, P_{end}, QRS_{onset}, QRS_{end}, and T_{end} respectively. The time error of the classification is computed as the deviation of the classified peaks from their nearest true positive annotated fiducial point within the standardized tolerances and is represented as the time error mean (m) ± its standard deviation (sd). Furthermore, the

comparison results of the models listed in Table III-3 and Table III-4 are illustrated in Figure III-10, Figure III-11, Figure III-12, and Figure III-13. The comparison considers the delineation results of the models on three fragments from the QTDB namely sel803, sel808, and selec0406; as well as two fragments from the CWD dataset namely 106m(18), and 123m(12).

III.5. Discussion

This study presents a new method for the delineation of the fiducial points of the ECG signal utilizing a novel peak analyzer algorithm manipulated using a reinforcement learning model for the analysis of the prominent peaks of the ECG signal to be fed sequentially to an LSTM model for classification. The results in Table III-2 clearly shows the ability to compress the samples of the input signal using the peak analyzer while keeping high precisions up to 100% and down to 76.54% along with delineating the prominent peaks over or close to the annotated peaks with a mean closest distance (MCD) down to 0 and up to 0.079 making the radius down to 0 ms and up to 79 ms in time and down to 0 mV and up to 0.079 mV in amplitude. The selected 28 signals contained 100800 samples with 2825 annotated peaks while the reinforcement learning model was able to reduce the scanned peaks count down to 4099 peaks with a flexible tolerance of 40% and a peak over the fiducial points ratio threshold (PFRT) set to 2 for the reward function. The sample reduction using a PFRT=2 reached 95.93% from the total 100800 samples with a peak over fiducial points ratio of 1.45 which validates the reinforcement learning required performance. The evaluation of the delineation of the fiducial points on the QTDB listed in Table III-3 shows a performance of the inter- and the intra-patient paradigm of both long and short signals from the ecgpuwave almost identical on the classification of the P, and T peaks with values ranging from 77.54% to 95.11% and from 81.59% to 90.06% in sensitivity and PPV respectively. The QRS peaks had a better delineation performance with sensitivity and PPV ranging from 96.94% to 98.6% and from 97.48% to 98.38% respectively. The same performance was lower and also identical on the classification of onset and end of each of the P, QRS, and T waves with a sensitivity and PPV ranging from 47.68% to 85.79% and from 57.94% to 81.3% respectively. The expert annotation dataset was only validated with the inter-patient paradigm since it covers short fragments from the signals. The evaluation results in Table III-3 show a better delineation performance compared to the ecgpuwave annotation dataset with sensitivity and PPV of 95.78% and 96.07 for the P_{peak} and of 92.17% and 90.27% for the T_{peak} respectively. The delineation of the QRS_{peak} however was poor with a sensitivity and PPV of 93.07% and 85.36% respectively due to the variated annotation position of the peaks between QRS_{onset} and QRS_{end}. The performance of the delineation of the onset and end of the waves with the expert annotation on the other hand was almost identical to the performance with the ecgpuwave

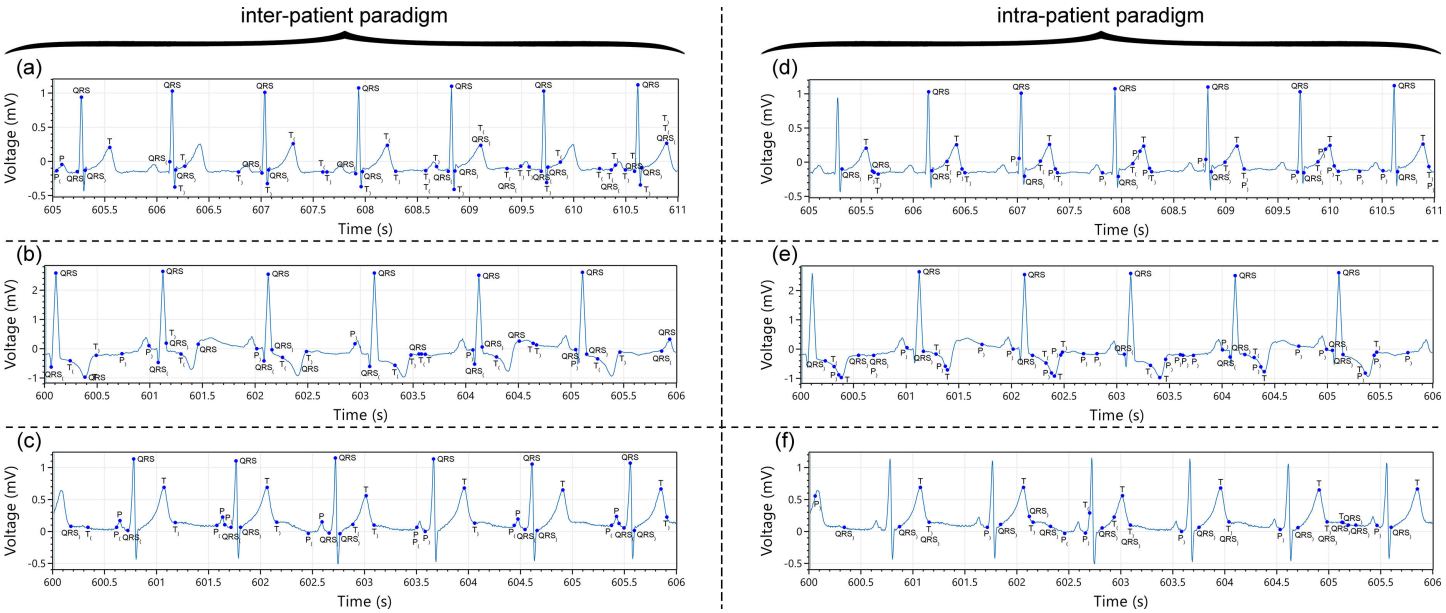

Figure III-10: Comparison in the performance between the inter- and intra-patient paradigm of two LSTM models trained with the first 10 min from the ecgpuwave dataset and tested on fragments from three different signals: (a) and (d) using the signal sel803; (b) and (e) using the signal sel808; and (c) and (f) using the signal sele0406.

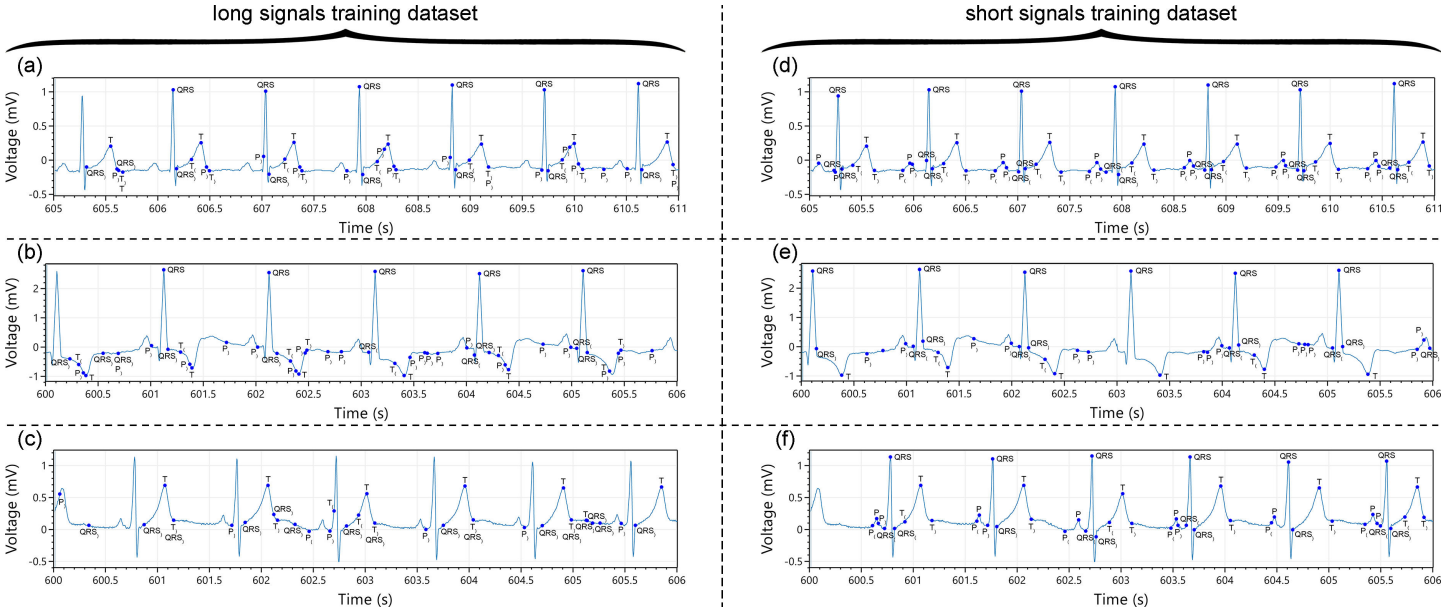

Figure III-11: Comparison in the performance between an LSTM model trained with long signals of 10 min and a second with short signals of 30 sec from the ecgpuwave dataset and tested on fragments from three different signals with the intra-patient paradigm: (a) and (d) using the signal sel803; (b) and (e) using the signal sel808; and (c) and (f) using the signal sele0406.

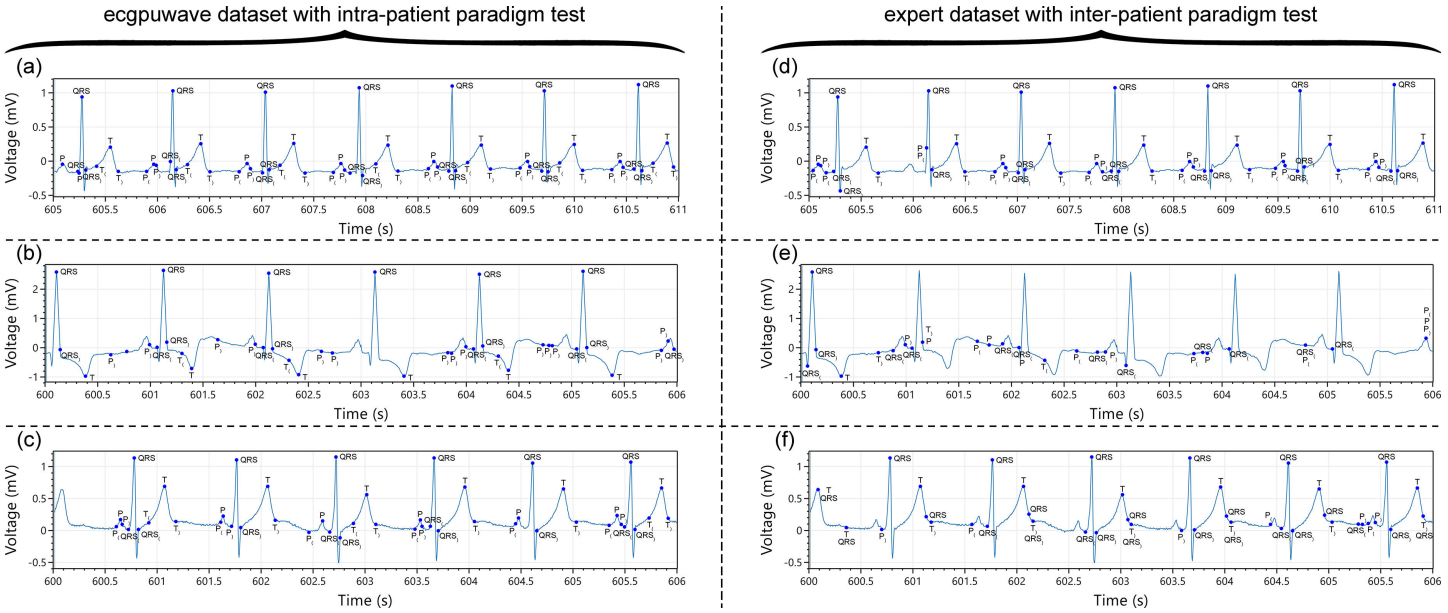

Figure III-12: Comparison in the performance between an LSTM trained with short signals from the ecgpuwave dataset and a second with short signals from the expert dataset and tested on fragments from three different signals with the intra-patient paradigm: (a) and (d) using the signal sel803; (b) and (e) using the signal sel808; and (c) and (f) using the signal sele0406.

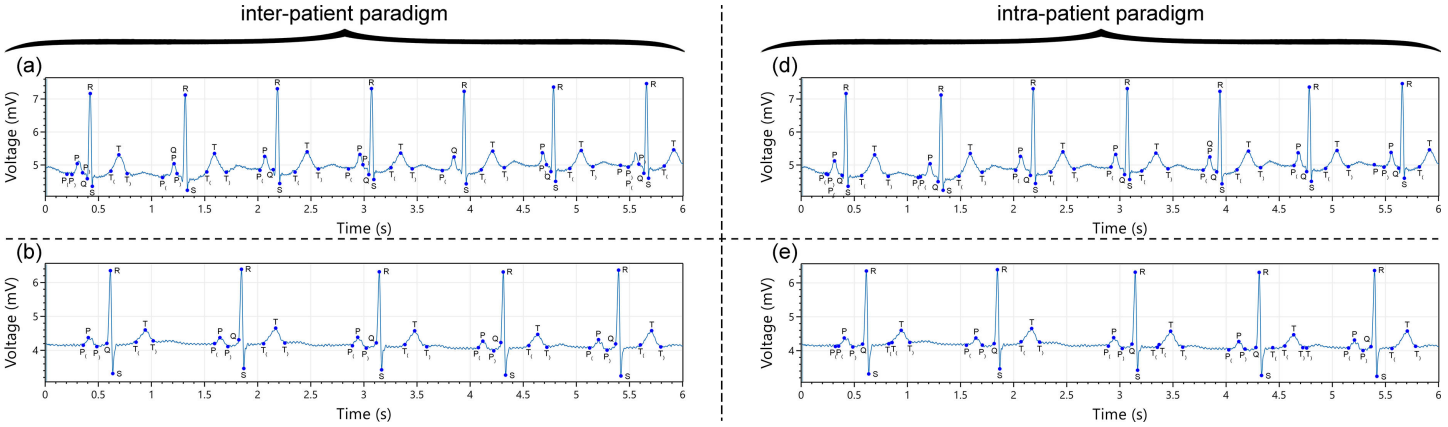

Figure III-13: Comparison in the performance between the inter- and intra-patient paradigm of two LSTM models trained with signals of 10 sec in length from the CWD dataset and tested on fragments from two different signals: (a) and (d) using the signal 106m(18); (b) and (e) using the signal 123m(12).

annotation apart from the delineation of the P_{end} and QRS_{onset} where the results with the expert annotation show better performance with a sensitivity and PPV of 80.72% 78.59% and of 84.04% and 87.46% respectively. The results of the delineation of the T_{onset} were not considered in the performance of the model trained with the expert annotation dataset since 51 of its records do not include the annotation of the T_{onset} which would affect the PPV and the time error results. Furthermore, the results listed in Table III-4 show the CWD dataset-trained model performed almost exactly as the expert dataset-trained model on six fiducial points with a much better

performance on the R_{peak} delineation reaching 100% both in sensitivity and PPV with 0 ms in time error using the CWD dataset. The sensitivity in delineating the P_{onset}, P_{end}, and T_{end} however was lower with values ranging from 60.93% to 63.03%. Besides, the time error results of the proposed method across all the experiments show a high performance in delineating the P_{onset}, P_{end}, QRS_{onset}/Q_{peak}, QRS_{peak}/R_{peak}, and QRS_{end}/S_{peak} with values ranging from 0±0 ms to -0.8±3.0 ms, a medium performance in delineating the P_{peak}, T_{peak}, and T_{end} with values ranging from 0±3.7 ms to -2.8±13.4 ms, and low performance in delineating the T_{onset} with values ranging from -2.0±15.2 ms to 12.5±24.2 ms. The wide range in time error in delineating the QRS_{peak} with the expert dataset refers to the same issue as with its alliance with the poor classification results due to the variated annotation position of the peaks.

The validation results in Table III-3 and Table III-4 show the ability of the proposed method to generalize the performance of the model over the inter- and intra-patient paradigm in addition to whether the model is trained with short or long signals, the model shows an identical performance. However, the results in Figure III-10, Figure III-11, Figure III-12, and Figure III-13 present a different perspective of the performance. The results in Figure III-10 show the long signals trained models have a better performance in QRS_{peak} delineation in the inter-patient paradigm while the T_{peak} delineation is better performed in the intra-patient paradigm. The delineation of the P_{peak} is poor in both experiments except with the record sele0406 where the inter-patient paradigm experiment shows the ability of the model to delineate most of the P_{peak}s even though the classification results in Table III-3 present the opposite where the intra-patient outperforms the inter-patient paradigm. This issue is more clarified in the results in Figure III-11 where the short signals trained model outperforms the long signals trained model in the intra-patient paradigm even though they show the same performance in Table III-3 which may refer to the familiarity of the LSTM memory with the length of the training signals. The poor performance of the models with delineating the P_{peak} of the signal sel808 may also refer to the insufficient data with the negative T waveform where the QTDB contains nine of such records, three of the records with inaccurate T wave delineation, the model was trained with three records and validated with the remaining ones. The results in Figure III-12 show that the ecgpuwave short signals trained model also outperformed the expert short signals trained model opposing to what is mentioned in Table III-3 which may refer either to the varying signal length or the inconsistent manual annotations in the expert dataset. Furthermore, the performance results in Figure III-13 also show the relationship between the length of the training signals and the memory parameters of the LSTM model where the CWD dataset signals are all 10 sec in length which makes the results in Table III-4 aligns with the 6 sec signals in the results of Figure III-13.

The comparison of the proposed method with the related works in Table III-5 show a comparable performance in the classification sensitivity and PPV where Spicher and Kukuk

Table III-5: Comparison of the proposed method with the related works in the delineation of the fiducial points of the ECG characteristic waves.

Method	Metrics	P_{onset}	P_{peak}	P_{end}	QRS_{onset}	QRS_{peak}	QRS_{end}	T_{onset}	T_{peak}	T_{end}
Proposed method	Se (%)	63.35	89.88	69.9	60.01	96.94	78.48	80.91	86.95	60.27
	PPV (%)	73.19	88.8	75.13	72.04	98.13	75.53	71.42	82.64	76.32
	m±sd (ms)	**0±1.1**	**-1.0±6.8**	-0.8**±2.9**	**0±0.2**	**0±2.8**	**-0.2±1.5**	-2.0±18.2	**-0.7±13.4**	-0.2±7.1
Li et al. [199]	Se (%)	98.59	98.68	98.48	98.68	98.68	98.68	98.64	98.64	98.52
	PPV (%)	98.59	**98.68**	98.48	98.68	98.68	98.68	**98.64**	**98.64**	**98.52**
	m±sd (ms)	-	-	-	-	-				
Spicher and Kukuk [232]	Se (%)	**99.91**	**99.91**	**99.91**	**99.92**	**99.92**	**99.92**	**99.93**	**99.89**	**99.89**
	PPV (%)	-	-	-	-	-	-	-	-	-
	m±sd (ms)	0.5±15.1	5.1±10.9	**0.5**±15.0	0.9±8.5	-4.1±4.6	-0.4±9.6	**-0.3**±23.7	-4.5±14.7	0.6±20.3
Krasteva et al. [233]	NPV (%)	-	97.4	-	-	-	-	-	-	-
	PPV (%)	-	95.6	-	-	-	-	-	-	-
	m±sd (ms)	-2.3±7.3	-	-1.4±5.2	-1.1±3.8	-	1.3±7.9	-	-	**-0.1**±9.9
Li et al. [234]	Se (%)	98.99	-	99.75	99.44	-	99.57	99.81	-	97.28
	PPV (%)	98.91	-	**98.72**	**99.82**	-	**99.82**	97.01	-	96.60
	m±sd (ms)	3.7±3.7	-	1.2±4.3	2.5±4.1	-	0.6±3.4	2.0**±4.0**	-	2.0**±3.0**
Peimankar and Puthusserypady [235]	Se (%)	95.49	97.69	96.41	99.75	-	99.36	-	97.71	95.87
	PPV (%)	88.77	90.84	89.06	-	-	-	-	96.51	94.43
	m±sd (ms)	-	-	-	-	-	-	-	-	-
Nurmaini et al. [236]	Se (%)	98.38	-	-	-	99.10	-	98.47	-	-
	PPV (%)	**99.00**	-	-	-	**99.24**	-	97.92	-	-
	m±sd (ms)	-	-	-	-	-	-	-	-	-
ANSI/AAMI-EC57:1998 standards	Tolerance (ms)	±75	±75	±75	±75	±75	±75	±75	±75	±75
CSE standards	Tolerance (ms)	±10.2	-	±12.7	±6.5	-	±11.6	-	-	±30.6

[232] obtained high performance in sensitivity in delineating all fiducial points compared to other proposed methods with values ranging from 99.89% to 99.92%; Li et al. [199] had better values in PPV in the delineation of the Ppeak and the fiducial points of the T wave with values ranging from 98.52% to 98.68%; Krasteva et al. [233], Li et al. [234], Peimankar and Puthusserypady [235], and Nurmaini et al. [236] presented results of delineating part of the fiducial points also with high-performance values ranging from 95.49% to 99.81% and from 88.77% to 99.82% in sensitivity and PPV respectively. However, the high performance of the method proposed by Spicher and Kukuk relies on the pre-segmentation of each of the characteristic waves (P, QRS, and T waves) using their pre-obtained peak locations, the same pre-segmentation technique is also used for separating beats before classification by Nurmaini et al. and Krasteva et al., Li et al.'s method relies mostly on finding the absolute maxima of multiple sliding windows for the detection of the fiducial points which make it susceptible to arrhythmias, Peimankar and Puthusserypady's method is impractical with real-time processing, especially with signals of high sampling frequencies, and Li et al.'s high-performance results are based on time error tolerance of ±150 ms which is considered a biased measurement comparing to the related works. The proposed method on the other hand classifies prominent peaks selected independently from the signal using the peak analyzer and fed sequentially to the

Table III-6: Comparison of the proposed method with the related works in running time.

Method	Processor specs	Beats	Run. time	Normalized
Proposed method	i7-6820HQ @ 2.70 GHz; tick freq: 10 MHz.	7	280.83 ms	40.11 ms
Li et al. [199]	DELL 210-ANJK workstation	6	2.11 sec (QRS); 2.90 sec (P, R, T); 3.97 sec (onsets and ends)	1.49 sec
Spicher and Kukuk [232]	Intel Core i5-4210U processor, 12GB RAM	1	149.9 ms (QRS); 132.4 ms (T); 110.7 ms (P)	393 ms
Krasteva et al. [233]	Intel CPU Xeon Silver 4214R @ 2.4 GHz (2 processors), 96 GB RAM (Intel, Santa Clara, CA, USA), and NVIDIA RTX A5000-24 GB	1	221 µs for segmentation; 176 µs for delineation	397 µs

LSTM without relying on any pre-segmentation of the beats. The selection of the prominent peaks using the peak analyzer also enhanced the proposed method by outperforming the related works in reducing the time error as indicated in bold in Table III-5. Moreover, Table III-6 lists the running time in the delineation of the fiducial points of the proposed method with the related works where Processor specs indicate the machine used for running the method, Beats is the number of beats processed by the proposed method, Run. time is the time spent to process the total beats declared in the "Beats" column, Normalized is the time spent to process a single beat. The running time of the proposed method considers the performance in the result (d) in Figure III-11 where the model yields a good ability to delineate most of the fiducial points. The values in the normalized running time show that Krasteva et al. had the fastest delineation performance with 397 µs in delineating a single beat. However, their method ran on a powerful machine which relies on the high number of the GPU core on the NVIDIA RTX A5000-24 GB. Alternatively, the CPU-based delineation yielded a fast performance using the proposed method with 40.11 ms in delineating a single beat which affirms the ability of the peak analyzer to compress the number of samples while keeping the prominent peaks selected.

Addressing the issues declared in our previous work [230] where the Q and S peaks were naively selected as the preceding and following scanned peaks from the R peak. The current work gave more freedom to the classification of all fiducial points as depicted in Figure III-14 and Figure III-15. The S_{peak} is well delineated in both examples except with the first one in Figure III-15 due to insufficient waveform features. The Q_{peak} however is still inaccurately delineated maybe due to the susceptibility of the selected features to noise. Also, the reinforcement learning model over-reduces the selected peaks skipping low amplitude waves such as the second P wave in Figure III-16 resulting in missing its delineation as captured in Figure III-15. This issue is due to the imbalanced training data of low-amplitude waves to high-amplitude waves.

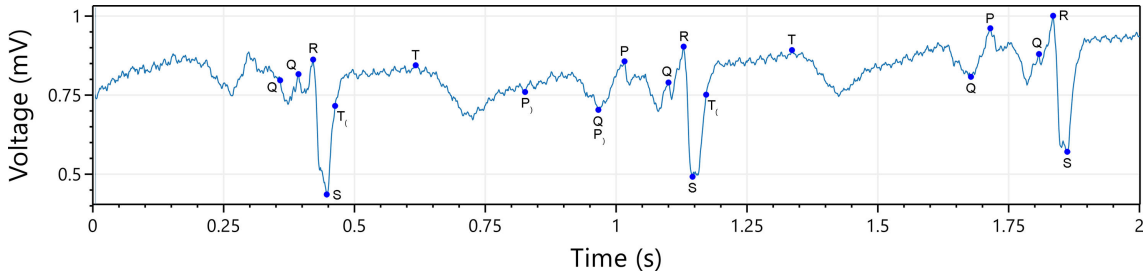

Figure III-14: Delineation of a noisy signal from PTB Diagnostic ECG DB (record s0351lre, lead aVL, at 0 sec).

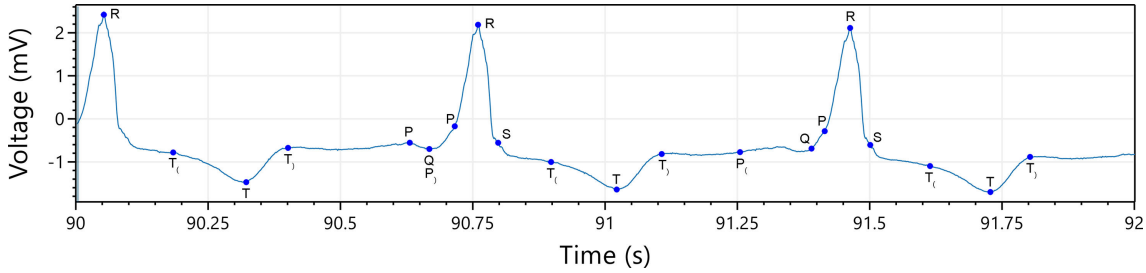

Figure III-15: Delineation of a non-undershoot S_{peak} followed with a negative T wave (record s0351lre, lead V5, at 90 sec).

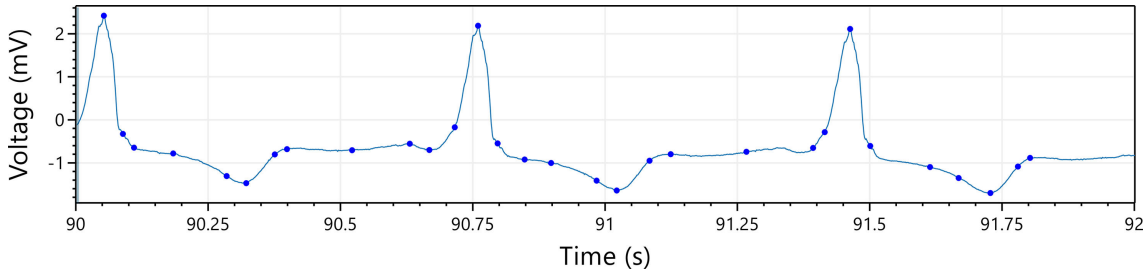

Figure III-16: Reinforcement learning performance on peak analysis using the peak analyzer (record s0351lre, lead V5, at 90 sec) illustrates the ability to reduce the samples of the signal from 2000 to 30 with a reduction ratio of 98.5% of the total samples.

III.6. Conclusion

This chapter proposes a new method for the delineation of the fiducial points of the ECG characteristic waves using two neural network models in two steps. A reinforcement learning model in the first step manipulates a novel algorithm named peak analyzer which is proposed for the selection of the prominent peaks according to the morphology of the input signal. An LSTM model receives then the selected peaks sequentially and associates them with multi-labels from 10 classes (P, QRS, T waves fiducial points, and "other" class) according to their 106 extracted features. Unlike the related works that rely on the pre-segmentation of the input signal [231], [232], [233], [236] and are susceptible to the sampling frequency variation of the input signal [199], [233], [236] as well as arrhythmia [199], the proposed method benefits from the

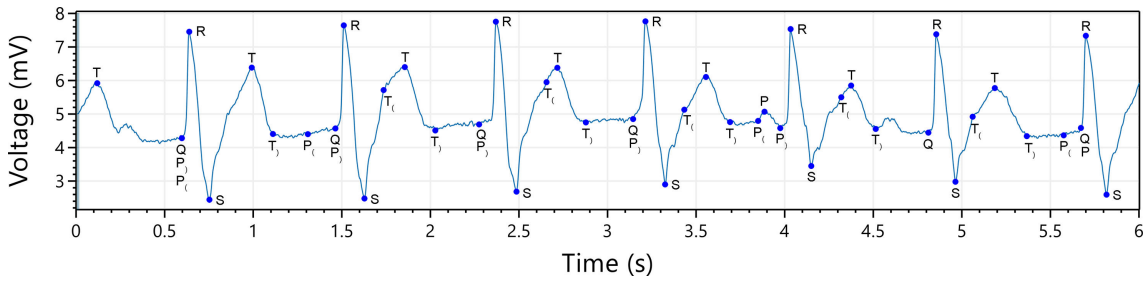

Figure III-17: Performance of the proposed method in delineating the P waves in an ECG signal with a third-degree atrioventricular block.

peak analyzer peak selection which grants it independence from the sampling frequency variation and enhances the classification accuracy by focusing on the quality of the features extraction method on the selected prominent peaks.

The reinforcement learning-based peak analysis achieved high performance in reducing the input samples to 95.93% of reduction from the total samples while keeping a radius down to 0 ms and up to 79 ms in time and down to 0 mV and up to 0.079 mV in amplitude from the annotations. Given the reduction achieved, the method was granted with a low single beat running time performance of 40.11 ms and low time error compared to the related works in addition to yielding an averaged classification performance with the CWD dataset in intra-patient paradigm of 96.07% and 95.60% for the CW peaks, and of 81.23% and 78.33% for CW onsets, and of 78.48% and 84.54% for the CW ends in sensitivity and PPV respectively.

Even though the peak analyzer affords the LSTM flexibility with the selected peaks and hands the classification over to the LSTM memory, the proposed method still shows susceptibility to noise (or maybe to data imbalance) as depicted in Figure III-14, as well as ECG signals with third-degree atrioventricular block. The features of the LSTM were selected to adapt to such diseases where the P wave rhythm is independent of the QRS complex rhythm. However, the results captured in Figure III-17 show that the proposed method is still incapable of handling such scenarios which advocates for proposing better feature extraction techniques to enhance the LSTM classification task.

General Conclusion

This thesis explored the multidimensional landscape of biological signal processing through the lens of artificial intelligence (AI), with a particular focus on the electrocardiogram (ECG). This work was guided by the recognition that biological signals are indispensable tools for observing and interpreting physiological processes. Serving as dynamic interfaces between biological systems and external observers, these signals enable the noninvasive investigation of complex internal phenomena. A central contribution of this work was to address the growing need for structured understanding, precise detection, and automated interpretation of these signals, particularly in scenarios where life-threatening pathologies are involved.

One of the key findings of this research is the vast diversity of biological signals. These signals exist in almost unlimited types, driven by advances in acquisition technologies and the varying forms (electrical, mechanical, thermal, optical, and chemical) in which biological activity manifests. To navigate this complexity, a generalized framework was proposed, classifying biological signals by their origin, dynamic nature, and physical form. This classification serves not only as a conceptual tool for understanding biological signals but also as a practical roadmap for researchers entering this domain.

As an endogenous and dynamic signal of electrical type, the ECG provides critical insights into cardiac activity, capturing the electrophysiological behavior of the atria and ventricles. While disease detection remains its primary application, the ECG is applied in other areas such as cardiac imaging, biometric authentication, and emotion recognition. Each of these domains benefits from AI-driven analysis of ECG data, especially as larger datasets and more complex modeling techniques become accessible.

Building on this foundational understanding, two main contributions were proposed. The first focused on the detection of Wolff-Parkinson-White (WPW) syndrome, a rare but potentially fatal condition characterized by abnormal cardiac conduction and episodes of tachycardia. A novel machine learning-based peak analyzer was developed and evaluated using three different classifiers: k-nearest neighbor, Naïve Bayes, and artificial neural networks. Among these, the neural network-based method achieved the highest overall accuracy of 99.25% in detecting WPW patterns. Importantly, this method stands out as the first to explicitly identify the delta wave. Nonetheless, the method was limited in its ability to reliably delineate Q and S peaks, particularly in noisy environments or signals with atypical morphology.

To overcome these limitations, a second contribution introduced a more robust and efficient delineation framework based on reinforcement learning and Long Short-Term Memory (LSTM) networks. The new system employed a two-parametric peak analyzer for sample reduction

achieving a 95.93% reduction in input samples, passing only the most informative points to the LSTM for detailed delineation of ECG characteristic waves (P, QRS, T). This approach yielded high sensitivity (96.07%) in classifying characteristic waves on our own CWD database. These results represent a significant advancement in precise fiducial point detection and offer promising directions for real-time ECG monitoring systems allowing for runtimes of 40.11 ms per beat. However, challenges remain, particularly in delineating Q peaks under noisy conditions and detecting P waves in cases of third-degree atrioventricular block, where P waves are dissociated from QRS complexes.

Future Work

Despite the encouraging results obtained in this work, several avenues remain open for future investigation. First, while disease detection has been extensively addressed, applications of ECG in cardiac imaging, biometric authentication, and emotion recognition remain underexplored and warrant greater attention. These areas could benefit significantly from deeper integration of AI techniques. Second, persistent challenges in delineating the P wave in ECG signals with complete AV block highlight the need for specialized detection frameworks.

Another important future direction involves enhancing the transparency and interpretability of AI-based diagnostic systems. While current models offer high accuracy, their decision-making processes often remain opaque, limiting clinical trust and regulatory adoption. Integrating Explainable AI (XAI) techniques could offer crucial insights into model behavior, helping bridge the gap between computational analysis and clinical relevance. Lastly, continued efforts should focus on optimizing model complexity, execution time, and memory efficiency to facilitate real-time applications on resource-constrained platforms such as wearable devices and mobile systems.

In conclusion, this thesis demonstrated how biological signal processing, when guided by intelligent algorithmic design, can yield meaningful insights and practical diagnostic tools. The contributions presented herein reinforce the value of AI in biological signal analysis and provide a foundation for continued research into smart, autonomous, and clinically relevant health technologies.

Appendix

Appendix A. Supplementary data

Supplementary data to Chapter II can be found online at https://doi.org/10.17632/5kpr7zwt2v.1.

Supplementary data of 131 ECG signals with beats characteristics and classification features.

The supplementary data consists of:

1. SQLite database.

2. C# code explaining the procedure of querying data from the database.

3. PDF file describing the structure of the data, and the recommended steps for accessing the dataset.

Appendix B. Supplementary data

Supplementary data to Chapter III can be found online at http://doi.org/10.17632/9jz5p3jdg2.1.

Supplementary data containing three databases storing ECG records annotated by three different annotators in addition to the performance results of the proposed method.

The data comprise the following 6 files:

1. PDF file describing the content of the supplementary data, presenting a guide for reading the annotated ECG records, and discussing additional performance comparison of the proposed method with the related works.

2. Excel file presenting the performance of the reinforcement learning model in manipulating the peak analyzer using different episode-ending parameters.

3. Second Excel file describing in detail the selected training and validating datasets from the provided three ECG record databases aligned with the performance results of the proposed method.

4. Three SQLite database files consisting of:

4.a. 73 annotated ECG records selected from the ecgpuwave annotated records of the QTDB.

4.b. 71 annotated ECG records selected from the expert annotated records of the QTDB.

4.c. 160 of our own manually annotated records.

References

[1] E. H. Houssein, I. E. Ibrahim, N. Neggaz, M. Hassaballah, and Y. M. Wazery, 'An efficient ECG arrhythmia classification method based on Manta ray foraging optimization', *Expert Syst. Appl.*, vol. 181, p. 115131, Nov. 2021, doi: 10.1016/j.eswa.2021.115131.

[2] H. Cui, S. Ning, S. Wang, W. Zhang, and Y. Peng, 'ECG Signal Classification Using Interpretable KAN: Towards Predictive Diagnosis of Arrhythmias', *Algorithms*, vol. 18, no. 2, p. 90, Feb. 2025, doi: 10.3390/a18020090.

[3] K.-W. Chen, L. Bear, and C.-W. Lin, 'Solving Inverse Electrocardiographic Mapping Using Machine Learning and Deep Learning Frameworks', *Sensors*, vol. 22, no. 6, p. 2331, Mar. 2022, doi: 10.3390/s22062331.

[4] S. Maleki Lonbar, A. Beigi, N. Bagheri, P. Peris-Lopez, and C. Camara, 'Deep learning based bio-metric authentication system using a high temporal/frequency resolution transform', *Front. Digit. Health*, vol. 6, p. 1463713, Dec. 2024, doi: 10.3389/fdgth.2024.1463713.

[5] J. F. Sedehi, N. J. Dabanloo, K. Maghooli, and A. Sheikhani, 'Develop an emotion recognition system using jointly connectivity between electroencephalogram and electrocardiogram signals', *Heliyon*, vol. 11, no. 2, p. e41767, Jan. 2025, doi: 10.1016/j.heliyon.2025.e41767.

[6] N. Gumpfer, D. Grün, J. Hannig, T. Keller, and M. Guckert, 'Detecting myocardial scar using electrocardiogram data and deep neural networks', *Biol. Chem.*, vol. 402, no. 8, pp. 911–923, Jul. 2021, doi: 10.1515/hsz-2020-0169.

[7] K. Wang, K. Zhang, B. Liu, W. Chen, and M. Han, 'Early prediction of sudden cardiac death risk with Nested LSTM based on electrocardiogram sequential features', *BMC Med. Inform. Decis. Mak.*, vol. 24, no. 1, Apr. 2024, doi: 10.1186/s12911-024-02493-4.

[8] P. Janbakhshi and M. B. Shamsollahi, 'ECG-derived respiration estimation from single-lead ECG using gaussian process and phase space reconstruction methods', *Biomed. Signal Process. Control*, vol. 45, pp. 80–90, Aug. 2018, doi: 10.1016/j.bspc.2018.05.025.

[9] G. A. Orphanides, C. Karittevlis, L. Alsadder, and A. A. Ioannides, 'Using spectral continuity to extract breathing rate from heart rate and its applications in sleep physiology', *Front. Physiol.*, vol. 15, p. 1446868, Aug. 2024, doi: 10.3389/fphys.2024.1446868.

[10] D. Farina *et al.*, 'The Extraction of Neural Information from the Surface EMG for the Control of Upper-Limb Prostheses: Emerging Avenues and Challenges', *IEEE Trans. Neural Syst. Rehabil. Eng.*, vol. 22, no. 4, pp. 797–809, Jul. 2014, doi: 10.1109/TNSRE.2014.2305111.

[11] D. Novak, 'Biomechatronic Applications of Brain-Computer Interfaces', in *Handbook of Biomechatronics*, Elsevier, 2019, pp. 129–175. doi: 10.1016/B978-0-12-812539-7.00008-8.

[12] A. Bomford and R. A. Sherwood, 'Acute and chronic liver disease', in *Clinical Biochemistry: Metabolic and Clinical Aspects*, Elsevier, 2014, pp. 250–272. doi: 10.1016/B978-0-7020-5140-1.00014-6.

[13] S. Ghorashi, D. McGuirt, and N. Nezami, ‘Drug safety in vitro, in vivo, harm, toxicity, dosing, good laboratory practices’, in *Translational Interventional Radiology*, Elsevier, 2023, pp. 55–58. doi: 10.1016/B978-0-12-823026-8.00022-5.

[14] D. Vetturi, M. Tiboni, G. Maternini, and M. Bonera, ‘Use of eye tracking device to evaluate the driver’s behaviour and the infrastructures quality in relation to road safety’, *Transp. Res. Procedia*, vol. 45, pp. 587–595, 2020, doi: 10.1016/j.trpro.2020.03.053.

[15] Z. Bouzid *et al.*, ‘Novel ECG features and machine learning to optimize culprit lesion detection in patients with suspected acute coronary syndrome’, *J. Electrocardiol.*, vol. 69, pp. 31–37, Nov. 2021, doi: 10.1016/j.jelectrocard.2021.07.012.

[16] M. Savadkoohi, T. Oladunni, and L. Thompson, ‘A machine learning approach to epileptic seizure prediction using Electroencephalogram (EEG) Signal’, *Biocybern. Biomed. Eng.*, vol. 40, no. 3, pp. 1328–1341, Jul. 2020, doi: 10.1016/j.bbe.2020.07.004.

[17] A. Menon, L. I. Galindez Olascoaga, N. Shakouri, J. Ruffing, V. Balanaga, and J. M. Rabaey, ‘Brain-inspired Multi-level Control of an Assistive Prosthetic Hand through EMG Task Recognition’, in *2022 IEEE Biomedical Circuits and Systems Conference (BioCAS)*, Taipei, Taiwan: IEEE, Oct. 2022, pp. 384–388. doi: 10.1109/BioCAS54905.2022.9948571.

[18] F. Terranova *et al.*, ‘Windy events detection in big bioacoustics datasets using a pre-trained Convolutional Neural Network’, *Sci. Total Environ.*, vol. 949, p. 174868, Nov. 2024, doi: 10.1016/j.scitotenv.2024.174868.

[19] D. Yan *et al.*, ‘Flexible arc-shaped triboelectric nanogenerator for all directions and highly efficient biomechanical energy harvesting and human motion monitoring’, *Nano Energy*, vol. 129, p. 110000, Oct. 2024, doi: 10.1016/j.nanoen.2024.110000.

[20] E. Kaniusas, *Biomedical Signals and Sensors I: Linking Physiological Phenomena and Biosignals*. in Biological and Medical Physics, Biomedical Engineering. Berlin, Heidelberg: Springer Berlin Heidelberg, 2012. doi: 10.1007/978-3-642-24843-6.

[21] S. Kaplan Berkaya, A. K. Uysal, E. Sora Gunal, S. Ergin, S. Gunal, and M. B. Gulmezoglu, ‘A survey on ECG analysis’, *Biomed. Signal Process. Control*, vol. 43, pp. 216–235, May 2018, doi: 10.1016/j.bspc.2018.03.003.

[22] M. Wasimuddin, K. Elleithy, A.-S. Abuzneid, M. Faezipour, and O. Abuzaghleh, ‘Stages-Based ECG Signal Analysis From Traditional Signal Processing to Machine Learning Approaches: A Survey’, *IEEE Access*, vol. 8, pp. 177782–177803, 2020, doi: 10.1109/ACCESS.2020.3026968.

[23] B. K. Pradhan, B. C. Neelappu, J. Sivaraman, D. Kim, and K. Pal, ‘A Review on the Applications of Time-Frequency Methods in ECG Analysis’, *J. Healthc. Eng.*, vol. 2023, no. 1, p. 3145483, Jan. 2023, doi: 10.1155/2023/3145483.

[24] J. Semmlow, ‘The Big Picture’, in *Circuits, Signals and Systems for Bioengineers*, Elsevier, 2018, pp. 3–50. doi: 10.1016/B978-0-12-809395-5.00001-1.

[25] P. Herrero, P. Georgiou, N. Oliver, D. G. Johnston, and C. Toumazou, ‘A Bio-Inspired Glucose Controller Based on Pancreatic β-Cell Physiology’, *J. Diabetes Sci. Technol.*, vol. 6, no. 3, pp. 606–616, May 2012, doi: 10.1177/193229681200600316.

[26] L. Gonzalez-Carabarin, E. A. Castellanos-Alvarado, P. Castro-Garcia, and M. A. Garcia-Ramirez, ‘Machine Learning for personalised stress detection: Inter-individual variability of EEG-ECG markers for acute-stress response’, *Comput. Methods Programs Biomed.*, vol. 209, p. 106314, Sep. 2021, doi: 10.1016/j.cmpb.2021.106314.

[27] J. Mercier, L. Provins, and J. Hannestad, 'Progress and Challenges in the Development of PET Ligands to Aid CNS Drug Discovery', in *Comprehensive Medicinal Chemistry III*, Elsevier, 2017, pp. 20–64. doi: 10.1016/B978-0-12-409547-2.12437-0.
[28] S. Finger, *Minds Behind the Brain*. Oxford University Press, 2005. doi: 10.1093/acprof:oso/9780195181821.001.0001.
[29] Z. Schofield *et al.*, 'Bioelectrical understanding and engineering of cell biology', *J. R. Soc. Interface*, vol. 17, no. 166, p. 20200013, May 2020, doi: 10.1098/rsif.2020.0013.
[30] H. Kim, S. Song, B. H. Cho, and D. P. Jang, 'Deep learning-based stress detection for daily life use using single-channel EEG and GSR in a virtual reality interview paradigm', *PLOS ONE*, vol. 19, no. 7, p. e0305864, Jul. 2024, doi: 10.1371/journal.pone.0305864.
[31] P. Davidovits, 'Electrical Technology', in *Physics in Biology and Medicine*, Elsevier, 2013, pp. 191–203. doi: 10.1016/B978-0-12-386513-7.00014-X.
[32] J. L. Oschman, 'Energy "Circuits" in the Body', in *Energy Medicine*, Elsevier, 2016, pp. 145–168. doi: 10.1016/B978-0-443-06729-7.00010-7.
[33] P. Hayes *et al.*, 'Converse Magnetoelectric Composite Resonator for Sensing Small Magnetic Fields', *Sci. Rep.*, vol. 9, no. 1, p. 16355, Nov. 2019, doi: 10.1038/s41598-019-52657-w.
[34] R. Hari *et al.*, 'IFCN-endorsed practical guidelines for clinical magnetoencephalography (MEG)', *Clin. Neurophysiol.*, vol. 129, no. 8, pp. 1720–1747, Aug. 2018, doi: 10.1016/j.clinph.2018.03.042.
[35] H. Wang, Z. Xie, L. Lu, B. Su, S. Jung, and X. Xu, 'A mobile platform-based app to assist undergraduate learning of human kinematics in biomechanics courses', *J. Biomech.*, vol. 142, p. 111243, Sep. 2022, doi: 10.1016/j.jbiomech.2022.111243.
[36] L. Ferrández-Laliena *et al.*, 'Diagnostics Using the Change-of-Direction and Acceleration Test (CODAT) of the Biomechanical Patterns Associated with Knee Injury in Female Futsal Players: A Cross-Sectional Analytical Study', *Diagnostics*, vol. 13, no. 5, p. 928, Mar. 2023, doi: 10.3390/diagnostics13050928.
[37] X. Xiao *et al.*, 'Single-cell sequencing reveals the impact of endothelial cell PIEZO1 expression on thoracic aortic aneurysm', *J. Mol. Cell. Cardiol.*, vol. 191, pp. 63–75, Jun. 2024, doi: 10.1016/j.yjmcc.2024.04.015.
[38] A. Saleh Asheghabadi, S. B. Moqadam, and J. Xu, 'Biomechanical Signals-Based Pattern Recognition Using a Developed Algorithm in Upper Limb Amputees', *IEEE Sens. Lett.*, vol. 8, no. 10, pp. 1–4, Oct. 2024, doi: 10.1109/LSENS.2024.3422024.
[39] M. Escabí, 'Biosignal Processing', in *Introduction to Biomedical Engineering*, Elsevier, 2012, pp. 667–746. doi: 10.1016/B978-0-12-374979-6.00011-3.
[40] N. J. Cuper *et al.*, 'The use of near-infrared light for safe and effective visualization of subsurface blood vessels to facilitate blood withdrawal in children', *Med. Eng. Phys.*, vol. 35, no. 4, pp. 433–440, Apr. 2013, doi: 10.1016/j.medengphy.2012.06.007.
[41] C. Kauba, B. Prommegger, and A. Uhl, 'Combined Fully Contactless Finger and Hand Vein Capturing Device with a Corresponding Dataset', *Sensors*, vol. 19, no. 22, p. 5014, Nov. 2019, doi: 10.3390/s19225014.
[42] J. Yu, K. Zhao, Z. Zhang, Y. Zhang, X. Zhang, and H. Ren, 'Development of a bioluminescence resonance energy transfer Quenchbody sensor for the detection of organophosphorus pesticides in water bodies', *Water Res.*, vol. 250, p. 121051, Feb. 2024, doi: 10.1016/j.watres.2023.121051.
[43] Z. Yang *et al.*, 'Folic acid-mediated hollow $$\text {Mn}_{3}\text {O}_{4}$$ nanocomposites for in vivo MRI/FLI monitoring the metastasis of gastric cancer',

Biomed. Eng. OnLine, vol. 23, no. 1, p. 53, Jun. 2024, doi: 10.1186/s12938-024-01248-6.

[44] M. Kumar *et al.*, 'Light origami multi-beam interference digital holographic microscope for live cell imaging', *Opt. Laser Technol.*, vol. 176, p. 110961, Sep. 2024, doi: 10.1016/j.optlastec.2024.110961.

[45] H. Fan *et al.*, 'Transformer-based multimodal feature enhancement networks for multimodal depression detection integrating video, audio and remote photoplethysmograph signals', *Inf. Fusion*, vol. 104, p. 102161, Apr. 2024, doi: 10.1016/j.inffus.2023.102161.

[46] T. Wang, M. Gong, X. Yu, G. Lan, and Y. Shi, 'Acoustic-pressure sensor array system for cardiac-sound acquisition', *Biomed. Signal Process. Control*, vol. 69, p. 102836, Aug. 2021, doi: 10.1016/j.bspc.2021.102836.

[47] D. A. Ramli, Z. X. Wan, and H. Ibrahim, 'Bio-acoustic signal identification based on sparse representation classifier', *J. Phys. Conf. Ser.*, vol. 1529, no. 2, p. 022069, Apr. 2020, doi: 10.1088/1742-6596/1529/2/022069.

[48] Ł. Pawelec, K. Kierczak, and A. Lipowicz, 'Assessment of the obesity based on voice perception', *Anthropol. Rev.*, vol. 85, no. 4, pp. 43–60, Jan. 2023, doi: 10.18778/1898-6773.85.4.04.

[49] M. Torres and H. J. Forman, 'SIGNAL TRANSDUCTION', in *Encyclopedia of Respiratory Medicine*, Elsevier, 2006, pp. 10–18. doi: 10.1016/B0-12-370879-6/00351-3.

[50] P. Van Der Geer, 'Signal Transduction', in *Brenner's Encyclopedia of Genetics*, Elsevier, 2013, pp. 436–439. doi: 10.1016/B978-0-12-374984-0.01424-8.

[51] F. Ribet, G. Stemme, and N. Roxhed, 'Real-time intradermal continuous glucose monitoring using a minimally invasive microneedle-based system', *Biomed. Microdevices*, vol. 20, no. 4, p. 101, Dec. 2018, doi: 10.1007/s10544-018-0349-6.

[52] S. J. Crouzet *et al.*, 'G–PLIP: Knowledge graph neural network for structure-free protein–ligand bioactivity prediction', *Comput. Struct. Biotechnol. J.*, vol. 23, pp. 2872–2882, Dec. 2024, doi: 10.1016/j.csbj.2024.06.029.

[53] J. C. Chato, 'A View of the History of Heat Transfer in Bioengineering', in *Advances in Heat Transfer*, vol. 22, Elsevier, 1992, pp. 1–18. doi: 10.1016/S0065-2717(08)70343-5.

[54] A. G. Rodrigues, 'Biosynthesis of Nanoparticles by Aspergillus and Its Medical Applications', in *New and Future Developments in Microbial Biotechnology and Bioengineering*, Elsevier, 2016, pp. 199–207. doi: 10.1016/B978-0-444-63505-1.00016-6.

[55] S. Ioannou, 'Functional Infrared Thermal Imaging: A Contemporary Tool in Soft Tissue Screening', *Sci. Rep.*, vol. 10, no. 1, p. 9303, Jun. 2020, doi: 10.1038/s41598-020-66397-9.

[56] K. Nagumo, K. Oiwa, and A. Nozawa, 'Spatial normalization of facial thermal images using facial landmarks', *Artif. Life Robot.*, vol. 26, no. 4, pp. 481–487, Nov. 2021, doi: 10.1007/s10015-021-00703-0.

[57] F. Crispi and J. M. Martinez, 'Arrhythmias', in *Obstetric Imaging: Fetal Diagnosis and Care*, Elsevier, 2018, pp. 418-425.e1. doi: 10.1016/B978-0-323-44548-1.00095-4.

[58] J. L. Salinet and O. Luppi Silva, 'ECG Signal Acquisition Systems', in *Developments and Applications for ECG Signal Processing*, Elsevier, 2019, pp. 29–51. doi: 10.1016/B978-0-12-814035-2.00008-6.

[59] A. Daviesis, ‘Calculating cardiac axis on a 12-lead ECG’, *Br. J. Card. Nurs.*, vol. 2, no. 11, pp. 513–517, Nov. 2007, doi: 10.12968/bjca.2007.2.11.27544.
[60] M. Kosuge and K. Kimura, ‘Implications of Using the Cabrera Sequence for Diagnosing Acute Coronary Syndrome’, *Circ. J.*, vol. 80, no. 5, pp. 1087–1096, 2016, doi: 10.1253/circj.cj-16-0126.
[61] J. W. Hurst, ‘Naming of the Waves in the ECG, With a Brief Account of Their Genesis’, *Circulation*, vol. 98, no. 18, pp. 1937–1942, Nov. 1998, doi: 10.1161/01.cir.98.18.1937.
[62] M. J. Boonstra, B. N. Hilderink, E. T. Locati, F. W. Asselbergs, P. Loh, and P. M. Van Dam, ‘Novel *CineECG* enables anatomical 3D localization and classification of bundle branch blocks’, *EP Eur.*, vol. 23, no. Supplement_1, pp. i80–i87, Mar. 2021, doi: 10.1093/europace/euaa396.
[63] P. Cunningham and S. J. Delany, ‘k-Nearest Neighbour Classifiers - A Tutorial’, *ACM Comput. Surv.*, vol. 54, no. 6, pp. 1–25, Jul. 2022, doi: 10.1145/3459665.
[64] I. Wickramasinghe and H. Kalutarage, ‘Naive Bayes: applications, variations and vulnerabilities: a review of literature with code snippets for implementation’, *Soft Comput.*, vol. 25, no. 3, pp. 2277–2293, Feb. 2021, doi: 10.1007/s00500-020-05297-6.
[65] PhysioNet editors, ‘Databases’, *https://physionet.org/about/database/*, Oct. 2023.
[66] G. Li and B. He, ‘Localization of the site of origin of cardiac activation by means of a heart-model-based electrocardiographic imaging approach’, *IEEE Trans. Biomed. Eng.*, vol. 48, no. 6, pp. 660–669, Jun. 2001, doi: 10.1109/10.923784.
[67] A. Rajagopal, V. Radzicki, H. Lee, and S. Chandrasekaran, ‘Nonlinear electrocardiographic imaging using polynomial approximation networks’, *APL Bioeng.*, vol. 2, no. 4, p. 046101, Dec. 2018, doi: 10.1063/1.5038046.
[68] M. Manche *et al.*, ‘A reduced complexity ECG imaging model for regularized inversion optimization’, *Comput. Biol. Med.*, vol. 167, p. 107698, Dec. 2023, doi: 10.1016/j.compbiomed.2023.107698.
[69] G. Kutluana and İ. Türker, ‘Classification of cardiac disorders using weighted visibility graph features from ECG signals’, *Biomed. Signal Process. Control*, vol. 87, p. 105420, Jan. 2024, doi: 10.1016/j.bspc.2023.105420.
[70] C. Zizzo, A. Hassani, and D. Turner, ‘Automatic Detection and Imaging of Ischemic Changes During Electrocardiogram Monitoring’, *IEEE Trans. Biomed. Eng.*, vol. 55, no. 3, pp. 1243–1247, Mar. 2008, doi: 10.1109/TBME.2007.909504.
[71] T. Ortmaier, M. Groger, D. H. Boehm, V. Falk, and G. Hirzinger, ‘Motion Estimation in Beating Heart Surgery’, *IEEE Trans. Biomed. Eng.*, vol. 52, no. 10, pp. 1729–1740, Oct. 2005, doi: 10.1109/TBME.2005.855716.
[72] J. Coll-Font and D. Brooks, ‘ECG-Based Reconstruction of Heart Position and Orientation with Bayesian Optimization’, presented at the 2017 Computing in Cardiology Conference, Sep. 2017. doi: 10.22489/CinC.2017.054-387.
[73] P. M. Van Dam *et al.*, ‘Novel CineECG Derived From Standard 12-Lead ECG Enables Right Ventricle Outflow Tract Localization of Electrical Substrate in Patients With Brugada Syndrome’, *Circ. Arrhythm. Electrophysiol.*, vol. 13, no. 9, p. e008524, Sep. 2020, doi: 10.1161/CIRCEP.120.008524.
[74] P. M. Van Dam, ‘A new anatomical view on the vector cardiogram: The mean temporal-spatial isochrones’, *J. Electrocardiol.*, vol. 50, no. 6, pp. 732–738, Nov. 2017, doi: 10.1016/j.jelectrocard.2017.08.010.

[75] X. Wang, W. Cai, and M. Wang, ‘A novel approach for biometric recognition based on ECG feature vectors’, *Biomed. Signal Process. Control*, vol. 86, p. 104922, Sep. 2023, doi: 10.1016/j.bspc.2023.104922.
[76] Y. Yang *et al.*, ‘Data imbalance in cardiac health diagnostics using CECG-GAN’, *Sci. Rep.*, vol. 14, no. 1, Jun. 2024, doi: 10.1038/s41598-024-65619-8.
[77] J. Sun, ‘Automatic cardiac arrhythmias classification using CNN and attention-based RNN network’, *Healthc. Technol. Lett.*, vol. 10, no. 3, pp. 53–61, Jun. 2023, doi: 10.1049/htl2.12045.
[78] Y. Tao, Z. Li, C. Gu, B. Jiang, and Y. Zhang, ‘ECG-based expert-knowledge attention network to tachyarrhythmia recognition’, *Biomed. Signal Process. Control*, vol. 76, p. 103649, Jul. 2022, doi: 10.1016/j.bspc.2022.103649.
[79] H. Kim, T. Q. Phan, W. Hong, and S. Y. Chun, ‘Physiology-based augmented deep neural network frameworks for ECG biometrics with short ECG pulses considering varying heart rates’, *Pattern Recognit. Lett.*, vol. 156, pp. 1–6, Apr. 2022, doi: 10.1016/j.patrec.2022.02.014.
[80] H.-L. Chan, H.-W. Chang, W.-Y. Hsu, P.-J. Huang, and S.-C. Fang, ‘Convolutional Neural Network for Individual Identification Using Phase Space Reconstruction of Electrocardiogram’, *Sensors*, vol. 23, no. 6, p. 3164, Mar. 2023, doi: 10.3390/s23063164.
[81] T. M. C. Pereira, R. C. Conceição, and R. Sebastião, ‘Initial Study Using Electrocardiogram for Authentication and Identification’, *Sensors*, vol. 22, no. 6, p. 2202, Mar. 2022, doi: 10.3390/s22062202.
[82] M. S. Asif *et al.*, ‘Hybrid Deep Learning and Discrete Wavelet Transform-Based ECG Biometric Recognition for Arrhythmic Patients and Healthy Controls’, *Sensors*, vol. 23, no. 10, p. 4635, May 2023, doi: 10.3390/s23104635.
[83] T. Fan *et al.*, ‘A new deep convolutional neural network incorporating attentional mechanisms for ECG emotion recognition’, *Comput. Biol. Med.*, vol. 159, p. 106938, Jun. 2023, doi: 10.1016/j.compbiomed.2023.106938.
[84] T. Lugovaya, ‘The ECG-ID Database’. physionet.org, 2011. doi: 10.13026/C2J01F.
[85] G. B. Moody and R. G. Mark, ‘The impact of the MIT-BIH Arrhythmia Database’, *IEEE Eng. Med. Biol. Mag.*, vol. 20, no. 3, pp. 45–50, Jun. 2001, doi: 10.1109/51.932724.
[86] J. Farhadi Sedehi, N. Jafarnia Dabanloo, K. Maghooli, and A. Sheikhani, ‘Multimodal insights into granger causality connectivity: Integrating physiological signals and gated eye-tracking data for emotion recognition using convolutional neural network’, *Heliyon*, vol. 10, no. 16, p. e36411, Aug. 2024, doi: 10.1016/j.heliyon.2024.e36411.
[87] A. W. Awan *et al.*, ‘An Ensemble Learning Method for Emotion Charting Using Multimodal Physiological Signals’, *Sensors*, vol. 22, no. 23, p. 9480, Dec. 2022, doi: 10.3390/s22239480.
[88] J. Lee and S. K. Yoo, ‘Recognition of Negative Emotion Using Long Short-Term Memory with Bio-Signal Feature Compression’, *Sensors*, vol. 20, no. 2, p. 573, Jan. 2020, doi: 10.3390/s20020573.
[89] G. Pinto, J. M. Carvalho, F. Barros, S. C. Soares, A. J. Pinho, and S. Brás, ‘Multimodal Emotion Evaluation: A Physiological Model for Cost-Effective Emotion Classification’, *Sensors*, vol. 20, no. 12, p. 3510, Jun. 2020, doi: 10.3390/s20123510.
[90] S. Woo, J. Park, J.-Y. Lee, and I. S. Kweon, ‘CBAM: Convolutional Block Attention Module’, Jul. 18, 2018, *arXiv*: arXiv:1807.06521. doi: 10.48550/arXiv.1807.06521.
[91] A. R. Philip Schmidt, ‘WESAD (Wearable Stress and Affect Detection)’. UCI Machine Learning Repository, 2018. doi: 10.24432/C57K5T.

[92] S. Katsigiannis and N. Ramzan, 'DREAMER: A Database for Emotion Recognition Through EEG and ECG Signals From Wireless Low-cost Off-the-Shelf Devices', *IEEE J. Biomed. Health Inform.*, vol. 22, no. 1, pp. 98–107, Jan. 2018, doi: 10.1109/JBHI.2017.2688239.
[93] R. Subramanian, J. Wache, M. K. Abadi, R. L. Vieriu, S. Winkler, and N. Sebe, 'ASCERTAIN: Emotion and Personality Recognition Using Commercial Sensors', *IEEE Trans. Affect. Comput.*, vol. 9, no. 2, pp. 147–160, Apr. 2018, doi: 10.1109/TAFFC.2016.2625250.
[94] Elsevier, 'ScienceDirect', *https://www.sciencedirect.com/*.
[95] National Center for Biotechnology Information, 'PubMed', *https://pubmed.ncbi.nlm.nih.gov/*.
[96] JSTOR and Portico, 'Constellate', *https://constellate.org/*.
[97] Google, 'Google Scholar', *https://scholar.google.com/*.
[98] Digital Science, 'Dimensions', *https://app.dimensions.ai/*.
[99] J. Pan and W. J. Tompkins, 'A Real-Time QRS Detection Algorithm', *IEEE Trans. Biomed. Eng.*, vol. BME-32, no. 3, pp. 230–236, Mar. 1985, doi: 10.1109/TBME.1985.325532.
[100] J. Talmon, J. Kors, and J. Van Bemmel, 'Adaptive Gaussian filtering in routine ECG/VCG analysis', *IEEE Trans. Acoust. Speech Signal Process.*, vol. 34, no. 3, pp. 527–534, Jun. 1986, doi: 10.1109/TASSP.1986.1164864.
[101] P. N. Casale, R. B. Devereux, D. R. Alonso, E. Campo, and P. Kligfield, 'Improved sex-specific criteria of left ventricular hypertrophy for clinical and computer interpretation of electrocardiograms: validation with autopsy findings.', *Circulation*, vol. 75, no. 3, pp. 565–572, Mar. 1987, doi: 10.1161/01.CIR.75.3.565.
[102] D. A. Coast, R. M. Stern, G. G. Cano, and S. A. Briller, 'An approach to cardiac arrhythmia analysis using hidden Markov models', *IEEE Trans. Biomed. Eng.*, vol. 37, no. 9, pp. 826–836, Sep. 1990, doi: 10.1109/10.58593.
[103] Cuiwei Li, Chongxun Zheng, and Changfeng Tai, 'Detection of ECG characteristic points using wavelet transforms', *IEEE Trans. Biomed. Eng.*, vol. 42, no. 1, pp. 21–28, Jan. 1995, doi: 10.1109/10.362922.
[104] V. X. Afonso, W. J. Tompkins, T. Q. Nguyen, and Shen Luo, 'ECG beat detection using filter banks', *IEEE Trans. Biomed. Eng.*, vol. 46, no. 2, pp. 192–202, Feb. 1999, doi: 10.1109/10.740882.
[105] P. De Chazal, C. Heneghan, E. Sheridan, R. Reilly, P. Nolan, and M. O'Malley, 'Automated processing of the single-lead electrocardiogram for the detection of obstructive sleep apnoea', *IEEE Trans. Biomed. Eng.*, vol. 50, no. 6, pp. 686–696, Jun. 2003, doi: 10.1109/TBME.2003.812203.
[106] P. deChazal, M. O'Dwyer, and R. B. Reilly, 'Automatic Classification of Heartbeats Using ECG Morphology and Heartbeat Interval Features', *IEEE Trans. Biomed. Eng.*, vol. 51, no. 7, pp. 1196–1206, Jul. 2004, doi: 10.1109/TBME.2004.827359.
[107] R. K. Niazy, C. F. Beckmann, G. D. Iannetti, J. M. Brady, and S. M. Smith, 'Removal of FMRI environment artifacts from EEG data using optimal basis sets', *NeuroImage*, vol. 28, no. 3, pp. 720–737, Nov. 2005, doi: 10.1016/j.neuroimage.2005.06.067.
[108] A. H. Khandoker, M. Palaniswami, and C. K. Karmakar, 'Support Vector Machines for Automated Recognition of Obstructive Sleep Apnea Syndrome From ECG Recordings', *IEEE Trans. Inf. Technol. Biomed.*, vol. 13, no. 1, pp. 37–48, Jan. 2009, doi: 10.1109/TITB.2008.2004495.

[109] A. Jovic and N. Bogunovic, 'Electrocardiogram analysis using a combination of statistical, geometric, and nonlinear heart rate variability features', *Artif. Intell. Med.*, vol. 51, no. 3, pp. 175–186, Mar. 2011, doi: 10.1016/j.artmed.2010.09.005.
[110] W. R. M. Dassen *et al.*, 'An Artificial Neural Network to Localize Atrioventricular Accessory Pathways in Patients Suffering from the Wolff-Parkinson-White Syndrome', *Pacing Clin. Electrophysiol.*, vol. 13, no. 12, pp. 1792–1796, Dec. 1990, doi: 10.1111/j.1540-8159.1990.tb06892.x.
[111] T. Stamkopoulos, K. Diamantaras, N. Maglaveras, and M. Strintzis, 'ECG analysis using nonlinear PCA neural networks for ischemia detection', *IEEE Trans. Signal Process.*, vol. 46, no. 11, pp. 3058–3067, Nov. 1998, doi: 10.1109/78.726818.
[112] R. Silipo and C. Marchesi, 'Artificial neural networks for automatic ECG analysis', *IEEE Trans. Signal Process.*, vol. 46, no. 5, pp. 1417–1425, May 1998, doi: 10.1109/78.668803.
[113] M. Kukar, I. Kononenko, C. Grošelj, K. Kralj, and J. Fettich, 'Analysing and improving the diagnosis of ischaemic heart disease with machine learning', *Artif. Intell. Med.*, vol. 16, no. 1, pp. 25–50, May 1999, doi: 10.1016/S0933-3657(98)00063-3.
[114] B. Pourbabaee, M. J. Roshtkhari, and K. Khorasani, 'Deep Convolutional Neural Networks and Learning ECG Features for Screening Paroxysmal Atrial Fibrillation Patients', *IEEE Trans. Syst. Man Cybern. Syst.*, vol. 48, no. 12, pp. 2095–2104, Dec. 2018, doi: 10.1109/TSMC.2017.2705582.
[115] A. Y. Hannun *et al.*, 'Cardiologist-level arrhythmia detection and classification in ambulatory electrocardiograms using a deep neural network', *Nat. Med.*, vol. 25, no. 1, pp. 65–69, Jan. 2019, doi: 10.1038/s41591-018-0268-3.
[116] Z. I. Attia *et al.*, 'Screening for cardiac contractile dysfunction using an artificial intelligence–enabled electrocardiogram', *Nat. Med.*, vol. 25, no. 1, pp. 70–74, Jan. 2019, doi: 10.1038/s41591-018-0240-2.
[117] Z. I. Attia *et al.*, 'An artificial intelligence-enabled ECG algorithm for the identification of patients with atrial fibrillation during sinus rhythm: a retrospective analysis of outcome prediction', *The Lancet*, vol. 394, no. 10201, pp. 861–867, Sep. 2019, doi: 10.1016/S0140-6736(19)31721-0.
[118] H. Elayan, M. Aloqaily, and M. Guizani, 'Digital Twin for Intelligent Context-Aware IoT Healthcare Systems', *IEEE Internet Things J.*, vol. 8, no. 23, pp. 16749–16757, Dec. 2021, doi: 10.1109/JIOT.2021.3051158.
[119] G. Petmezas *et al.*, 'Automated Atrial Fibrillation Detection using a Hybrid CNN-LSTM Network on Imbalanced ECG Datasets', *Biomed. Signal Process. Control*, vol. 63, p. 102194, Jan. 2021, doi: 10.1016/j.bspc.2020.102194.
[120] L. Weixue, X. Zhengyao, and F. Yingjie, 'Microcomputer-based cardiac field simulation model', *Med. Biol. Eng. Comput.*, vol. 31, no. 4, pp. 384–387, Jul. 1993, doi: 10.1007/BF02446692.
[121] K. Aras *et al.*, 'Experimental Data and Geometric Analysis Repository—EDGAR', *J. Electrocardiol.*, vol. 48, no. 6, pp. 975–981, Nov. 2015, doi: 10.1016/j.jelectrocard.2015.08.008.
[122] B. P. Simon and C. Eswaran, 'An ECG Classifier Designed Using Modified Decision Based Neural Networks', *Comput. Biomed. Res.*, vol. 30, no. 4, pp. 257–272, Aug. 1997, doi: 10.1006/cbmr.1997.1446.

[123] J. Boutkan, *ABC of the ECG.: A Guide to Electrocardiography*. in Philips technical library. Thomas, 1968. [Online]. Available: https://books.google.dz/books?id=DC1sAAAAMAAJ
[124] S. Yu and K. Chou, 'Integration of independent component analysis and neural networks for ECG beat classification', *Expert Syst. Appl.*, vol. 34, no. 4, pp. 2841–2846, May 2008, doi: 10.1016/j.eswa.2007.05.006.
[125] U. R. Acharya, H. Fujita, S. L. Oh, Y. Hagiwara, J. H. Tan, and M. Adam, 'Application of deep convolutional neural network for automated detection of myocardial infarction using ECG signals', *Inf. Sci.*, vol. 415–416, pp. 190–198, Nov. 2017, doi: 10.1016/j.ins.2017.06.027.
[126] R. Bousseljot, D. Kreiseler, and A. Schnabel, 'Nutzung der EKG-Signaldatenbank CARDIODAT der PTB über das Internet', *Biomed. Tech. Eng.*, pp. 317–318, Jul. 2009, doi: 10.1515/bmte.1995.40.s1.317.
[127] J. Huang, B. Chen, B. Yao, and W. He, 'ECG Arrhythmia Classification Using STFT-Based Spectrogram and Convolutional Neural Network', *IEEE Access*, vol. 7, pp. 92871–92880, 2019, doi: 10.1109/ACCESS.2019.2928017.
[128] E. M. Lima *et al.*, 'Deep neural network-estimated electrocardiographic age as a mortality predictor', *Nat. Commun.*, vol. 12, no. 1, p. 5117, Aug. 2021, doi: 10.1038/s41467-021-25351-7.
[129] A. H. Ribeiro *et al.*, 'CODE dataset'. The CODE (Clinical Outcomes in Digital Electrocardiography) group, p. 179540985435 Bytes, 2021. doi: 10.17044/SCILIFELAB.15169716.V1.
[130] A. H. Ribeiro *et al.*, 'CODE-15%: a large scale annotated dataset of 12-lead ECGs'. Zenodo, Jun. 09, 2021. doi: 10.5281/ZENODO.4916206.
[131] A. L. P. Ribeiro *et al.*, 'Sami-Trop: 12-lead ECG traces with age and mortality annotations'. Zenodo, Jun. 07, 2021. doi: 10.5281/ZENODO.4905618.
[132] Q. Zhang, D. Zhou, and X. Zeng, 'HeartID: A Multiresolution Convolutional Neural Network for ECG-Based Biometric Human Identification in Smart Health Applications', *IEEE Access*, vol. 5, pp. 11805–11816, 2017, doi: 10.1109/ACCESS.2017.2707460.
[133] M. A. García-González, A. Argelagós-Palau, M. Fernández-Chimeno, and J. Ramos-Castro, 'A comparison of heartbeat detectors for the seismocardiogram', in *Computing in Cardiology 2013*, Sep. 2013, pp. 461–464.
[134] N. Iyengar, C. K. Peng, R. Morin, A. L. Goldberger, and L. A. Lipsitz, 'Age-related alterations in the fractal scaling of cardiac interbeat interval dynamics', *Am. J. Physiol.*, vol. 271, no. 4 Pt 2, pp. R1078-1084, Oct. 1996, doi: 10.1152/ajpregu.1996.271.4.R1078.
[135] P. Albrecht, 'The MIT-BIH ST Change Database'. physionet.org, 1992. doi: 10.13026/C2ZW2H.
[136] G. B. Moody and R. G. Mark, 'MIT-BIH Atrial Fibrillation Database'. physionet.org, 1992. doi: 10.13026/C2MW2D.
[137] S. D. Greenwald, 'The MIT-BIH Malignant Ventricular Arrhythmia Database'. physionet.org, 1992. doi: 10.13026/C22P44.
[138] H. M. Lynn, S. B. Pan, and P. Kim, 'A Deep Bidirectional GRU Network Model for Biometric Electrocardiogram Classification Based on Recurrent Neural Networks', *IEEE Access*, vol. 7, pp. 145395–145405, 2019, doi: 10.1109/ACCESS.2019.2939947.
[139] M. Hammad, P. Pławiak, K. Wang, and U. R. Acharya, 'ResNet-Attention model for human authentication using ECG signals', *Expert Syst.*, vol. 38, no. 6, p. e12547, Sep. 2021, doi: 10.1111/exsy.12547.

[140] H. P. Da Silva, A. Lourenço, A. Fred, N. Raposo, and M. Aires-de-Sousa, 'Check Your Biosignals Here: A new dataset for off-the-person ECG biometrics', *Comput. Methods Programs Biomed.*, vol. 113, no. 2, pp. 503–514, Feb. 2014, doi: 10.1016/j.cmpb.2013.11.017.
[141] R. Srivastva, A. Singh, and Y. N. Singh, 'PlexNet: A fast and robust ECG biometric system for human recognition', *Inf. Sci.*, vol. 558, pp. 208–228, May 2021, doi: 10.1016/j.ins.2021.01.001.
[142] L. Santamaria-Granados, M. Munoz-Organero, G. Ramirez-Gonzalez, E. Abdulhay, and N. Arunkumar, 'Using Deep Convolutional Neural Network for Emotion Detection on a Physiological Signals Dataset (AMIGOS)', *IEEE Access*, vol. 7, pp. 57–67, 2019, doi: 10.1109/ACCESS.2018.2883213.
[143] J. A. Miranda-Correa, M. K. Abadi, N. Sebe, and I. Patras, 'AMIGOS: A Dataset for Affect, Personality and Mood Research on Individuals and Groups', *IEEE Trans. Affect. Comput.*, vol. 12, no. 2, pp. 479–493, Apr. 2021, doi: 10.1109/TAFFC.2018.2884461.
[144] S. Nita, S. Bitam, M. Heidet, and A. Mellouk, 'A new data augmentation convolutional neural network for human emotion recognition based on ECG signals', *Biomed. Signal Process. Control*, vol. 75, p. 103580, May 2022, doi: 10.1016/j.bspc.2022.103580.
[145] M. Soleymani, J. Lichtenauer, T. Pun, and M. Pantic, 'A Multimodal Database for Affect Recognition and Implicit Tagging', *IEEE Trans. Affect. Comput.*, vol. 3, no. 1, pp. 42–55, Jan. 2012, doi: 10.1109/T-AFFC.2011.25.
[146] D. B. Pryor *et al.*, 'Value of the History and Physical in Identifying Patients at Increased Risk for Coronary Artery Disease', *Ann. Intern. Med.*, vol. 118, no. 2, pp. 81–90, Jan. 1993, doi: 10.7326/0003-4819-118-2-199301150-00001.
[147] C. Ramanathan, R. N. Ghanem, P. Jia, K. Ryu, and Y. Rudy, 'Noninvasive electrocardiographic imaging for cardiac electrophysiology and arrhythmia', *Nat. Med.*, vol. 10, no. 4, pp. 422–428, Apr. 2004, doi: 10.1038/nm1011.
[148] R. J. Martis, U. R. Acharya, and L. C. Min, 'ECG beat classification using PCA, LDA, ICA and Discrete Wavelet Transform', *Biomed. Signal Process. Control*, vol. 8, no. 5, pp. 437–448, Sep. 2013, doi: 10.1016/j.bspc.2013.01.005.
[149] N. Luo *et al.*, 'Flexible Piezoresistive Sensor Patch Enabling Ultralow Power Cuffless Blood Pressure Measurement', *Adv. Funct. Mater.*, vol. 26, no. 8, pp. 1178–1187, Feb. 2016, doi: 10.1002/adfm.201504560.
[150] F. A. Elhaj, N. Salim, A. R. Harris, T. T. Swee, and T. Ahmed, 'Arrhythmia recognition and classification using combined linear and nonlinear features of ECG signals', *Comput. Methods Programs Biomed.*, vol. 127, pp. 52–63, Apr. 2016, doi: 10.1016/j.cmpb.2015.12.024.
[151] C. C. Y. Poon, Yuan-Ting Zhang, and Shu-Di Bao, 'A novel biometrics method to secure wireless body area sensor networks for telemedicine and m-health', *IEEE Commun. Mag.*, vol. 44, no. 4, pp. 73–81, Apr. 2006, doi: 10.1109/MCOM.2006.1632652.
[152] Y. Wang, F. Agrafioti, D. Hatzinakos, and K. N. Plataniotis, 'Analysis of Human Electrocardiogram for Biometric Recognition', *EURASIP J. Adv. Signal Process.*, vol. 2008, no. 1, p. 148658, Dec. 2007, doi: 10.1155/2008/148658.
[153] A. D. C. Chan, M. M. Hamdy, A. Badre, and V. Badee, 'Wavelet Distance Measure for Person Identification Using Electrocardiograms', *IEEE Trans. Instrum. Meas.*, vol. 57, no. 2, pp. 248–253, 2008, doi: 10.1109/TIM.2007.909996.

[154] J. S. Arteaga-Falconi, H. Al Osman, and A. El Saddik, ‘ECG Authentication for Mobile Devices’, *IEEE Trans. Instrum. Meas.*, vol. 65, no. 3, pp. 591–600, Mar. 2016, doi: 10.1109/TIM.2015.2503863.
[155] F. Farid, M. Elkhodr, F. Sabrina, F. Ahamed, and E. Gide, ‘A Smart Biometric Identity Management Framework for Personalised IoT and Cloud Computing-Based Healthcare Services’, *Sensors*, vol. 21, no. 2, p. 552, Jan. 2021, doi: 10.3390/s21020552.
[156] J. Blasco and P. Peris-Lopez, ‘On the Feasibility of Low-Cost Wearable Sensors for Multi-Modal Biometric Verification’, *Sensors*, vol. 18, no. 9, p. 2782, Aug. 2018, doi: 10.3390/s18092782.
[157] I. Tanasković *et al.*, ‘CardioPRINT: Biometric identification based on the individual characteristics derived from the cardiogram’, *Expert Syst. Appl.*, vol. 265, p. 126018, Mar. 2025, doi: 10.1016/j.eswa.2024.126018.
[158] I. Tanasković *et al.*, ‘Dataset for CardioPRINT-based Biometric Identification’. Zenodo, Dec. 02, 2024. doi: 10.5281/ZENODO.10204955.
[159] W. A. Tiller, R. McCraty, and M. Atkinson, ‘Cardiac coherence: a new, noninvasive measure of autonomic nervous system order’, *Altern. Ther. Health Med.*, vol. 2, no. 1, pp. 52–65, Jan. 1996.
[160] K. H. Kim, S. W. Bang, and S. R. Kim, ‘Emotion recognition system using short-term monitoring of physiological signals’, *Med. Biol. Eng. Comput.*, vol. 42, no. 3, pp. 419–427, May 2004, doi: 10.1007/BF02344719.
[161] J. Kim and E. Andre, ‘Emotion recognition based on physiological changes in music listening’, *IEEE Trans. Pattern Anal. Mach. Intell.*, vol. 30, no. 12, pp. 2067–2083, Dec. 2008, doi: 10.1109/TPAMI.2008.26.
[162] L. Chen, Y. Zhao, P. Ye, J. Zhang, and J. Zou, ‘Detecting driving stress in physiological signals based on multimodal feature analysis and kernel classifiers’, *Expert Syst. Appl.*, vol. 85, pp. 279–291, Nov. 2017, doi: 10.1016/j.eswa.2017.01.040.
[163] J. A. Healey and R. W. Picard, ‘Stress Recognition in Automobile Drivers’. physionet.org, 2008. doi: 10.13026/C2SG6B.
[164] A. Sepúlveda, F. Castillo, C. Palma, and M. Rodriguez-Fernandez, ‘Emotion Recognition from ECG Signals Using Wavelet Scattering and Machine Learning’, *Appl. Sci.*, vol. 11, no. 11, p. 4945, May 2021, doi: 10.3390/app11114945.
[165] O. Ronneberger, P. Fischer, and T. Brox, ‘U-Net: Convolutional Networks for Biomedical Image Segmentation’, May 18, 2015, *arXiv*: arXiv:1505.04597. doi: 10.48550/arXiv.1505.04597.
[166] K. He, X. Zhang, S. Ren, and J. Sun, ‘Deep Residual Learning for Image Recognition’, in *2016 IEEE Conference on Computer Vision and Pattern Recognition (CVPR)*, Las Vegas, NV, USA: IEEE, Jun. 2016, pp. 770–778. doi: 10.1109/CVPR.2016.90.
[167] Y. Yan, L. Lan, P. Gong, and C. Guo, ‘How humidity and CO2 affect the sleep of older adults? —Insights for improving sleep quality through environmental control’, *Build. Environ.*, vol. 271, p. 112628, Mar. 2025, doi: 10.1016/j.buildenv.2025.112628.
[168] Z. Nizami *et al.*, ‘Supraventricular tachycardia in children’, *Prog. Pediatr. Cardiol.*, vol. 76, p. 101771, Mar. 2025, doi: 10.1016/j.ppedcard.2024.101771.
[169] B. Shrestha *et al.*, ‘Cardiovascular causes of pediatric chest pain: Case-based review’, *Prog. Pediatr. Cardiol.*, vol. 77, p. 101805, Jun. 2025, doi: 10.1016/j.ppedcard.2024.101805.

[170] H. Huiling, L. Keyao, and Z. Yuan Helen, 'Symptomatic complete heart block: A rare complication of anterior myocardial infarction in a young, fit male: A case report', *JEM Rep.*, vol. 4, no. 1, p. 100129, Mar. 2025, doi: 10.1016/j.jemrpt.2024.100129.
[171] D. Potyagaylo *et al.*, 'Interactive teaching of medical 3D cardiac anatomy: atrial anatomy enhanced by ECG and 3D visualization', *Front. Med.*, vol. 11, p. 1422017, Jul. 2024, doi: 10.3389/fmed.2024.1422017.
[172] C. Hallman, R. Baumwart, and R. M. Hallman, '64-Slice ECG-gated computed tomographic angiography for assessment of coronary arteries in brachycephalic dogs with pulmonary stenosis', *Vet. Rec.*, vol. 194, no. 6, p. e3857, Mar. 2024, doi: 10.1002/vetr.3857.
[173] H. Castro, J. D. Garcia-Racines, and A. Bernal-Norena, 'Prediction of paroxysmal atrial fibrillation using a convolutional neural network and electrocardiogram signals', *Int. J. Electr. Comput. Eng. IJECE*, vol. 14, no. 3, p. 2676, Jun. 2024, doi: 10.11591/ijece.v14i3.pp2676-2683.
[174] X. Zhang, Q. Liu, D. He, H. Suo, and C. Zhao, 'Electrocardiogram-Based Biometric Identification Using Mixed Feature Extraction and Sparse Representation', *Sensors*, vol. 23, no. 22, p. 9179, Nov. 2023, doi: 10.3390/s23229179.
[175] A. R. Yuniarti, S. Rizal, and K. M. Lim, 'Single heartbeat ECG authentication: a 1D-CNN framework for robust and efficient human identification', *Front. Bioeng. Biotechnol.*, vol. 12, p. 1398888, Jul. 2024, doi: 10.3389/fbioe.2024.1398888.
[176] P. Yi, Y. Si, W. Fan, and Y. Zhang, 'ECG Biometrics Based on Attention Enhanced Domain Adaptive Feature Fusion Network', *IEEE Access*, vol. 12, pp. 1291–1307, 2024, doi: 10.1109/ACCESS.2023.3346997.
[177] H.-S. Choi, 'Simple Siamese Model with Long Short-Term Memory for User Authentication with Field-Programmable Gate Arrays', *Electronics*, vol. 13, no. 13, p. 2584, Jul. 2024, doi: 10.3390/electronics13132584.
[178] L. Turchet, B. O'Sullivan, R. Ortner, and C. Guger, 'Emotion Recognition of Playing Musicians From EEG, ECG, and Acoustic Signals', *IEEE Trans. Hum.-Mach. Syst.*, vol. 54, no. 5, pp. 619–629, Oct. 2024, doi: 10.1109/THMS.2024.3430327.
[179] W. Zhao, L. Tan, S. Niu, and L. Qing, 'Assessing the Impact of Street Visual Environment on the Emotional Well-Being of Young Adults through Physiological Feedback and Deep Learning Technologies', *Buildings*, vol. 14, no. 6, p. 1730, Jun. 2024, doi: 10.3390/buildings14061730.
[180] M. H. Rahmani, M. Symons, O. Sobhani, R. Berkvens, and M. Weyn, 'EmoWear: Wearable Physiological and Motion Dataset for Emotion Recognition and Context Awareness', *Sci. Data*, vol. 11, no. 1, p. 648, Jun. 2024, doi: 10.1038/s41597-024-03429-3.
[181] R. A. Alharbey, S. Alsubhi, K. Daqrouq, and A. Alkhateeb, 'The continuous wavelet transform using for natural ECG signal arrhythmias detection by statistical parameters', *Alex. Eng. J.*, vol. 61, no. 12, pp. 9243–9248, Dec. 2022, doi: 10.1016/j.aej.2022.03.016.
[182] K. Ma, C. A. Zhan, and F. Yang, 'Multi-classification of arrhythmias using ResNet with CBAM on CWGAN-GP augmented ECG Gramian Angular Summation Field', *Biomed. Signal Process. Control*, vol. 77, p. 103684, Aug. 2022, doi: 10.1016/j.bspc.2022.103684.
[183] R. D. Santos, 'Increased resting heart rate and greater progression of subclinical coronary atherosclerosis: Another bad fact about fast hearts? Commentary on the study of Rubin et al.', *Atherosclerosis*, vol. 220, no. 1, pp. 36–37, Jan. 2012, doi: 10.1016/j.atherosclerosis.2011.07.024.

[184] U. Meyerfeldt *et al.*, 'Heart rate variability before the onset of ventricular tachycardia: differences between slow and fast arrhythmias', *Int. J. Cardiol.*, vol. 84, no. 2–3, pp. 141–151, Aug. 2002, doi: 10.1016/S0167-5273(02)00139-0.
[185] B. Mohebbi, 'ST-Segment Elevation Myocardial Infarction', in *Practical Cardiology*, Elsevier, 2022, pp. 395–411. doi: 10.1016/B978-0-323-80915-3.00039-9.
[186] L. Chhabra, A. Goyal, and M. D. Benham, 'Wolff-Parkinson-White Syndrome', in *StatPearls*, Treasure Island (FL): StatPearls Publishing, 2021. Accessed: Feb. 08, 2025. [Online]. Available: http://www.ncbi.nlm.nih.gov/books/NBK554437/
[187] V. Carbone, F. Ferrara, A. Cassese, and G. Carbone, 'Wolff-Parkinson-White pattern on alternate beats: What is the mechanism?', *J. Electrocardiol.*, vol. 66, pp. 12–15, May 2021, doi: 10.1016/j.jelectrocard.2021.02.008.
[188] S. Bendaram *et al.*, 'Management of Wolff-Parkinson-White syndrome in a patient with peripartum cardiomyopathy', *J. Community Hosp. Intern. Med. Perspect.*, vol. 11, no. 6, pp. 839–842, Nov. 2021, doi: 10.1080/20009666.2021.1978155.
[189] L. F. Lemus, I. Pereira, and R. Valdivieso, 'Wolff-Parkinson-White Syndrome in Third Trimester of Pregnancy', *Cureus*, Mar. 2022, doi: 10.7759/cureus.22731.
[190] A. R. Pereira, A. Briosa, R. Miranda, S. S. Almeida, L. Brandão, and H. Pereira, 'Sudden Cardiac Death: The Most Feared but Potentially Preventable Presentation of Wolff-Parkinson-White Syndrome', *Case Rep. Cardiol.*, vol. 2021, pp. 1–6, Nov. 2021, doi: 10.1155/2021/9083144.
[191] A. Kashou, P. Wackel, and G. Kowlgi Narayan, 'Asymptomatic Ventricular Preexcitation (Wolff-Parkinson-White Pattern): When to Be Concerned', AMERICAN COLLEGE of CARDIOLOGY. [Online]. Available: https://www.acc.org/latest-in-cardiology/articles/2022/02/17/13/25/asymptomatic-ventricular-preexcitation
[192] R. Adwan, S. Thatcher, S. Russo, and S. Tisma-Dupanovic, 'Arrhythmias in children: Too fast or too slow', *Prog. Pediatr. Cardiol.*, vol. 65, p. 101520, Jun. 2022, doi: 10.1016/j.ppedcard.2022.101520.
[193] F. Gritzali, G. Frangakis, and G. Papakonstantinou, 'Detection of the P and T waves in an ECG', *Comput. Biomed. Res.*, vol. 22, no. 1, pp. 83–91, Feb. 1989, doi: 10.1016/0010-4809(89)90017-7.
[194] M. S. Manikandan and K. P. Soman, 'A novel method for detecting R-peaks in electrocardiogram (ECG) signal', *Biomed. Signal Process. Control*, vol. 7, no. 2, pp. 118–128, Mar. 2012, doi: 10.1016/j.bspc.2011.03.004.
[195] L. Maršánová, A. Němcová, R. Smíšek, M. Vítek, and L. Smital, 'Advanced P Wave Detection in Ecg Signals During Pathology: Evaluation in Different Arrhythmia Contexts', *Sci. Rep.*, vol. 9, no. 1, p. 19053, Dec. 2019, doi: 10.1038/s41598-019-55323-3.
[196] T. Tuncer, S. Dogan, P. Plawiak, and A. Subasi, 'A novel Discrete Wavelet-Concatenated Mesh Tree and ternary chess pattern based ECG signal recognition method', *Biomed. Signal Process. Control*, vol. 72, p. 103331, Feb. 2022, doi: 10.1016/j.bspc.2021.103331.
[197] T. Tuncer, S. Dogan, P. Pławiak, and U. Rajendra Acharya, 'Automated arrhythmia detection using novel hexadecimal local pattern and multilevel wavelet transform with ECG signals', *Knowl.-Based Syst.*, vol. 186, p. 104923, Dec. 2019, doi: 10.1016/j.knosys.2019.104923.
[198] A. Subasi, S. Dogan, and T. Tuncer, 'A novel automated tower graph based ECG signal classification method with hexadecimal local adaptive binary pattern and deep learning',

J. Ambient Intell. Humaniz. Comput., vol. 14, no. 2, pp. 711–725, Feb. 2023, doi: 10.1007/s12652-021-03324-4.

[199] G. Li *et al.*, 'A new method of detecting the characteristic waves and their onset and end in electrocardiogram signals', *Biomed. Signal Process. Control*, vol. 75, p. 103607, May 2022, doi: 10.1016/j.bspc.2022.103607.

[200] H. A. Mahamat, S. Jacquir, C. Khalil, G. Laurent, and S. Binczak, 'Wolff-Parkinson-White (WPW) syndrome: The detection of delta wave in an electrocardiogram (ECG)', in *2016 38th Annual International Conference of the IEEE Engineering in Medicine and Biology Society (EMBC)*, Orlando, FL, USA: IEEE, Aug. 2016, pp. 3809–3812. doi: 10.1109/EMBC.2016.7591558.

[201] P. Kühn, C. Lang, and F. Wiesbauer, *ECG MastEry Yellow Belt*. Medmastery GmbH, 2014.

[202] R. Kakkar, R. Malhotra, P. A. Noseworthy, and P. J. Podrid, *Podrid's Real-World ECGs:A Master's Approach to the Art and Practice of Clinical ECG Interpretation*. cardiotext, 2015.

[203] H.-C. Seo, G.-W. Yoon, S. Joo, and G.-B. Nam, 'Multiple electrocardiogram generator with single-lead electrocardiogram', *Comput. Methods Programs Biomed.*, vol. 221, p. 106858, Jun. 2022, doi: 10.1016/j.cmpb.2022.106858.

[204] J. D. Fortune, N. E. Coppa, K. T. Haq, H. Patel, and L. G. Tereshchenko, 'Digitizing ECG image: A new method and open-source software code', *Comput. Methods Programs Biomed.*, vol. 221, p. 106890, Jun. 2022, doi: 10.1016/j.cmpb.2022.106890.

[205] K. J. Abdullah, I. A. Akbar, B. Setiawan, F. Samopa, and N. A. Sani, 'Analysis of the effect of comedic film on changes of heart rate using photoplethysmogram and electrocardiogram', *Procedia Comput. Sci.*, vol. 197, pp. 208–214, 2022, doi: 10.1016/j.procs.2021.12.133.

[206] T. W. Bae and K. K. Kwon, 'ECG PQRST complex detector and heart rate variability analysis using temporal characteristics of fiducial points', *Biomed. Signal Process. Control*, vol. 66, p. 102291, Apr. 2021, doi: 10.1016/j.bspc.2020.102291.

[207] R. Morello, F. Ruffa, I. Jablonski, L. Fabbiano, and C. De Capua, 'An IoT based ECG system to diagnose cardiac pathologies for healthcare applications in smart cities', *Measurement*, vol. 190, p. 110685, Feb. 2022, doi: 10.1016/j.measurement.2021.110685.

[208] A. S. Eltrass, 'Novel cascade filter design of improved sparse low-rank matrix estimation and kernel adaptive filtering for ECG denoising and artifacts cancellation', *Biomed. Signal Process. Control*, vol. 77, p. 103750, Aug. 2022, doi: 10.1016/j.bspc.2022.103750.

[209] Y. Sattar and L. Chhabra, 'Electrocardiogram', in *StatPearls*, Treasure Island (FL): StatPearls Publishing, 2025. Accessed: Feb. 08, 2025. [Online]. Available: http://www.ncbi.nlm.nih.gov/books/NBK549803/

[210] B. Brembilla-Perrot *et al.*, 'Missing diagnosis of preexcitation syndrome on ECG', *Int. J. Cardiol.*, vol. 163, no. 3, pp. 288–293, Mar. 2013, doi: 10.1016/j.ijcard.2011.06.051.

[211] A. Bhatia, J. Sra, and M. Akhtar, 'Preexcitation Syndromes', *Curr. Probl. Cardiol.*, vol. 41, no. 3, pp. 99–137, Mar. 2016, doi: 10.1016/j.cpcardiol.2015.11.002.

[212] M. Saviano, F. Toriello, L. Barbieri, and S. Carugo, 'Ventricular ectopy following accessory pathway ablation in WPW syndrome', *J. Electrocardiol.*, vol. 69, pp. 119–123, Nov. 2021, doi: 10.1016/j.jelectrocard.2021.09.016.

[213] S. Nishiwaki, S. Shizuta, M. Tanaka, A. Komasa, H. Kohjitani, and T. Kimura, 'A case of preexcitation syndrome showing atypical atrioventricular nodal reentrant tachycardia and orthodromic atrioventricular reciprocating tachycardia with a bystander concealed

nodoventricular/nodofascicular pathway', *Hear. Case Rep.*, vol. 8, no. 7, pp. 529–534, Jul. 2022, doi: 10.1016/j.hrcr.2022.05.003.
[214] J. Kulig and B. A. Koplan, 'Wolff-Parkinson-White Syndrome and Accessory Pathways', *Circulation*, vol. 122, no. 15, Oct. 2010, doi: 10.1161/CIRCULATIONAHA.109.929372.
[215] K. Stokfiszewski, K. Wieloch, and M. Yatsymirskyy, 'An efficient implementation of one-dimensional discrete wavelet transform algorithms for GPU architectures', *J. Supercomput.*, vol. 78, no. 9, pp. 11539–11563, Jun. 2022, doi: 10.1007/s11227-022-04331-8.
[216] M. Merbouti Abdenacer, *'Source code' Biological Signal Processing using AI*. C#. [Online]. Available: https://github.com/GaijinOtohp/bsp-using-ai.git
[217] J. Heaton, 'Chapter 5: Feedforward Backpropagation Neural Networks', in *Introduction to Neural Networks for Java, Second Edition*, 2008. [Online]. Available: https://web.archive.org/web/20140625074056/http://www.heatonresearch.com/online/introduction-neural-networks-java-edition-2
[218] C. Munteanu *et al.*, 'Current data regarding homeostasis of tissues oxygenation in pathophysiological and therapeutic circumstances', *Balneo PRM Res. J.*, vol. 14, no. Vol.14, 2, p. 565, Jun. 2023, doi: 10.12680/balneo.2022.565.
[219] N. Chamidah, B. Lestari, H. Susilo, M. Y. Alsagaff, I. N. Budiantara, and D. Aydin, 'Spline Estimator in Nonparametric Ordinal Logistic Regression Model for Predicting Heart Attack Risk', *Symmetry*, vol. 16, no. 11, p. 1440, Oct. 2024, doi: 10.3390/sym16111440.
[220] B. Adams, L. Jacocks, and H. Guo, 'Higher BMI is linked to an increased risk of heart attacks in European adults: a Mendelian randomisation study', *BMC Cardiovasc. Disord.*, vol. 20, no. 1, p. 258, Dec. 2020, doi: 10.1186/s12872-020-01542-w.
[221] N. Bernolian, Radiyati Umi Partan, Siti Nurmaini, Cindy Kesty, and Benedictus Wicaksono Widodo, 'Congenital Heart Diseases in Pregnancy', *Biosci. Med. J. Biomed. Transl. Res.*, vol. 5, no. 4, pp. 988–1004, Jul. 2021, doi: 10.32539/bsm.v5i4.376.
[222] N. Kamal, N. Othman, and A. Salih, 'Incidence and Types of Congenital Heart Diseases among Children in Sulaimani Governorate', *Kurd. J. Appl. Res.*, vol. 2, no. 2, pp. 106–111, Jul. 2017, doi: 10.24017/science.2017.2.15.
[223] E. Ekpe, M. Ikpe, and I. Umoh, 'Echocardiographic pattern of acquired heart diseases in Nigeria', *Niger. Med. J.*, vol. 56, no. 4, p. 253, 2015, doi: 10.4103/0300-1652.169699.
[224] R. Masson, H. Bakhshi, and T. M. Haddad, 'Intermittent left bundle branch block and acute heart failure in trastuzumab-induced cardiotoxicity', *BMJ Case Rep.*, vol. 13, no. 7, p. e236009, Jul. 2020, doi: 10.1136/bcr-2020-236009.
[225] H. Dathe, D. Krefting, and N. Spicher, 'Completing the Cabrera Circle: deriving adaptable leads from ECG limb leads by combining constraints with a correction factor', *Physiol. Meas.*, vol. 44, no. 10, p. 105005, Oct. 2023, doi: 10.1088/1361-6579/acf754.
[226] H. Moeinzadeh *et al.*, 'WCTECGdb: A 12-Lead Electrocardiography Dataset Recorded Simultaneously with Raw Exploring Electrodes' Potential Directly Referred to the Right Leg', *Sensors*, vol. 20, no. 11, p. 3275, Jun. 2020, doi: 10.3390/s20113275.
[227] A. A. Butchy, U. Jain, M. T. Leasure, V. A. Covalesky, and G. S. Mintz, 'Importance of Electrode Selection and Number in Reconstructing Standard Twelve Lead Electrocardiograms', *Biomedicines*, vol. 11, no. 6, p. 1526, May 2023, doi: 10.3390/biomedicines11061526.

[228] Z. Wang, T. Schaul, M. Hessel, H. van Hasselt, M. Lanctot, and N. de Freitas, 'Dueling Network Architectures for Deep Reinforcement Learning', 2015, *arXiv*. doi: 10.48550/ARXIV.1511.06581.
[229] A.-H. Tan, Y.-S. Ong, and A. Tapanuj, 'A hybrid agent architecture integrating desire, intention and reinforcement learning', *Expert Syst. Appl.*, vol. 38, no. 7, pp. 8477–8487, Jul. 2011, doi: 10.1016/j.eswa.2011.01.045.
[230] M. A. Merbouti and D. Cherifi, 'Machine learning based electrocardiogram peaks analyzer for Wolff-Parkinson-White syndrome', *Biomed. Signal Process. Control*, vol. 86, p. 105302, Sep. 2023, doi: 10.1016/j.bspc.2023.105302.
[231] N. Spicher and M. Kukuk, 'ECG delineation using a piecewise Gaussian derivative model with parameters estimated from scale-dependent algebraic expressions', in *2019 41st Annual International Conference of the IEEE Engineering in Medicine and Biology Society (EMBC)*, Berlin, Germany: IEEE, Jul. 2019, pp. 5633–5637. doi: 10.1109/EMBC.2019.8856523.
[232] N. Spicher and M. Kukuk, 'Delineation of Electrocardiograms Using Multiscale Parameter Estimation', *IEEE J. Biomed. Health Inform.*, vol. 24, no. 8, pp. 2216–2229, Aug. 2020, doi: 10.1109/JBHI.2019.2963786.
[233] V. Krasteva, T. Stoyanov, R. Schmid, and I. Jekova, 'Delineation of 12-Lead ECG Representative Beats Using Convolutional Encoder–Decoders with Residual and Recurrent Connections', *Sensors*, vol. 24, no. 14, p. 4645, Jul. 2024, doi: 10.3390/s24144645.
[234] X. Li, W. Cai, B. Xu, Y. Jiang, M. Qi, and M. Wang, 'SEResUTer: a deep learning approach for accurate ECG signal delineation and atrial fibrillation detection', *Physiol. Meas.*, vol. 44, no. 12, p. 125005, Dec. 2023, doi: 10.1088/1361-6579/ad02da.
[235] A. Peimankar and S. Puthusserypady, 'DENS-ECG: A deep learning approach for ECG signal delineation', *Expert Syst. Appl.*, vol. 165, p. 113911, Mar. 2021, doi: 10.1016/j.eswa.2020.113911.
[236] S. Nurmaini *et al.*, 'Electrocardiogram signal classification for automated delineation using bidirectional long short-term memory', *Inform. Med. Unlocked*, vol. 22, p. 100507, 2021, doi: 10.1016/j.imu.2020.100507.
[237] P. Laguna, R. G. Mark, A. Goldberg, and G. B. Moody, 'A database for evaluation of algorithms for measurement of QT and other waveform intervals in the ECG', in *Computers in Cardiology 1997*, Lund, Sweden: IEEE, 1997, pp. 673–676. doi: 10.1109/CIC.1997.648140.
[238] 'Recommendations for measurement standards in quantitative electrocardiography', *Eur. Heart J.*, Oct. 1985, doi: 10.1093/oxfordjournals.eurheartj.a061766.

Abstract

The acquisition procedures for reading biological signals determine the type of the signal obtained and with the advance of acquisition techniques, biological signals have an almost unlimited variety of types some of which are rarely addressed. This thesis establishes a foundational framework for categorizing biological signals by origin, dynamics, and physical form, with a focused review of ECG applications. It highlights the dominance of heuristic, machine learning, and neural network approaches in pathology detection and biometric authentication while identifying understudied areas such as ECG-based imaging and emotion recognition. Building on this, a robust seven-step peak analyzer-based machine learning method is proposed for detecting the ECG characteristic peaks (P, Q, R, S, and T peak) with the rarely studied Wolff-Parkinson-White (WPW) pattern via Delta wave localization, comparing the performance of neural networks, k-nearest neighbors (KNN), and Naïve Bayes algorithms on the MITDB Arrhythmia database. The approach achieves high precision (99.25% accuracy with neural networks) and addresses limitations of the method's dependency on the R peak detection leading to the proposal of an improved novel reinforcement learning-driven peak analyzer paired with an LSTM classifier to automate a real-time independent delineation of the fiducial points (onset, peak, and end) of the ECG characteristic waves, reducing input samples by 95.93% while maintaining low time error, short running time (40.11 ms per beat), and strong classification performance (96.07% sensitivity for peaks) on the QTDB and a custom CWD dataset.

Keywords: Biological signals, Electrocardiogram, Wolff-Parkinson-White, Delineation, Machine learning.

ملخص

تحدد إجراءات الحصول على الإشارات البيولوجية نوع الإشارة المُكتَشَفة، ومع تطور تقنيات الاستحواذ، أصبحت الإشارات البيولوجية تتمتع بتنوع غير محدود تقريبًا، بعضها نادر التناول. تؤسس هذه الأطروحة إطارًا أساسيًا لتصنيف الإشارات البيولوجية حسب المصدر والديناميكيات والشكل المادي، مع مراجعة مُركَّزة لتطبيقات تخطيط القلب الكهربائي .(ECG) تُسلط الضوء على هيمنة المناهج الاستدلالية وتعلم الآلة والشبكات العصبية في اكتشاف الأمراض والمصادقة الحيوية، مع تحديد مجالات غير مدروسة مثل التصوير القائم على تخطيط القلب الكهربائي والتعرف على المشاعر. بناءً على ذلك، تُقترح طريقة قوية مكونة من سبع خطوات قائمة على محلل القمم وتعلم الآلة لاكتشاف القمم المميزة لتخطيط القلب (P، Q، R، S، T)، مع دراسة نادرة لنمط وولف-باركنسون-وايت (WPW) عبر تحديد موجة دلتا، مع مقارنة أداء الشبكات العصبية وخوارزمية الجيران الأقرب(KNN) وخوارزمية بايز الساذجة على قاعدة بيانات MITDB لاضطرابات نظم القلب. حقق النهج دقة عالية (99.25% بالشبكات العصبية)، وتناول قيود اعتماد الطريقة على اكتشاف قمة R، مما أدى إلى اقتراح محلل قمم محسّن مدفوع بتعلم التعزيز مقترنًا بمصنف LSTM لأتمتة تحديد النقاط المرجعية (البداية، القمة، والنهاية) لموجات تخطيط القلب في الوقت الحقيقي بشكل مستقل، مع تقليل العينات المدخلة بنسبة 95.93% مع الحفاظ على خطأ زمني منخفض ووقت تشغيل قصير (40.11 مللي ثانية لكل نبضة) وأداء تصنيف قوي (حساسية 96.07% للقمم) على قاعدة بيانات QTDB ومجموعة بيانات مخصصة CWD.

الكلمات المفتاحية: الإشارات البيولوجية، تخطيط كهربية القلب، وولف-باركنسون-وايت، التحديد، التعلم الآلي.

Résumé

Les procédures d'acquisition des signaux biologiques déterminent le type de signal obtenu. Avec l'avancée des techniques d'acquisition, les signaux biologiques présentent une variété quasi illimitée, dont certains types sont rarement étudiés. Cette thèse établit un cadre fondamental pour catégoriser les signaux biologiques par origine, dynamique et forme physique, avec un examen ciblé des applications de l'électrocardiogramme (ECG). Elle met en lumière la dominance des approches heuristiques, d'apprentissage automatique et des réseaux de neurones dans la détection de pathologies et l'authentification biométrique, tout en identifiant des domaines sous-étudiés tels que l'imagerie basée sur l'ECG et la reconnaissance des émotions. Sur cette base, une méthode robuste en sept étapes, basée sur un analyseur de pics et l'apprentissage automatique, est proposée pour détecter les pics caractéristiques de l'ECG (P, Q, R, S, T), notamment le motif de Wolff-Parkinson-White (WPW) via la localisation de l'onde Delta, en comparant les performances des réseaux de neurones, des k-plus proches voisins (KNN) et de l'algorithme Naïve Bayes sur la base de données MITDB d'arythmie. L'approche atteint une haute précision (99,25 % de précision avec les réseaux de neurones) et aborde les limites de la dépendance de la méthode à la détection du pic R, conduisant à la proposition d'un nouvel analyseur de pics amélioré, piloté par apprentissage par renforcement et couplé à un classifieur LSTM pour automatiser la délimitation en temps réel des points fiduciaires (début, pic, fin) des ondes caractéristiques de l'ECG, réduisant les échantillons d'entrée de 95,93 % tout en maintenant une faible erreur temporelle, un temps d'exécution court (40,11 ms par battement) et une performance de classification élevée (96,07 % de sensibilité pour les pics) sur la base QTDB et un jeu de données personnalisé CWD.

Mots-clés : Signaux biologiques, Électrocardiogramme, Wolff-Parkinson-White, Délinéation, Apprentissage automatique.

Abstract

The acquisition procedures for reading biological signals determine the type of the signal obtained and with the advance of acquisition techniques, biological signals have an almost unlimited variety of types some of which are rarely addressed. This thesis establishes a foundational framework for categorizing biological signals by origin, dynamics, and physical form, with a focused review of ECG applications. It highlights the dominance of heuristic, machine learning, and neural network approaches in pathology detection and biometric authentication while identifying understudied areas such as ECG-based imaging and emotion recognition. Building on this, a robust seven-step peak analyzer-based machine learning method is proposed for detecting the ECG characteristic peaks (P, Q, R, S, and T peak) with the rarely studied Wolff-Parkinson-White (WPW) pattern via Delta wave localization, comparing the performance of neural networks, k-nearest neighbors (KNN), and Naïve Bayes algorithms on the MITDB Arrhythmia database. The approach achieves high precision (99.25% accuracy with neural networks) and addresses limitations of the method's dependency on the R peak detection leading to the proposal of an improved novel reinforcement learning-driven peak analyzer paired with an LSTM classifier to automate a real-time independent delineation of the fiducial points (onset, peak, and end) of the ECG characteristic waves, reducing input samples by 95.93% while maintaining low time error, short running time (40.11 ms per beat), and strong classification performance (96.07% sensitivity for peaks) on the QTDB and a custom CWD dataset.

Keywords: Biological signals, Electrocardiogram, Wolff-Parkinson-White, Delineation, Machine learning.

ملخص

تحدد إجراءات الحصول على الإشارات البيولوجية نوع الإشارة المُكتَشَفة، ومع تطور تقنيات الاستحواذ، أصبحت الإشارات البيولوجية تتمتع بتنوع غير محدود تقريبًا، بعضها نادر التناول. تؤسس هذه الأطروحة إطارًا أساسيًا لتصنيف الإشارات البيولوجية حسب المصدر والديناميكيات والشكل المادي، مع مراجعة مُركَّزة لتطبيقات تخطيط القلب الكهربائي .(ECG) تُسلط الضوء على هيمنة المناهج الاستدلالية وتعلم الآلة والشبكات العصبية في اكتشاف الأمراض والمصادقة الحيوية، مع تحديد مجالات غير مدروسة مثل التصوير القائم على تخطيط القلب الكهربائي والتعرف على المشاعر. بناءً على ذلك، تُقترح طريقة قوية مكونة من سبع خطوات قائمة على محلل القمم وتعلم الآلة لاكتشاف القمم المميزة لتخطيط القلب (P، Q، R، S، T)، مع دراسة نادرة لنمط وولف-باركنسون-وايت (WPW) عبر تحديد موجة دلتا، مع مقارنة أداء الشبكات العصبية وخوارزمية الجيران الأقرب(KNN) وخوارزمية بايز الساذجة على قاعدة بيانات MITDB لاضطرابات نظم القلب. حقق النهج دقة عالية (99.25% بالشبكات العصبية)، وتناول قيود اعتماد الطريقة على اكتشاف قمة R، مما أدى إلى اقتراح محلل قمم محسّن مدفوع بتعلم التعزيز مقترنًا بمصنف LSTMلأتمتة تحديد النقاط المرجعية (البداية، القمة، والنهاية) لموجات تخطيط القلب في الوقت الحقيقي بشكل مستقل، مع تقليل العينات المدخلة بنسبة 95.93% مع الحفاظ على خطأ زمني منخفض ووقت تشغيل قصير (40.11 مللي ثانية لكل نبضة) وأداء تصنيف قوي (حساسية 96.07% للقمم) على قاعدة بيانات QTDB ومجموعة بيانات مخصصة CWD.

الكلمات المفتاحية: الإشارات البيولوجية، تخطيط كهربية القلب، وولف-باركنسون-وايت، التحديد، التعلم الآلي.

Résumé

Les procédures d'acquisition des signaux biologiques déterminent le type de signal obtenu. Avec l'avancée des techniques d'acquisition, les signaux biologiques présentent une variété quasi illimitée, dont certains types sont rarement étudiés. Cette thèse établit un cadre fondamental pour catégoriser les signaux biologiques par origine, dynamique et forme physique, avec un examen ciblé des applications de l'électrocardiogramme (ECG). Elle met en lumière la dominance des approches heuristiques, d'apprentissage automatique et des réseaux de neurones dans la détection de pathologies et l'authentification biométrique, tout en identifiant des domaines sous-étudiés tels que l'imagerie basée sur l'ECG et la reconnaissance des émotions. Sur cette base, une méthode robuste en sept étapes, basée sur un analyseur de pics et l'apprentissage automatique, est proposée pour détecter les pics caractéristiques de l'ECG (P, Q, R, S, T), notamment le motif de Wolff-Parkinson-White (WPW) via la localisation de l'onde Delta, en comparant les performances des réseaux de neurones, des k-plus proches voisins (KNN) et de l'algorithme Naïve Bayes sur la base de données MITDB d'arythmie. L'approche atteint une haute précision (99,25 % de précision avec les réseaux de neurones) et aborde les limites de la dépendance de la méthode à la détection du pic R, conduisant à la proposition d'un nouvel analyseur de pics amélioré, piloté par apprentissage par renforcement et couplé à un classifieur LSTM pour automatiser la délimitation en temps réel des points fiduciaires (début, pic, fin) des ondes caractéristiques de l'ECG, réduisant les échantillons d'entrée de 95,93 % tout en maintenant une faible erreur temporelle, un temps d'exécution court (40,11 ms par battement) et une performance de classification élevée (96,07 % de sensibilité pour les pics) sur la base QTDB et un jeu de données personnalisé CWD.

Mots-clés : Signaux biologiques, Électrocardiogramme, Wolff-Parkinson-White, Délinéation, Apprentissage automatique.